Multifunctional Flexible Laser-Scribed Graphene Sensors for Resilient and Sustainable Electronics

Dissertation by

Altynay Kaidarova

In Partial Fulfillment of the Requirements

For the Degree of

Doctor of Philosophy

King Abdullah University of Science and Technology

Thuwal, Kingdom of Saudi Arabia

March, 2022

EXAMINATION COMMITTEE PAGE

The dissertation of Altynay Kaidarova is approved by the examination committee.

Committee Chairperson: Prof. Jurgen Kosel
Committee Members: Prof. Boon Ooi, Prof. Carlos M.Duarte, and Prof. Ravinder Dahiya

ABSTRACT

Multifunctional Flexible Laser-Scribed Graphene Sensors for Resilient and Sustainable Electronics

Altynay Kaidarova

The Fourth Industrial Revolution is driven by cyber-physical systems, in which sensors link the real and virtual worlds. A global explosion of physical sensors seamlessly connected to networks is expected to produce trillions of sensors annually. To accommodate sustainable sensor production, it is crucial to minimize the consumption of raw materials, the complexity of fabrication, and waste discharge while improving sensor performance and wearability. Graphene has emerged as an excellent candidate material for its electrical and mechanical characteristics; however, its economic impact has been hindered by complex and energy-intensive processes. Meanwhile, printed electronics offer a compelling range of merits for scalable, high-yield, low-cost manufacturing of graphene. Among them, the one-step laser scribing process has enabled a simultaneous formation and patterning of porous graphene in a solid-state and opened new perspectives for versatile and widely tunable physical sensing platforms.

This dissertation introduces flexible, lightweight, and robust Laser-Scribed Graphene sensor solutions for detecting various physical parameters, such as strain, flow, deflection, force, pressure, temperature, conductivity, and magnetic field. Multifunctionality was obtained by exploiting the direct laser scribing process combined with the flexible nature of polyimide and the piezoresistivity of porous graphene. The outstanding properties of LSG, such as low cytotoxicity, biocompatibility, corrosion

resistance, and ability to function under extreme pressure and temperature conditions, allowed targeting diverse emerging applications.

As a wearable device in healthcare, the LSG sensor was utilized to monitor motions involving joint bandings, such as finger folding, knee-related movements, microsleep detection, heart rate monitoring, and plantar pressure measurements. The marine ecosystem was used as an illustrative sensor application to cope with harsh environments. To this end, the sensor measured the velocity of underwater currents, pressure, salinity, and temperature while monitoring the movement of marine animals. The sensitivity to the magnetic field remained stable up to 400 °C, making the LSG sensor a viable option for high-temperature applications. In robotics, the LSG sensor was developed for velocity profile monitoring of drones and as a soft tactile sensor. The study provides insights into methods of improving sensor performance, opportunities, and challenges facing a tangible realization of LSG physical sensors.

ACKNOWLEDGEMENTS

Many people have positively influenced my doctoral journey over the recent years that culminate in this dissertation. This work is an attribute to them and their excellence as it is an example of my academic achievement.

I sincerely thank my supervisor, Prof. Jürgen Kosel, for taking me on as a student, faith and support full of encouragement and enthusiasm. He has been an inspiration, a true definition of a leader, and the ultimate role model. His skillful supervision enriched my academic journey higher than my best expectation. I extend my sincere gratitude to Prof. Khaled Salama and Prof. Boon Ooi for all the help and support since joining KAUST. I also wish to give Dr. Carlos Duarte special thanks for invaluable research opportunities and experiences that I shall never forget. Recognition must also be given to Ulrich Buttner and Ahad Syed for exceptional guidance in various KAUST laboratories. Dr. Nouf Alsharif's support with the biocompatibility study of the graphene sensors is greatly acknowledged. Many thanks to the whole Sensing Magnetism and Microsystems (SMM) group.

My deepest heartfelt gratitude goes to my mother and husband; without their constant love and support, I would not be in my position today. I am greatly indebted to my whole family for taking care of and helping me ever since. I would like to show my thankfulness to the entire KAUST community for making this journey possible., being home for five years and becoming my beacon of peace, hope, and reconciliation.

TABLE OF CONTENTS

LIST OF ABBREVIATIONS

CNTs	Carbon Nanotubes
CTD	Conductivity, Temperature, and Depth
CVD	Chemical Vapor Deposition
CPS	Cyber-Physical System
GF	Gauge factor
GNSS	Global Navigation Satellite Systems
IMU	Inertial Measurement Unit
IoT	Internet- of-Things
LIDAR	Light Detection and Ranging
LSG	Laser-Scribed Graphene
MEMs	Microelectromechanical systems
MWCNTs	Multi-walled carbon nanotubes
PC	Polycarbonate
PCB	Printed Circuit Board
PDMS	Polydimethylsiloxane
PEEK	Polyether ether ketone
PEN	Polyethylene naphthalate
PET	Polyethylene terephthalate
PI	Polyimide
PMMA	Polymethyl methacrylate
PU	Polyurethane
PVC	Polyvinyl chloride
RADAR	Radio Detection and Ranging
RMSE	Root Mean Squared Error
ROS	Robot Operating System
SEM	Scanning Electron Microscopy
SWaP	Size, Weight, and Power
SWCNTs	Single-walled carbon nanotubes
TGM	Thermal Gravimetric
UAV	Unmanned Aerial Vehicles.
XPS	X-Ray Photoelectron Spectroscopy
XRD	X-Ray Diffraction

LIST OF ILLUSTRATIONS

LIST OF TABLES

Chapter 1

Introduction

Over the last few centuries, the globe has experienced three prominent industrial revolutions. The discovery of steam power and the mechanization of production contributed to the First Industrial Revolution, while electric power and assembly lines sparked the Second. In the 1970s, memory-programmable controllers and computers enabled partial digitalization and automation, leading to the Third Industrial Revolution [1]. Today, the scientific and enterprise communities are preparing for the Fourth Industrial Revolution, referred to as Industry 4.0. The key element in implementing this concept is the cyber-physical system (CPSs) [2].

The CPSs are an emerging discipline that involves highly efficient computing, communication and control systems interfacing the physical world [2-4]. Humans, animals, and the environment are part of the physical world that transmit data into the virtual world for the purpose of data management, analysis, and decision-making. Notably, the interactions between cyber components and elements in the physical world occur through sensor devices [3, 5]. Typically, these are physical sensors that detect and monitor their surroundings and communicate the acquired information, from local temperature, pressure, salinity, material deformation to vital health parameters. Physical variables are also of high relevance for a multitude of advanced sensing applications such as in distributed diagnostics, robotics, electronic skins, functional clothing, and many other Internet-of-Things (IoT) solutions[6-8].

As a part of the Trillion Sensors Initiative, a number of visionary organizations have prepared a roadmap document demonstrating the explosion of physical sensors seamlessly connected to networks worldwide [9, 10]. The report indicates that 45 trillion sensors will be produced annually by 2033, fueled by new trends in smart applications (Figure 1.1). This roadmap aims to increase global awareness of the emerging quantity of sensors and facilitate engagements between developers of sensor technologies and those interested in their commercialization [10]. This also implies that to accommodate the effective production of such a large number of sensors, several significant challenges and constraints must be addressed.

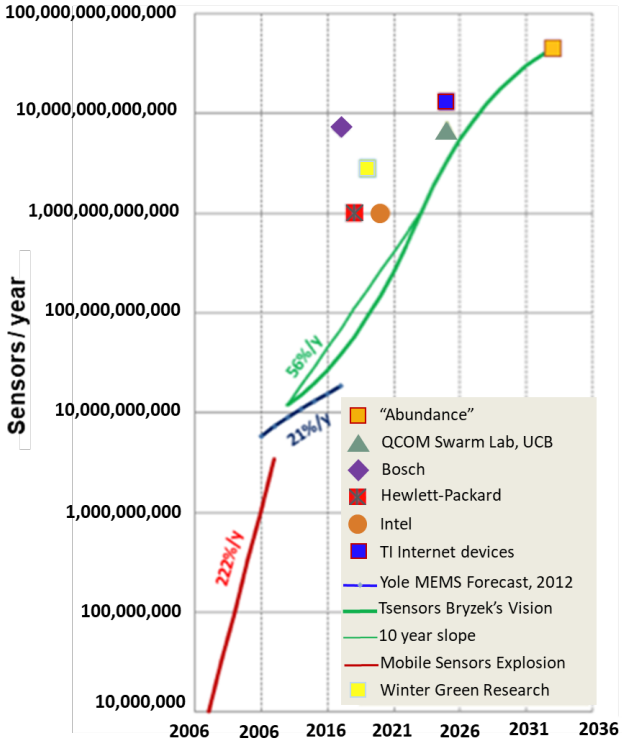

Figure 1.1 - The roadmap to trillions of physical sensors [10].

1.1 Next-Generation Sensor Requirements

The current industrial landscape, characterized by unprecedented levels of volatility, uncertainty, and complexity, together with the ultimate growth in sensor production associated with Industry 4.0 and IoT technologies, is expanding the vision for next-generation sensor technologies [11]. There is a rapidly rising demand for cost-saving sustainable manufacturing, increased wearability, and high-performance devices across a range of healthcare and environmental applications and conditions (Figure 1.2).

In recent years, there has been a heightened awareness of the environment that is reflected in various segments of the industrial market and literature [12]. To cope with this challenge, industrial value creation has been geared towards sustainability. Adoption of sustainable manufacturing is proposed for internal cost savings, opening new markets and meeting the demands of increased sensor production [13]. The sustainability in manufacturing could be achieved by minimized consumption of raw materials, reducing various energy-intensive processing, simplified fabrication processes, and less hazardous waste production [12, 14]. Sustainable manufacturing also enhances corporate image, competitive advantage, and marketing exposure leading to further economic growth and developments [14].

Reliability of information obtained from currently available sensor solutions limits their use in actual medical and clinical practices [15]. Thus, it is essential to enhance accuracy, sensitivity, and long-term stability of sensors to estimate vital metrics associated with physical activity, including heart rate, blood pressure, and energy expenditure. An advanced sensor technology should also survive extreme operating

conditions such as chemically aggressive media, large strain/stress, high temperature, and pressure conditions [16, 17]. This would help to better comprehend conditions that are difficult to analyze, such as the ocean floor, human body and space. As the world moves towards trillions of sensor markets, low-power sensors are needed to extend battery life without affecting performance [18]. Efficient power management is crucial for autonomous vehicles and drones, incorporating numerous sensors with intensive computational requirements. These technologies usually have a fixed energy budget that influences their durability and reliability. Importantly, low-power sensors can be also integrated with various energy harvesting technologies to function continuously for extended periods of time, cutting servicing and battery replacement costs [19].

Another important consideration for the non-invasive and safe usage of skin-mounted electronics is tissue biocompatibility [12]. Although a conclusive meaning encompassed within this term is still debated, it is typically regarded as the material's ability to maintain cellular activity without simulating or arousing any adverse effects to the host. According to internationally recognized biocompatibility standards (ISO 10993 and United States Pharmacopeia (USP) Class VI), wearable devices are expected to undergo cytotoxicity tests [13] to assess the response of living cells to the substance in a cell culture assay, which involves cell viability and the cellular growth.

Wearability refers to the overall user's experience, comfort, and ease of operation while utilizing a particular technological artifact [11]. To improve wearability, it is critical to reduce the weight, size, and a number of rigid components assembled on the device while moving towards all-polymeric flexible and simplified sensor solutions. The

limitations associated with silicon have shifted the focus on alternative materials that can withstand extensive bending cycles, as well as high temperatures, high pressures, and chemically corrosive environments for an extended period of time.

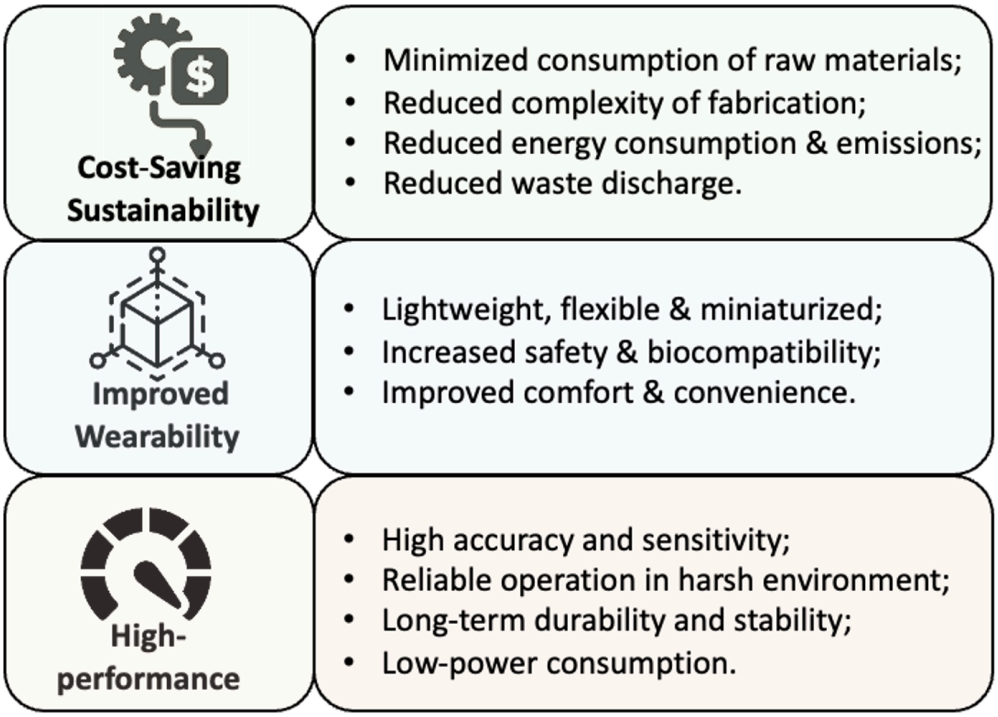

Figure 1.2 - Emerging design requirements of next-generation electronics.

1.2 Rise of Graphene

The unique characteristics of graphene and related two-dimensional materials have attracted considerable research interest across a wide range of applications fields. Graphene is a one-atom thick carbon allotrope arranged in two-dimensional hexagonal lattice. It has emerged as a versatile nanomaterial due to its outstanding characteristics, such as high carrier mobility (~20,000 $cm^2V^{-1}S^{-1}$), thermal conductivity (~5000 W/mK), Young's Modulus (~1 TPa), specific surface area (~ 2630 m^2g^{-1}) and transparency (>90%).

It is fabricated mainly using the *bottom-up* and *top-down* approaches [20] [21]. The former one involves chemistry to assemble carbon atoms into a monolayer structure. The most prominent example of this approach is Chemical Vapor Deposition (CVD), which deposits graphene directly onto nickel or copper films [21, 22]. Transferring graphene onto flexible films, on the other hand, frequently results in a variety of defects and fractures, lowering its overall quality. The *top-down* methods are concerned with disassembling graphite into graphene monolayers using mechanical and liquid phase exfoliations [23]. These approaches are not suited for large-scale graphene manufacturing since they can only produce grams of graphene, which is insufficient for use in industrial applications [24].

In other words, the currently available fabrication processes of graphene entail multi-step chemical synthesis routes, high-temperature and energy-intensive processing, which severely limit its wide-spread commercial potential. It should be noted that according to '*Global Market Insights'* investors are still looking forward to breakthroughs in cost-effective, environmentally friendly mass manufacturing techniques of graphene. Therefore, it is imperative to develop efficient means of fabricating graphene for use in a wide range of electronic devices and applications.

1.3 Dissertation Contributions

The dissertation paves the way towards the developing flexible, multifunctional, and robust graphene sensor platforms through a sustainability-oriented fabrication process. Figure 1.3 summarizes the contributions of this work, which fold in the following streams:

- Utilization of direct laser scribing as a fast and inexpensive technology to prepare, pattern, and customize 3D porous graphene without any functionalization, energy-intensive processing, and subsequent treatments;
- Development of an array of multifunctional graphene transducers that are flexible, lightweight, robust, and biocompatible; and can detect various physical parameters, such as strain, flow, speed, curvature, deflection, force, pressure, conductivity, temperature, and magnetic field;
- Exploitation of LSG electrodes in harsh environments including high temperature, pressure, and salinity, as well as under various bending conditions.
- Establishment of feasible tailoring and enhancement strategies for reliable sensing across a range of subjects and conditions;
- Integration of LSG sensors into various healthcare, robotics, and environmental monitoring applications using custom-made, plug-and-play sensor modules.

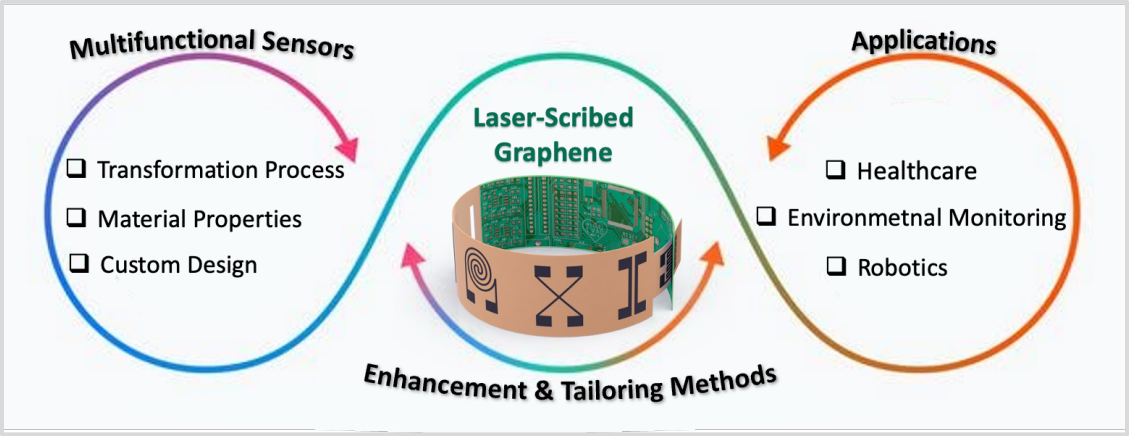

Figure 1.3 - Dissertation contribution for realizing wearable graphene sensor platform.

1.4 Dissertation Outline

Chapter 1 introduces the roadmap to trillions of physical sensors associated with cyber-physical systems and Industry. 4.0, followed by the emerging sensor requirements for a new generation of electronics. The principal research contributions of this dissertation are outlined. The statement of collaborations is also declared.

Chapter 2 provides the necessary background information to comprehend and appreciate the dissertation. Different graphene printing techniques, active sensing components, and flexible substrates are briefly discussed. It provides a comprehensive overview of the LSG formation process, the effect of laser parameters, laser choice, and lasing environments**.**

Chapter 3 presents the findings related to the realization and properties of LSG electrodes. The comprehensive fabrication process, material characterization, and results of cytotoxicity tests are presented. The chapter also reports on the performance of LSG electrodes under extreme environmental conditions.

Chapter 4 introduces a multifunctional and versatile graphene sensor platformThe piezoresistive bending sensor, which can measure a variety of physical quantities with minimal effort and cost, is demonstrated. A bending sensor was utilized to monitor joint-bending-related motions, detecting microsleep, the motion of marine animals, and the velocity of underwater currents.

Chapter 5 presents the effect of repeated laser writing to considerably enhance the electromechanical performance of piezoresistive graphene sensors. A plug-and-play PCB solution was developed for low-cost velocity profile tracking of drones in an outdoor environment.

Chapter 6 introduces laser-scribed pressure sensors for robust pressure measurements in various applications. The sensor was utilized for pulse rate monitoring on the radial artery, plantar pressure measurements, tactile sensing, as well as pressure measurements at a depth of 2 km in highly saline Red Sea water.

Chapter 7 presents the development of flexible conductivity cells for reliable salinity measurements. The two-electrode conductivity cell is proposed to increase the durability of the sensor by solving long-term biofouling issues. The outstanding sensor qualities allow for a less invasive application to the curvatures of underwater animals and sensor integration on CTD systems.

Chapter 8 introduces a flexible graphene Hall-Effect sensor that offers a linear response to magnetic fields, low noise voltage floor, and stability after being exposed to extensive bending cycles. The Hall-Effect sensor was combined with deformable

elastomer and soft magnetic skin to realize a low-cost, compliant, and tactile sensor for healthcare and soft robotics application

Chapter 9 presents the concluding remarks of the dissertation, as well as the overall outlook.

1.5 Statement of Collaboration

This research contributes to the Coupled Animal and Artificial Sensing for Sustainable Ecosystems (CAASE) project led by prof. Carlos M. Duarte. The sensor tests on marine animals, such as dolphins and turtles, were supported by the staff and leadership of the Oceanografic in Valencia and Dr. Nathan R.Geraldi. The biocompatibility evaluation, cell culture, and cell viability tests of the LSG samples were assessed with the help of Dr. Nouf Alsharif. X-ray photoelectron spectroscopy (XPS) analysis of LSG samples were conducted with the aid of Mani Teja Vijjapu under supervision of Prof. Khaled N. Salama.

Chapter 2

Background

Printed electronics (PEs) present a compelling range of merits for scalable, high-yield, low-cost manufacturing of flexible sensors, involving reduced fabrication steps, complexity, and waste discharge. These techniques offer a straightforward and rapid ink deposition over the large-area substrate and a viable route for graphene applications. This section provides an overview of graphene printing techniques commonly utilized for the manufacturing different types of solid-state electronic devices. The methods are compared based on the output resolution, throughput, and limitations. Alternative materials that are commonly utilized in printed electronics are also discussed based on their corresponding sizes, structures, and sheet resistances. The underlying flexible substrates are categorized based on their elastic modulus, Poisson ratio, tensile strain, and temperatures for processing.

2.1 Graphene Printing Techniques

Graphene-based electronics have been reportedly realized using printing technologies, such as ink-jet [25], screen[26], and gravure printing [25, 27]. The PE incorporate various screen masks, nozzles, or patterned cylinders, which determine trade-offs between feature resolution and fabrication throughput as shown in Table 2.1 [28]. These methods are also associated with liquid-phase graphene inks with distinct

physical properties, such as concentration of fillers, viscosity and surface tension of the solution[27].

State-of-the-art techniques for printing graphene rely on liquid-phase ink solutions, consisting of graphene or its derivative fillers in stabilized solutions [27, 29]. The composition of the ink is tailored through the use of solvents, surfactants and/or polymers as indicated in Figure 2.1. The concept behind this method is to reduce the intermolecular forces of interaction between adjacent graphene layers through liquid immersion. In the presence of ultrasonication and high shear rates, the high energy fluctuations cause the adjacent layers of bulk graphite to peel off [29-31]. Exfoliated into individual sheets, graphene utilizes the stabilizing effect of solvents and surfactants to minimize the intermolecular attraction, improving the stability of graphene dispersion. There has been also intensive research devoted to the design and synthesis of graphene hybrid complexes in order to enhance their conductivity [32, 33]. These hybrid inks take advantage of the properties of graphene and conductive polymer or metal particles to tailor for different applications.

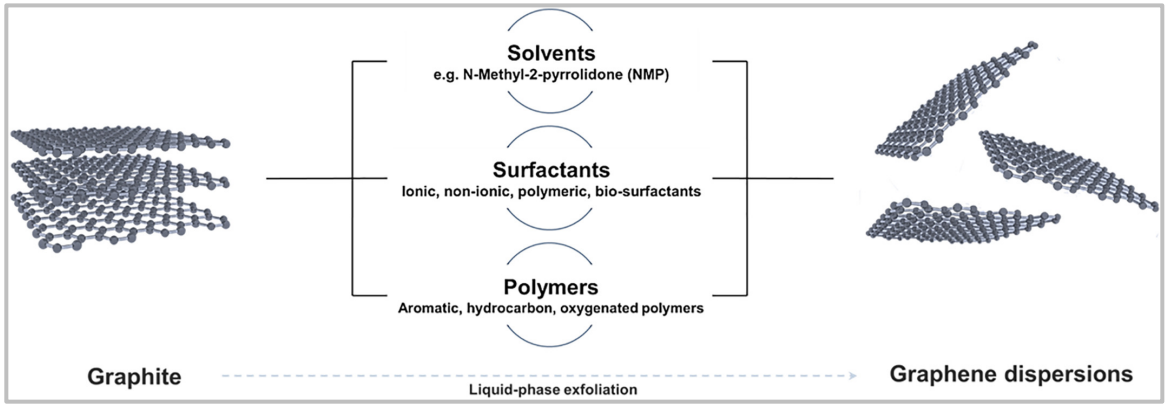

Figure 2.1 - Schematic of the liquid-phase exfoliation process of graphite into graphene dispersions

The screen-printing technique includes transferring a stenciled pattern onto a substrate using an ink, mesh screen, and a squeegee. The ink is squeezed across the stencil, forced through a fine mesh screen, and cured by applying heat or UV lights [34]. Currently, the formulations of graphene inks for screen-printing are mostly focused on either gelation of graphene dispersions [35] or preparation of highly concentrated graphene pastes [36]. Arapov et al. developed colloidally stable and highly concentrated (52 mg/ mL) graphene paste by gelation of graphene in polymer binder [37]. The paste had excellent screen printability with resolution of ~40 µm, high conductivity of ~30 Ω/sq and 25 µm thickness[37]. Meanwhile, Huyn et al. reported paste with a much higher graphene concentration of ~80 mg/mL, and shear viscosity ranging from 1 to 10 Pa at a shear rate of 10 s^{-1}. The paste demonstrated excellent performance during screen printing with resolution of ~40 µm and increased conductivity of ~1.86 × 10^4 S/m. The screen printing with graphene inks suffers from the challenge of controlling the thickness of the printed pattern, as the stencil thickness is the main determinant of the pattern thickness. Due to graphene's tendency to aggregate, it is also difficult to obtain highly viscous and concentrated dispersions of graphene to be used with screen printing[27].

The gravure printing necessitates to use a low-shear viscosity ink suspension. The desired pattern is first carved into the form of a distinct hollow a metallic gravure cylinder, which is then filled with graphene ink. The ink is printed onto desired polymer substrate during contact with the impression cylinder, as shown in Figure 2.2 [38]. To prevent ink leakage from gravure cells and improve line resolution, low shear viscosity inks (in the range of 0.05–0.2 Pa s) are often used. Therefoe, graphene that has been exfoliated using

solvents is well suited to this method. Graphene patterns printed on flexible substrates using gravure printing were demonstrated by Secor et al.[39]. By tuning the ink properties and printing parameters, continuous graphene lines with resolution of ~30 µm were printed over large area[27].

The ink-jet printing requires a high surface tension and diluted ink solution. It enables mask-free and non-contact patterning of graphene ink on flexible substrates by programming the movement of the nozzle. There are two widely used operation regimes of ink-jet printing: drop-on-demand and continuous printing. The former delivers droplets induced by thermal bubbles, and the latter generates a continuous ink stream through a nozzle by the electrostatic or magnetic field [40]. Inkjet printing of graphene has gained tremendous attention in recent years [41-43]. Graphene inks stabilized by ethyl cellulose could be easily utlised with inkjet printers, according to Secor et al[39]. The reported graphene ink had a surface tension of ~33 mN/m and viscosity of 10–12 mPa·s, and was printed using a Fujifilm Dimatix Materials Printer (DMP-2800).

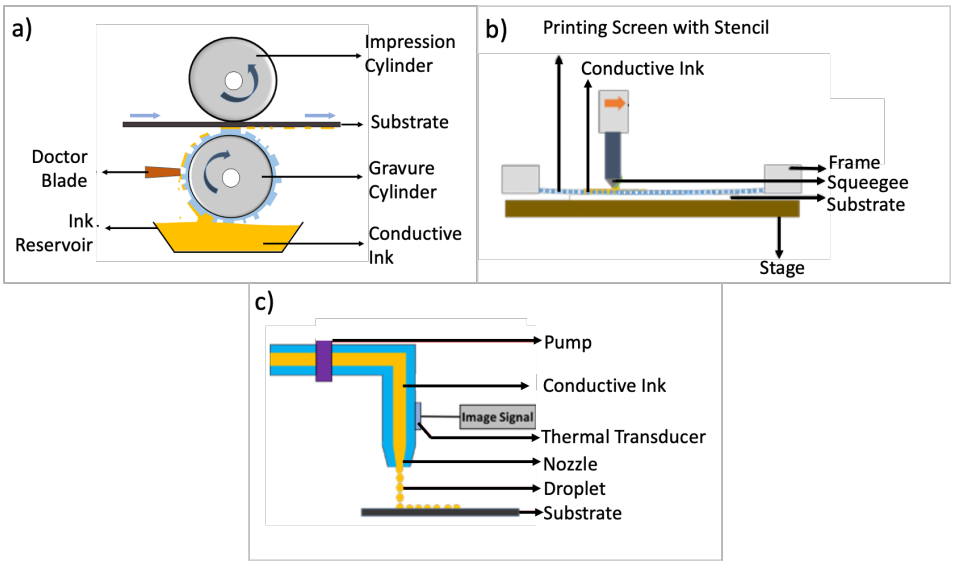

Figure 2.2 - Schematic diagram of a) gravure, b) screen, and c) ink-jet printing processes.

2.2 Other Materials for Printed Electronics

The essential component of PE technologies is a conductive ink, which can be also suspension composed of metallic or ionic particles linked by solving agents [44]. In fact, metallic solids are the most extensively utilized materials in flexible sensors, mainly because of high intrinsic electrical conductivity and commercial availability. Metals such as silver, copper, gold, platinum, nickel, chromium, magnesium, molybdenum, and aluminum are common active sensing elements incorporated into flexible sensors [45-47]. They are deposited on flexible films using traditional methods such as sputtering [48], electroplating [49], solution methods [50], and thermal/e-beam evaporation [51].

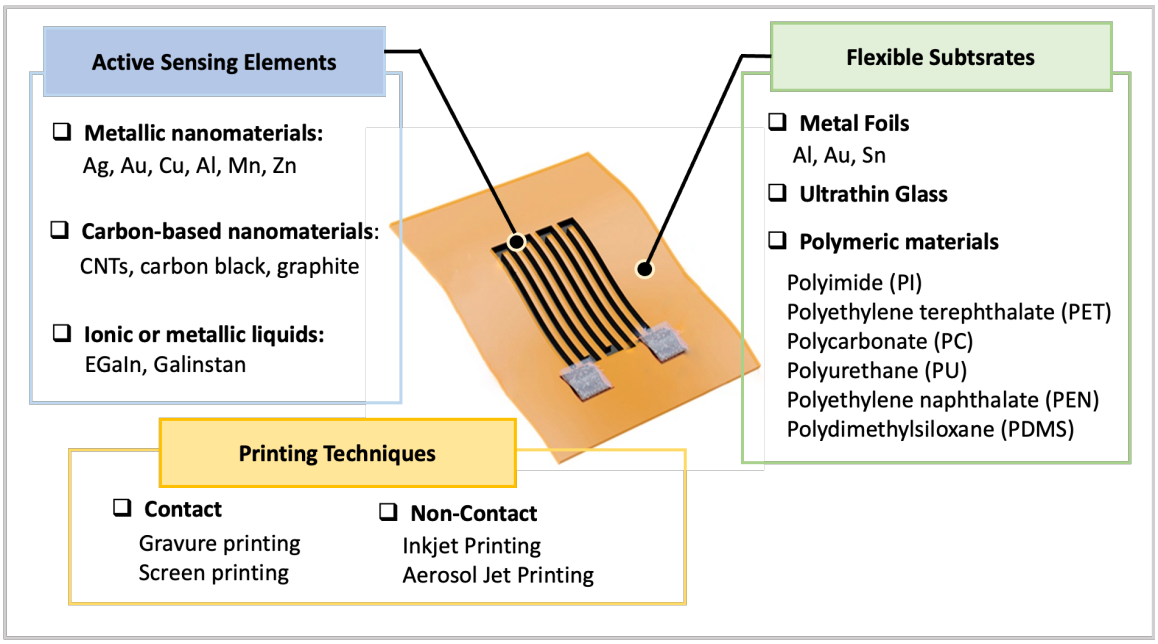

Figure 2.3 - Overview of common materials and printing techniques utilized for development of flexible sensors.

Although gold has been widely used as a thin-film contact to provide resistance to oxidation in air, it usually requires additional layers, such as titanium and chromium, to

improve the adhesion to the underlying substrates [52]. Mechanical and electrical properties of metallic solids also degrade gradually due to fatigue damage during repeated bending. To this end, metals of other geometries, such as nanowires and nanoparticles, were introduced to provide flexibility and mechanical stability [53-55]. The nanowires are commonly obtained using template/patterning (top-down method) or solution processes (bottom-up approach)[56]. However, the main limitations of these methods rise from underlying fabrication complexity and the presence of unwanted elements on the nanowire patterns [57].

In general, reducing the total loading of precious noble metals is highly desirable from both economic and geostrategic points of view. To this end, materials made of carbon, such as carbon nanotubes (CNTs), carbon black, reduced graphene oxide, and graphene, have gained considerable attention to develop thin-film transistors [58], flexible battery electrodes [59], and sensors [60, 61]. Among these, CNTs and graphene have been widely incorporated as active sensing elements in flexible sensors, mainly due to their fast electron transfer, remarkable strength, flexibility, lightweight, metallic and semiconducting properties. CNTs, large cylindrical molecules, are broadly classified into two categories, which are single-walled carbon nanotubes (SWCNTs) and multi-walled carbon nanotubes (MWCNTs) [62]. As the name suggests, the former is composed of a single cylindrical shell of the graphene sheet, while MWCNTs are made up of series circular cylinders of graphene. Arc discharge, laser ablation, and chemical vapor deposition (CVD) are conventional forms for fabricating CNTs[63]. The main drawback of CNT utilization is the lack of solubility in aqueous media and intricacies in handling [64].

Table 2.1 includes quantitative parameters for several of the materials used as active sensing components in flexible sensors.

Table 2.1 – Other active sensing elements commonly used for fabrication of flexible sensors.

Active Sensing Elements	Form/ Structure	Diameter (nm)	Length (nm)	Sheet Resistance	Ref.
Metallic nanomaterials (e.g., Ag, Au, Cu, Al, Mn, Zn)	Nanoparticle, nanowires, nanorods	2-400	200-1000	0.015–20 (Ω sq^{-1})	[35-37]
Carbon-based nanomaterials (e.g., CNTs, graphite)	Nanoparticle, nanowires, nanotubes, nanofibers	10-2000	500-5000	30-5×10^{6}(Ω sq^{-1})	[40-46]
Ionic or metallic liquids (e.g., eGaIn, Galinstan)	Liquid	Not applicable		2.63×10^{-9}-0.025 (Ω cm^{-1})	[28,29]

The utilization of flexible substrates considerably reduces the sensor weight and size while providing the ability to bend and roll into various shapes. There are several types of widely used flexible substrates: metal foils [65], ultrathin glass [66], ultrathin silicon[67, 68] and polymer films [69]. The former two have significant surface drawbacks, roughness, and low mechanical stability. Meanwhile, organic polymers have fast become a more viable option due to a higher degree of mechanical flexibility, conformability, and affordability in the purchase price and processing [70]. Some of the common polymers used to this end are polyimide(PI) [71-73], polyethylene terephthalate (PET) [74, 75] and polyethylenenaphthalate (PEN)[75, 76], and soft silicone elastomers [70, 75], among many others (see Table 2.2). Of these polymers, PI and PET are the most utilized for flexible electronics due to high chemical and thermal stability (average glass transition temperature of 360 ◦C), low coefficient of thermal expansion (3.4 ppm/K), nanometer-

scale surface roughness, as well as excellent dielectric properties [77]. Meanwhile, polydimethylsiloxane (PDMS) has dominated the field of stretchable sensing devices and electronics [77, 78]. Table 2.2 summarizes the various polymer films commonly employed for the fabrication of flexible and stretchable physical sensors.

Table 2.2 - Polymer substrates typically used for the fabrication of flexible sensors

Polymeric Substrates	Young's Modulus	Tensile Strain (%)	Poission Ratio (%)	Processing Temperture (℃)	Ref.
PI	2,500–10,000	<5	0.34–0.48	270	[56-58, 60]
PDMS	~ 0.36–0.87	>200	0.49999	70–80	[62, 63]
PET	2,000–4,100	<5	0.3–0.45	70	[59.60]
PC	2,600–3,000	<1	0.37	150	[60]
PU	10–50	>100	0.48–0.49999	80	[60]
PEN	5,000–5,500	<3	0.3–0.37	120	[60,61]

2.3 Laser-Scribed Graphene

Direct laser printing on commercial polyimide in ambient atmospheric conditions yielded multifunctional 3D graphene in 2014. This technology eliminates the need for costly cleanroom facilities, wet chemical processes, reducing agents, solvents, additional treatments, or other supporting processes by combining large-area graphene production and patterning in one fabrication step. This laser-scribed graphene (LSG) has stimulated research ranging from fundamental to applied sciences, investigating the laser graphitization process [79-81], effects of various lasers [82-84], environments [85, 86], and lasing parameters [87-89], to the development of flexible physical and chemical sensors. which also includes chemical recognition systems and surface functionalization to interact with analytic compounds [90-92], such as glucose[93], tyrosine [94], dopamine

[95], bisphenol [91], thrombin [96], ascorbic and uric acid [94]. The vast of the already available review articles [97-100] has concentrated mostly on LSG-based energy storage devices with electrodeposition [90, 101-103], an active catalyst with heteroatom doping [104-106], photodetectors with photosensitized materials integration [107], and biosensors with surface functionalization [108-110], all of which benefit from the high surface area of LSG and improved facilitation of electron transfer. In comparison, others focused more on reviewing laser-assisted processing of CVD graphene and its derivatives [111-114]. As a physical sensor, Tao et al. presented a LSG throat by showing slight changes in resistances to low pressures (<0.012 Pa) [115]; meanwhile, Yang et al. [94] and Luo et al.[116] reported the possibility of LSG to monitor heart rate and tactile sensing qualitatively. The majority of reported physical sensors utilized LSG as a strain sensor to qualitatively measure the bending of finger motion, as well as the angle of joints [107, 116, 117].

2.3.1 Transformation Process

The polymeric films could be transformed to porous graphene via laser photothermal (λ > 400 nm) or photochemical (λ < 400 nm) processes in two successive steps: carbonization and graphitization [98]. Amorphous tetrahedral or diamond-like carbon is created during the carbonization step. Meanwhile, the graphitization step is associated with converting the existing sp^3 bonds to sp^2 bonds, gaseous decomposition of products, and an increase in electrical conductivity [118]. Several laser types, polymers, and

environmental conditions that were used to obtain porous LSG films are listed in Figure 2.3

The composition of the LSG synthesis is heavily influenced by the propagation of the laser beam within in the substrate. After entering the polymer, the effective laser intensity is given by Equation 2.1.

$$I = I_o e^{-\alpha/z}, \tag{2.1}$$

where z is the penetration depth into the film, I_o is the initial intensity of the laser, and α is the optical absorption coefficient, which is strongly dependent on the wavelength of the laser. The precursors, such as PI [119] , PBM [120], PEEK [121], PEI [122], and PC

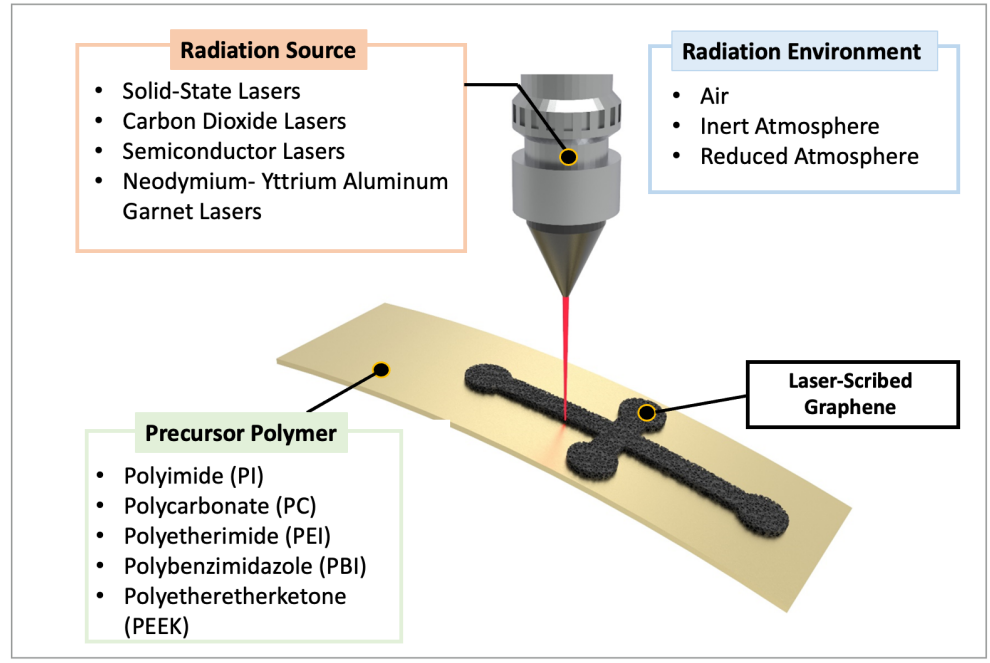

Figure 2.4 - Fabrication of LSG utilizing different radiation sources, precursor polymers, and radiation environments.

[123], share an ordinary aromatic ring in their molecular configuration that consists of carbon (C), Oxygen (O), hydrogen (H), and nitrogen (N), as illustrated in Figure 2.4. Their specific molecular structure influences the decomposition of gases during LSG formation.

The reaction that was observed during the LSG development is shown in Figure 2.4 [79]. The polymeric film is generally heated by a laser, inducing LSG, as well as CO, H_2 gases, and hydrocarbon ($C_xH_yN_z$) species.

Carbonization was reported to occur at 670 K, whereas graphitization happened at 770 K, using the most extensively used combination of a CO_2 laser and PI *[118]*. The gases generated from the conversion are eliminated from the system within 1.25 ns *[79]*. An amorphous structure is formed and transformed into ordered six-

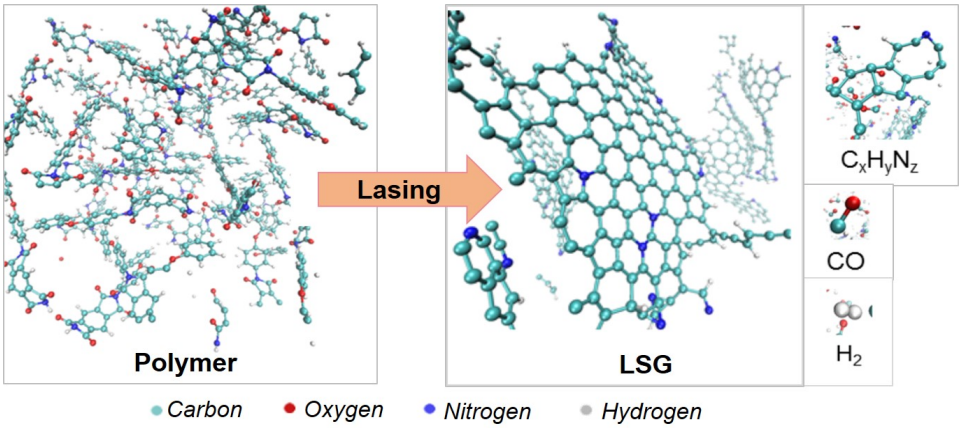

Figure 2.5 - Formation of LSG from polymer accompanied by the decomposition of species, such as CO, H2, and CxHyNz [61].

membered carbon rings, shown in Figure 2.5, within the initial 0.2 ns [79]. These results align with those reported by Lin et al., where TEM images revealed an ordered ring structure of graphene on PI (Figure 2.5b) [119]. Both investigations also noted uncommon formations that consist of five- and seven-member rings that may have resulted from steric stresses, the rapid formation, and cooling of the graphene, or trapping it in a higher energy state (Figure 2.5 c, d) [119] [79].

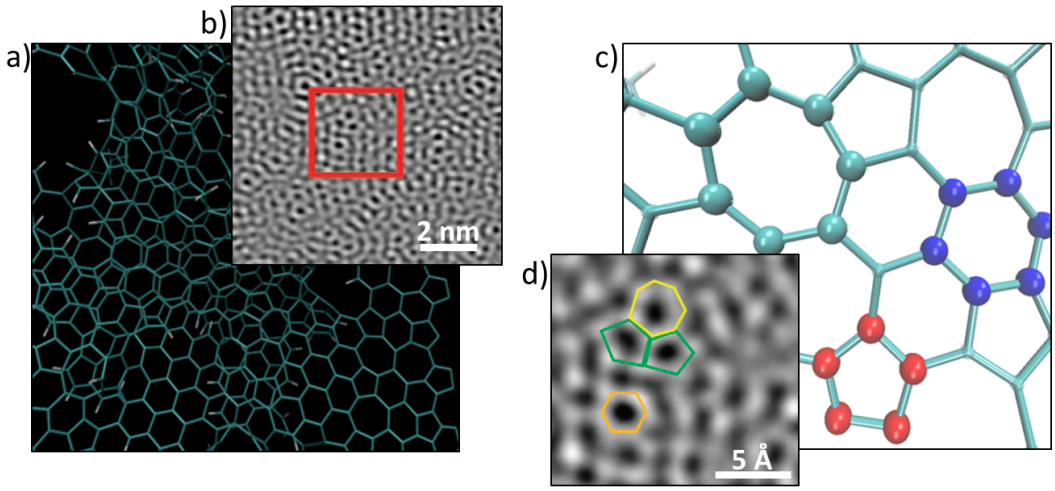

Figure 2.6 - a) Simulated and b) TEM image of polycrystalline LSG with grain boundary; c) Simulated and (d) TEM image showing the existence of different types of rings (5-, 6- and 7-member rings) LSG surface [61, 101].

The confirmation of LSG formation is typically done using Raman and X-Ray Diffraction (XRD) analyses. The 2D peak located around 2700 cm^{-1} in the Raman spectrum of LSG (Figure 2.6a) was recognized to be identical to one-layer graphene but with a wider width at half maximum of around 60 cm^{-1} [97, 124]. The XRD spectrum's prominent peak around 26° (002) suggested the production of a highly crystalline graphene structure (Figure 2.6b) [125, 126].

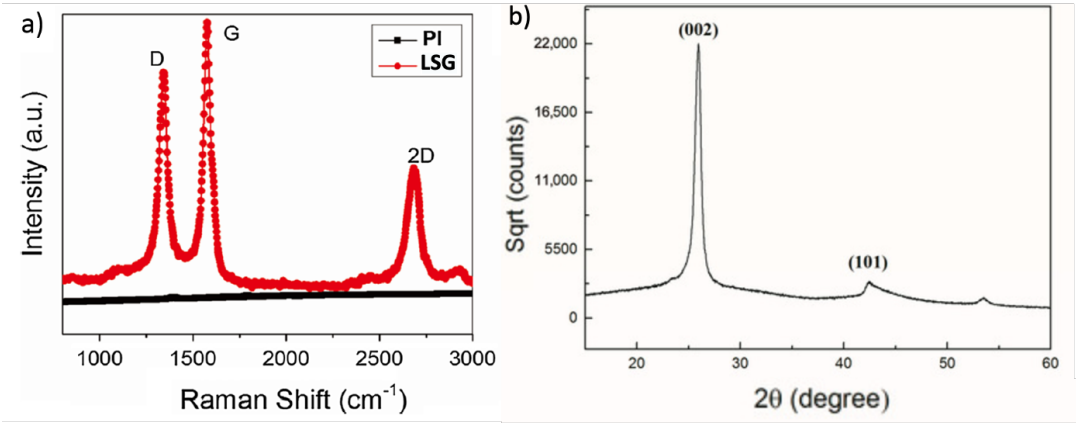

Figure 2.7 – Typical Raman spectra of LSG with prominent 2D peak [107] and f) XRD with a sharp (002) peak [79]].

Micro- and macro-manufacturing can be accomplished by scribing arbitrary geometries of customized shapes and sizes using software-controlled lasers. The lasing parameters, such as power (W), scanning speed (m/min), pulses per inch (PPI), and operational distance, z (mm), should be carefully tuned to obtain the desired morphology of LSG [122, 127]. 'Power' represents the energy magnitude at the laser nozzle, 'speed' defines the rate of motion of the nozzle over the substrate in the x-y directions, 'operational distance' represents the distance from the laser nozzle to the focal point of the laser on the film [116], while the 'PPI' parameter determines how many laser pulses per inch are used for the scribing.

2.3.2 Effect of Laser Parameters

Various combinations of CO_2 laser power levels and speeds have been previously used to form LSG as seen in Figure 2.7a. The heatmap of LSG electrodes over a wide range of power-speed combinations is illustrated in Figure 2.7b. The colors of red and orange indicate brittle electrodes obtained with high laser power and low speed. The polyimide which was partially or not carbonized at low power and high-speed settings is shown by brown colors [128]. Meanwhile, electrodes with a homogeneous texture and no damage from bending are characterized by the green color [128]. It was observed that the power has a linear relationship with the laser speed, i.e., an increased speed, necessitates an increased power to start the carbonization process [128-130]. Furthermore, the parameter sets can be varied as long as the threshold energy density, also called fluence, is achieved [117] . In the case of PI, the fluence of 7.9 ± 0.6 Jcm^{-2} is

required to initiate graphene scribing [77], which is in the range of previously reported energy estimations [89, 97, 117]. Tiliakos et al. have described a relationship between laser fluence, *F*, and laser parameters by

$$F = \frac{P}{\vartheta_x D}, \tag{2.2}$$

where, *P* is the power of laser, ϑ_x represents the laser speed in horizontal direction, and *D* stands for diameter of laser beam. The product $\vartheta_x D$ is the area scanned by the laser head per second [131, 132]. This also implies that a smaller spot size produces a larger fluence for the same amount of power. As can be seen from Table 2.3, the IR lasers emit the lowest threshold fluence, while UV lasers have the highest. The morphology of LSG can be tuned by altering the laser fluence, such that above a certain fluence, graphene fibers of approximately 1 mm in length and 100 nm in width emerge from the substrate as seen Figure 2.8 [133].

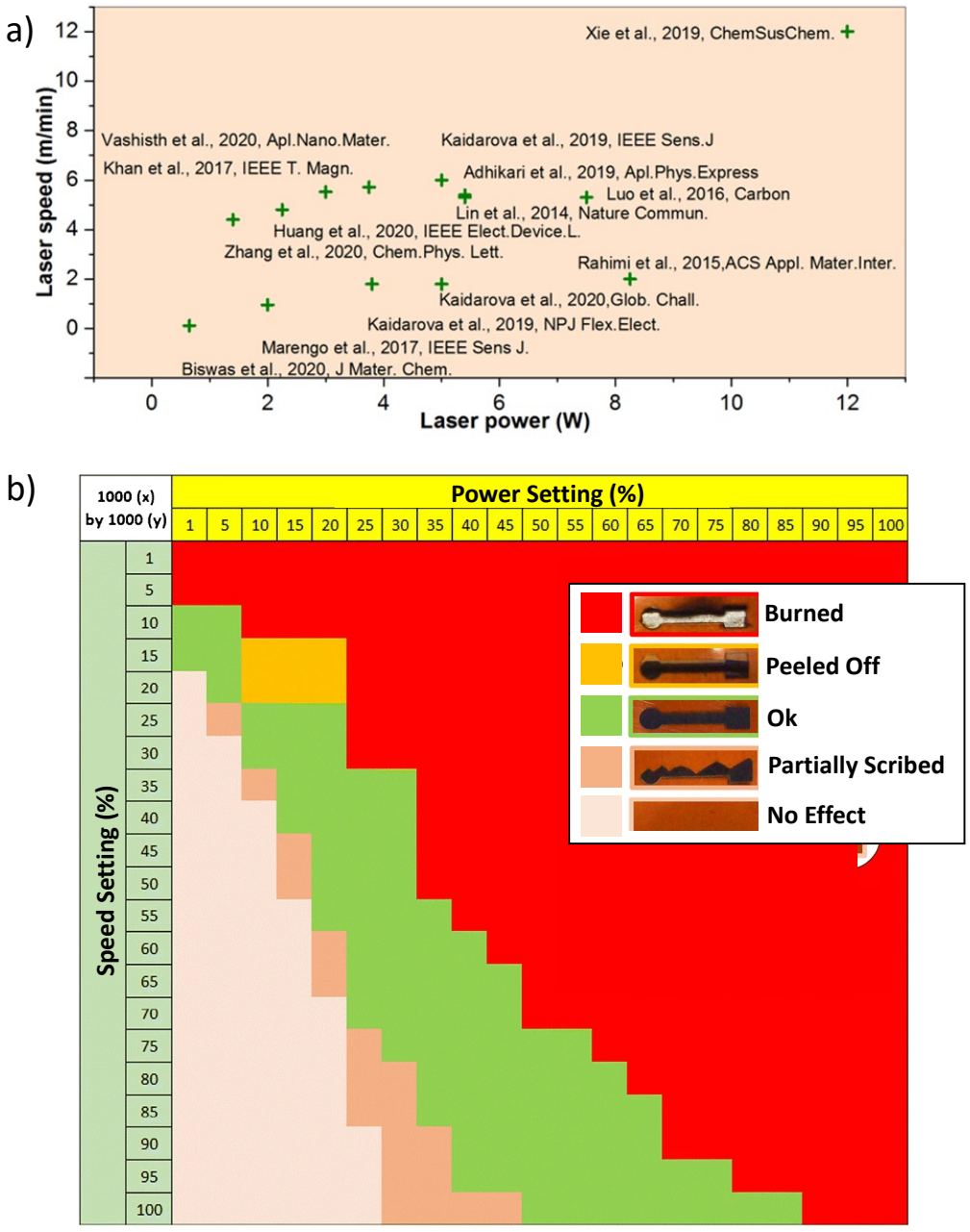

Figure 2. 8 - a) Overview of typically reported power and speed of CO2 laser to obtain LSG. b) Heatmap of LSG outcome at various power(1 to 100% of 30 W) and speed settings (1% to 100% of 76 m/min) and 1000 PPI[128].

Table 2.3 - Overview of the lasers and corresponding threshold fluence, power and spot sizes utilized for LSG fabrication.

Optical region	Type	Wave length	Manu-facturer	Model	Threshold Fluence & Power	Power (W)	Spot Size(µm)
IR	CO_2	10.6 µm	Universal Laser Systems	PLS 6.75	(0.50 ±0.03) W (7.88±0.47) Jcm^{-2}	10-75	~60 -150
				PLS 6MW			
				XLS10MWH		10-150	
				VL-300		30 -50	
				VLS 2.3		10-30	
			Coryart	Microlaser C40		40	
	Nd: YAG	1064 nm	DMG Mori	Lasertec 40		100	
Visible (blue-violet)	Laser Diode	450 nm	OSRAM		0.161W, 83.4 Jcm^{-2}	1.6	>12
			Nano Pro III			0.5-5	
		405 nm	Q-BAIHE	405 ML-300e2290		0.015-0.3	
			Laser Co.	M-33A405-500-G,91		0.5	
UV	Nd: YVO4	355 nm	Inngu Laser	n/a	0.3W 15 J cm^{-2}	<40	~30-60

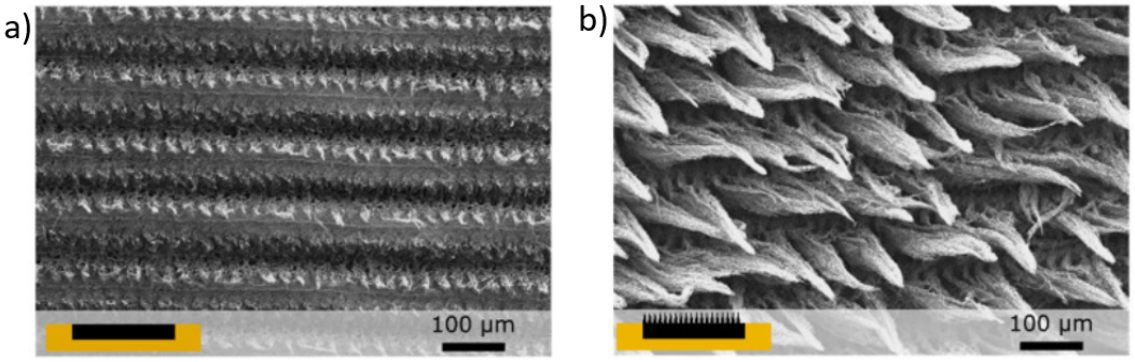

Figure 2.9 - The morphology of a) porous and b) fibrous obtained by tuning laser fluence [119].

Laser parameters also influence the resultant sheet resistance, conductivity, crystallite size, thickness, and wettability of LSG. For example, based on the applied power of the CO_2 laser, the sheet resistance of graphene can vary from 5 Ωsq^{-1} to 115 Ωsq^{-1}, and conductivity can be in the range from 500 Sm^{-1} to 2500 Sm^{-1} [89, 134]. An

excrescent laser power or speed, however, induces the rise of defects and oxidation of the graphitic tracks, which usually result in a reduction of conductance, as shown in Figure 2.9 [80, 117]. The laser power also impacts the average line width, thickness, and crystallinity of LSG. The thickness of porous graphene could be from 20 µm to 100 µm [80], line width can extend from 110 µm to 240 µm [116], and crystalline size could vary from 20 nm to 40 nm [118].

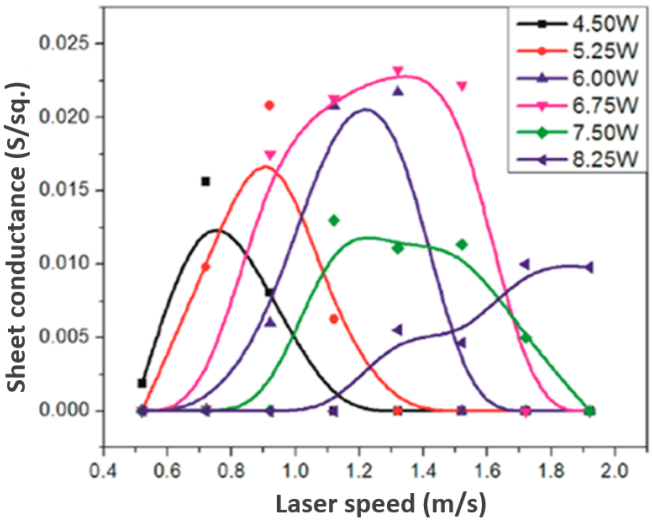

Figure 2.10 - Conductance of carbon traces on PI versus laser fabrication parameters [117].

The scanning speed and frequency of the laser incident radiation can also affect the wettability of porous graphene. [88]. A superhydrophobic surface of LSG with contact angles of > 150° was obtained when laser speed surpassed 12 m/min and frequency of 20 kHz. These laser parameters stimulated a distinct structure displacement and gas evolution in PI, impacting its conduction characteristics [88, 135]. These observations are consistent with the wettability properties of carbon-based materials, which are exceedingly magnified by the nano-morphology of the LSG foams [135].

2.3.3 Choice of Laser

A summary of the lasers that have been used for the fabrication of 3D porous graphene from PI is shown in Table 2.4.

Infrared laser. The dissociation of CO_2 molecules in electric discharges provides substantial laser energy at IR wavelength (10.6 μm, 943.40 cm^{-1})[136-138]. The IR laser couples to carbon bonds existent in the polymer and offers effective photothermal heating [139-141]. The rastering capability of the laser allows the graphene scribing into various shapes and sizes. Considering that more than 90% of IR at this wavelength of 10.6 μm is absorbed by the upper surface of PI, the carbonization commences immediately after the photon penetrates it. This leads to the topmost parts of the polymer evolving into graphene, while the bottom part stays unalloyed and functions as mechanical reinforcement. Biswas et al. in-depth examined the conversion of PI into LSG using a CO_2 laser[118]. It appeared that carbonization of PI takes place at a threshold power of (0.21 ± 0.02) W and a fluence of (3.31 ± 0.32) Jcm^{-2}, while graphitization eventuates at a power of (0.50 ± 0.03) W and a fluence of (7.88 ± 0.47) Jcm^2 [118]. Furthermore, near IR lasers, such as Nd : YAG (1064 nm), could be incorporated into a compartment with environment control and supplied with a rapid galvo-scanning apparatus with a nanosecond pulse for quick prototyping and mass production [84]. Graphitization was not detected on PI substrates under defocusing conditions and insufficient laser energy. The limitations associated with the spot size and diffraction of infrared lasers result in graphene line widths of from 100 μm to 150 μm.

Meanwhile, increased line width (>150 μm) is indicative of a larger spot size associated with defocusing distance and sufficient energy.

UV lasers. The energy of radiation is inversely proportional to its wavelength. In the near UV region (< 400 nm), the photochemical effect considerably affects the formation of LSG by eliminating the oxygen residuals from the LSG structure [98]. In contrast to the photothermal effect, the chemical bonding can be directly broken by the absorbed photon energy, particularly when it exceeds dissociation energy [142]. Although UV lasers were first used for graphene oxide reduction (with a threshold power of 15 kW cm^{-2}), they have now been utilized for direct scribing of graphene to prevent considerable PI heating [143]. Due to smaller wavelengths, UV lasers are capable of focusing on smaller spot sizes than IR lasers. Carvalho et al. have produced LSG with a UV laser using the power of 0.3 W and a fluence of 15 J cm^{-2} [82]. Meanwhile, the resultant LSG resolution ranged from 30 μm to 50 μm with a thickness of ~5 μm [86, 144-146].

Visible blue-violet lasers. An enhanced feature has been recently achieved with the visible 405 nm laser, providing a minimum resolution of ∼12 μm [144]. Stanford et al. reported a significant absorption of visible blue-violet light photons, making visible light lasers appealing for the photothermal transformation of polymers to LSG. The obtained LSG thicknesses of near 5μm are comparable to LSG fabricated using UV lasers [144]. A threshold energy of 83.4 Jcm^{-2} and power of 0.161 W were needed to obtain LSG from a single pulse laser exposure. As can be noted from Table 2.4, visible lasers also use reduced powers, which serves as a commercial advantage.

2.3.4 Influence of Lasing Environment

The environmental conditions during lasing affect the pore size, conductivity, and thickness of the LSG, as well as hydrophobicity and hydrophilicity of the LSG films [85] [86] [147]. Cai et al. examined the effect of air and inert gases on the resultant scribed graphene [86]. It appeared that when the laser scribing environment is exposed to air, the graphene formation is accompanied by an oxidation process, which leads to thicker LSG substrates and rougher surface morphologies. The resultant micrometer-sized pores were widely distributed across the LSG with high oxygen content [86].

The oxidation process, nevertheless, can be effectively minimized in an inert environment, such as Ar. The inert atmosphere promotes the emergence of relatively thinner LSG substrates, smoother surface morphologies, narrower pore size distribution, higher carbon lining, and conductivity [86]. The surrounding environment facilitates significant changes in the water contact angle on the LSG, from 0° (superhydrophilic) when using O_2 or air to > 160° (superhydrophobic) when using inert or reducing gases (Ar, H_2, or SF6) [85]. Li et al. reported that distinct wetting properties are due to the alternations in surface morphology and surface chemistry of LSG structures. The scribing in a controlled gas environment mimics the conventional CVD process for the growth and modification of graphene properties but substitutes the high-temperature oven heating by laser irradiation [148].

Chapter 3

Realization and Properties of LSG Electrodes

3.1 Fabrication Process

The process begins with cleaning the surface of commercial PI film of 125 µm thickness (Kapton # IM301449, DuPont, Delaware, USA) with ethanol and drying with clean air/nitrogen gas. The electrodes pattern are then designed on a computer with vector graphics software, such as CorelDraw or AutoCAD. The sensors are realized by direct laser scribing using a CO_2 infrared laser (wavelength 10.6 µm, laser spot diameter ~150 µm, Universal Laser Systems® PLS6.75) in ambient condition, as illustrated in Figure 2.3. Laser beam parameters are tuned to obtain good adhesion of the carbon network to the substrate and achieve the porous morphology with the minimum electrode width of ~150 µm (corresponding to the laser spot diameter). In particular, the following laser beam parameters have been used often: 3.6 W power, 3 cm/s speed, 1000 pulses per inch, and 3 -mm laser-to-surface distance. The resultant LSG electrodes are shown in Figure 3.1a, as an illustrative example. Depending on the application, a stable and reliable wire connection is established by one of the following means:

1. *Adhesive connection:* Conducive epoxy (CW2400, CircuitWorks, Inc) is used to connect the electrical wires because it has strong mechanical connections, high electrical conductivity, and cures quickly at room temperature; In order to prevent epoxy from penetrating the pores of graphene and causing structural

damage, thin layer of gold (~100 nm) is sputter-deposited on top of the graphene contact pads (Q300T, Quorum), as seen in Figure 3.1a and Figure 3.2b.

2. *Mechanical connection:* Holes of 120 µm in diameter are created in the LSG electrode using 30 W of CO_2 laser power and 20 cm s^{-1} speed, followed by mechanical threading of wires through the holes (Figure 3.1b and Figure 3.2c).
3. *Vias connection:* Holes of 400 µm in diameter are created in the LSG electrodes using 30 W of CO_2 laser power and 20 cm s^{-1} speed. Vias are then inserted to establish robust electrical connection between LSG and any printed circuit board (Figure 3.1c and Figure 3.2d). Conductive epoxy (CW2400, CircuitWorks. Inc) was utilized to fill holes of the vias and ensure more reliable assembly yields.

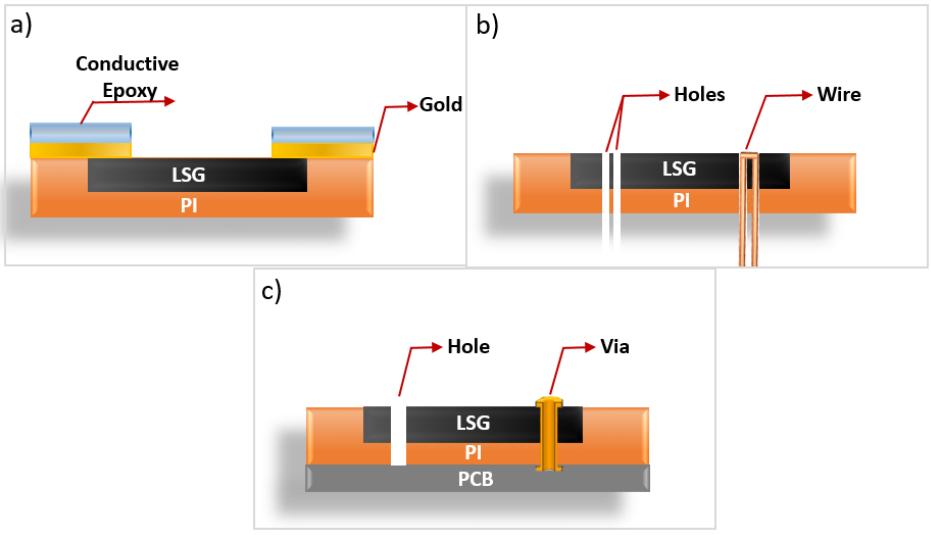

Figure 3.1 The cross-section of LSG electrodes with a) adhesive, b) mechanical, and c) vias connections.

Optionally, a coating material can be applied to protect porous graphene from desquamation; and, when deployed in seawater, to avoid damage from biofouling and

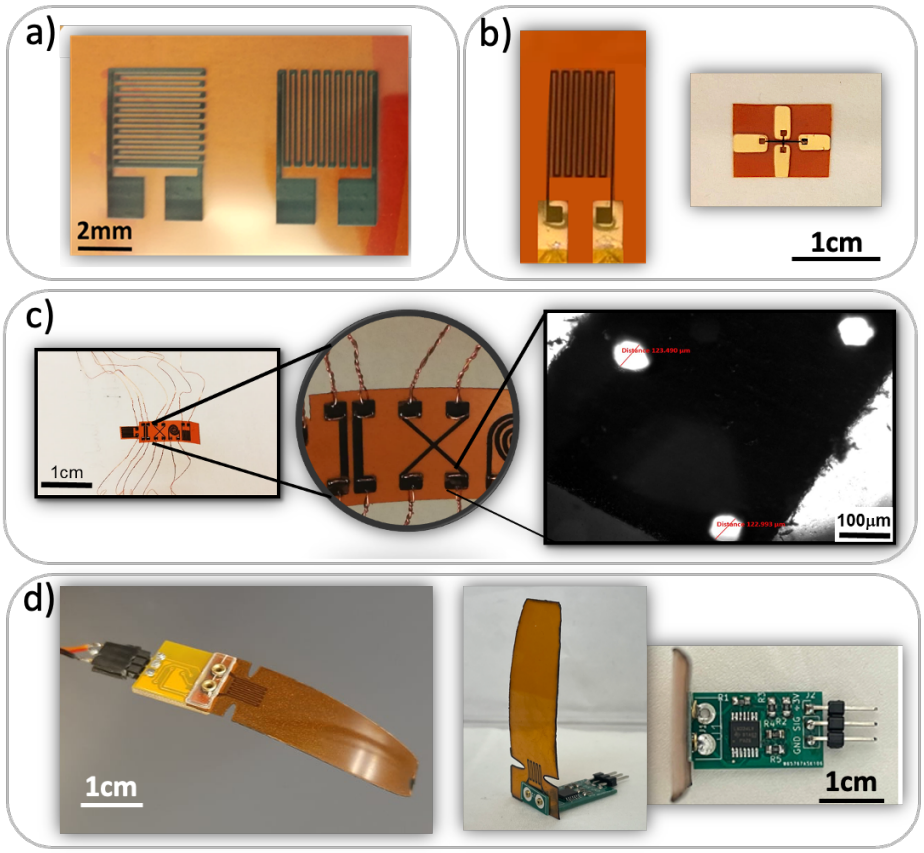

Figure 3.2 – a) LSG electrodes realized using b) adhesive c) mechanical and d) Vias contact pads.

interference with the measurement due to shunt currents. The following coatings are particularly useful in these regards:

1. Polydimethylsiloxane (PDMS, Dow Corning Corp., Slygard® 184) with a ratio of 10 (base):1 (curing agent) is spin-coated on top (2500 revolutions per min for 90 s) of the device and placed in a vacuum desiccator for 20 min to eliminate air bubbles. The passivation layer is cured in the oven at 80 °C for 1 hour. The obtained thickness of the PDMS is approximately 10 µm.

2. Parylene C (poly(dichloro-p-xylylene)) coating is applied using a vapor deposition technique (PDS 2010 Parylene Deposition System). With a Parylene granule of 2 mg, a coating layer thickness of approximately 1 µm is obtained.
3. Polymethylmethacrylate (PMMA, Kafrit, Inc.) of 15 µm is thermally laminated on top of an LSG structure with a 4 min. warm-up time (P42DE-WE, Atlas, Inc.). When a relatively rigid material like PMMA (E ~ 3.2 GPa) is applied on top of the LSG-PI stack, the stress gets transferred to the LSG upon applying pressure, which provides a pathway for insulating and passivating the sensor.

3.2 Physical Characterization

Scanning electron microscopy (SEM, Quanta 600FEG Systems), confocal Raman microscopes (Alpha300AR+, WITec), and X-Ray photoelectron spectroscopy (XPS, ESCA 3400, Amicus Kratos) were used to examine the morphology of the LSG electrodes.

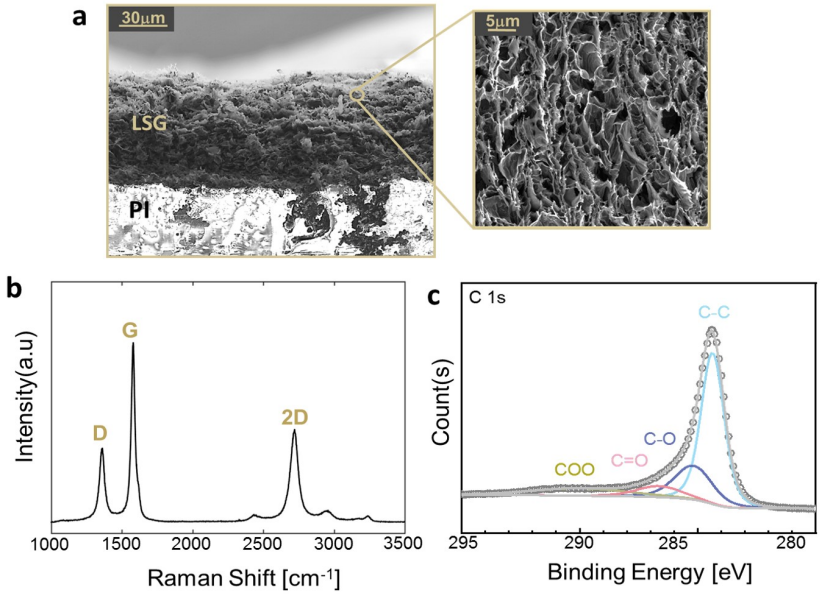

Figure 3.3 - a) SEM image of cross –section of LSG. Inset shows a high-magnification SEM image where graphene flakes are randomly arranged and interconnected. b) Raman spectrum of LSG acquired with a 473 nm laser. c) High-resolution XPS spectrum

Figure 3.3a shows a low magnification SEM image of an LSG cross-section, revealing a porous and carbonized structure of 60m thickness on top of the residual PI. The SEM image of the LSG under high magnification (inset) indicates that the entire volume is comprised of multilayer graphene sheets with a high porosity. Meanwhile, the Raman spectroscopy of the LSG reveals three distinctive peaks at 1360 cm^{-1} (D-band), 1580 cm^{-1} (G-band), and 2720 cm^{-1} (2D-band) and thereby, suggesting the presence of graphene sheets in the porous structure (Figure 3.3b). The G peak is related to the vibration of sp^2 carbon atoms in the hexagonal plane [149]. Disorder and defects stimulate D peak, which is associated with intravalley double resonance mechanisms [150]. The 2D peak is responsive to the order of the graphene stacks along the c-axis. It is the key one in monolayer graphene that can result from laser-induced graphene structures [151]. This result is supported by the XPS spectrum (Figure 3.3c), which shows a prominent C—C peak, with greatly suppressed C—O, C = O, and COO peaks, suggesting the dominance of sp^2-carbon in the LSG and breakage of these chemical bonds [152].

3.3 Repeated Laser Writing

The graphene electrodes were formed by repeatedly laser scribing on a 125 m polyimide (PI) substrate (DuPont, Kapton #IM301449) in ambient environment using pulses from a CO_2 laser (ULS, PLS6.75). A maximum of 5 iterations of repetitive laser writing were used to scribe the samples. To evaluate the degree of graphitization and defect formation for the LSG electrodes after each laser writing step, confocal Raman spectroscopy (Alpha 300 Apron, Witec), scanning electron microscopy (SEM, Nova Nano

630 Systems), X-ray photoelectron spectroscopy (XPS, ESCA 3400, Amicus Kratos Analytical), and X-ray diffraction (XRD, D2 Phaser, Bruker) were utilized. Figure 3.4a shows Raman spectra acquired with an excitation laser source of 532 nm under 5 mW power.

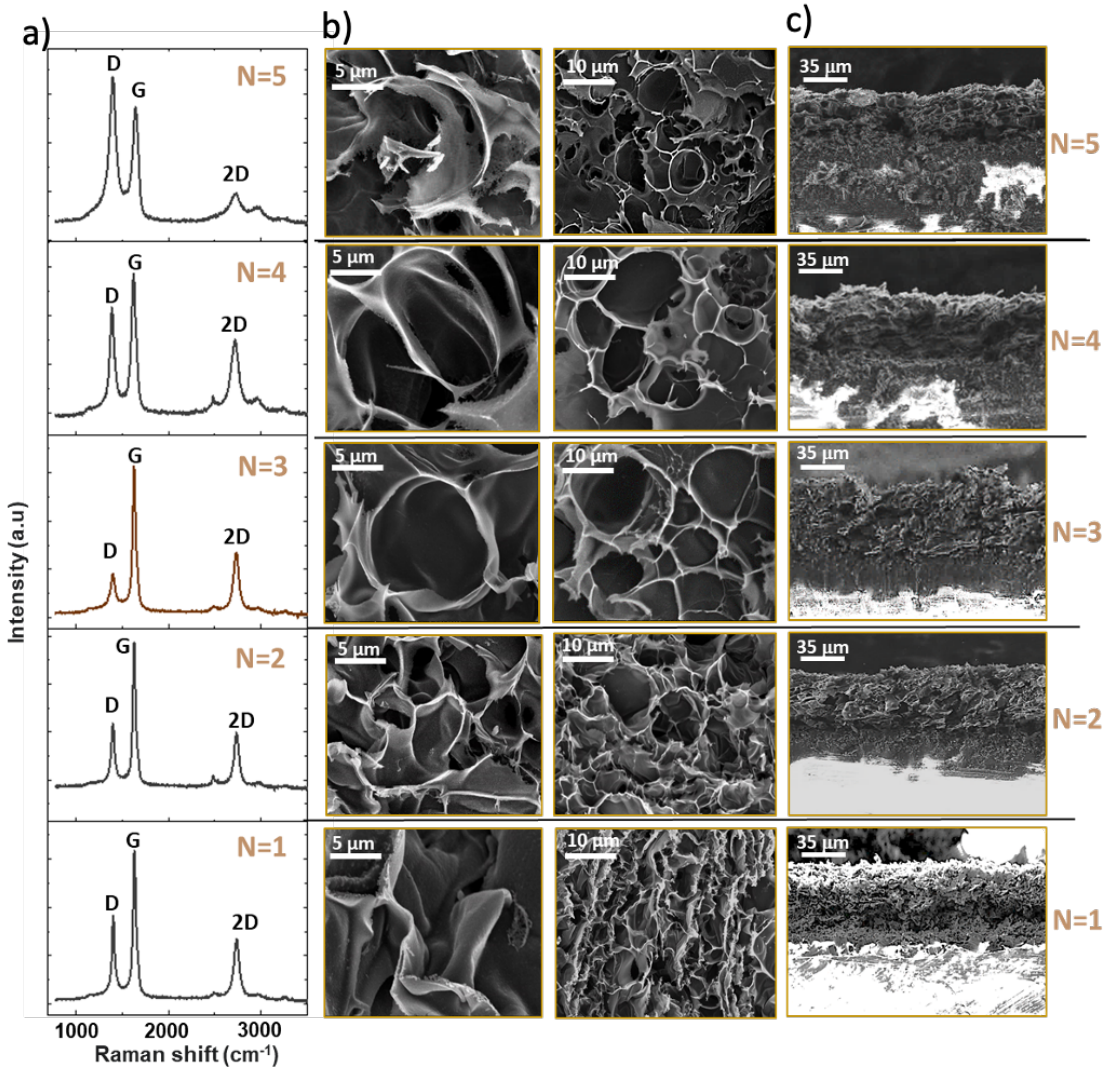

Figure 3.4 - a) Raman spectrum of LSG for N consecutive laser irradiations. b) Top-view and c) cross-sectional SEM images of porous graphene structures after each laser irradiation step.

Even after four times repeated lasing, three distinct peaks at approximately 1360 cm^{-1} (D-band), 1584 cm^{-1} (G-band), and 2730 cm^{-1} (2D-band) can be recognized, indicating

LSG development. [79, 82, 139]. The ratio of their intensity (I_D/I_G) is commonly used to quantify the amount of defects in the graphitic materials [153]. In our case, the ratio I_D/I_G decreases from 0.79 to 0.26 after three-time repeated laser writing, indicating reduced structural defects, lower edge densities, and higher quality of the obtained graphene. These results are further verified by SEM images, which show more polyporous and looser surface morphologies obtained after three repeated laser scribing steps (Figure 3.4b). The higher porosity observed suggests more air and less LSG in the same volume. Indeed, the weight of the LSG sample dropped by 35% after three laser writing, measured using an electronic weighing scale (BSA 224S-CW, Sartorius), as shown in (Table 3.1). Each successive lasing step also led to an increased resistance, which also suggest the dominance of the effect of increased porosity [154, 155] (More details in Chapter 5.2)

Table 3.1 - The effect of multiple laser writing on the physical and electrical performance of LSG strip (L= 20 mm).

Multiple lasing	LSG Width (µm)	LSG Thickness (µm)	Mass (mg)	Resistance (Ω)	Sheet Resistance (Ω/sq)	Conductivity (Sm^{-1})	GF
N=1	263	60	8	1,023	13.5	1238.93	10.7
N=2	288	76	7	1240	17.9	736.9	43.6
N=3	295	90	6	2010	29.7	374.8	91.2
N=4	298	130	5.5	3347	49.9	154.2	85.3
N=5	310	135	5	6900	106.9	69.3	44.4

The consecutive laser writing (four and five-times), however, introduces damages to the LSG structure and non-uniform graphene distribution across the PI thickness (Figure 3.4c), which is consistent with an increased intensity of the D- band in the Raman spectra.

Meanwhile, the ratio I_{2D}/I_G is less than 1 for all repeated laser writing samples, which implies the existence of multilayered graphene [156].

Using Raman spectroscopy results and Equation 3.1 , the crystalline size of LSG, $L_{a,}$ can also be estimated [119]:

$$L_a = (2.4 \times 10^{-10}) \times (\frac{I_D}{I_G})^{-1} \times \lambda_{l,}^4 \quad (3.1)$$

where λ_l is the wavelength of the Raman laser (λ_l = 514 nm), the L_a values reach ~60 nm after three laser writing steps (Figure 3.5a). A further increase in the number of laser writing steps degrades the quality of the LSG with a L_a of 21 nm, which is attributed to the broken LSG bonds and partial oxidation of LSG in the air.

XPS was used to examine the elemental composition of the LSG after each repeated laser writing step. XPS spectra of samples showed the signature of the major elements carbon (from the aryl group) and oxygen (from the ketone and ether bonds) only, as shown in Figure 3.6. The C/O ratio has increased by ~37% after three laser writing steps, indicating an increased amount of carbon and decreased oxygen elements (Figure 3.5b). Figures 3.5c and d show a high-resolution C-1s peak of the XPS spectrum and an XRD pattern for LSG after three times of laser writing, respectively. Deconvoluted C-1s peak shows a prominent C-C (284.8 eV) peak with considerably reduced C-O (285.4 eV), C = O (286.2 eV) peaks, suggesting the predominance of sp^2 carbons agreeing well with Raman spectra results [157].

Meanwhile, XRD of powdered LSG shows a peak centered at 2θ=26.02° and 2θ=42.9°, both of which correspond to previously reported LSG [119] [101]. The interlayer spacing between (002) planes can be derived using Bragg's equation

$$\lambda=2d\sin(\Theta), \tag{3.2}$$

where λ is the wavelength of the X-ray beam (0.154 nm), d is the distance between the adjacent LSG sheets or layers, Θ is the diffraction angle. As shown in Figure 3.5d, the

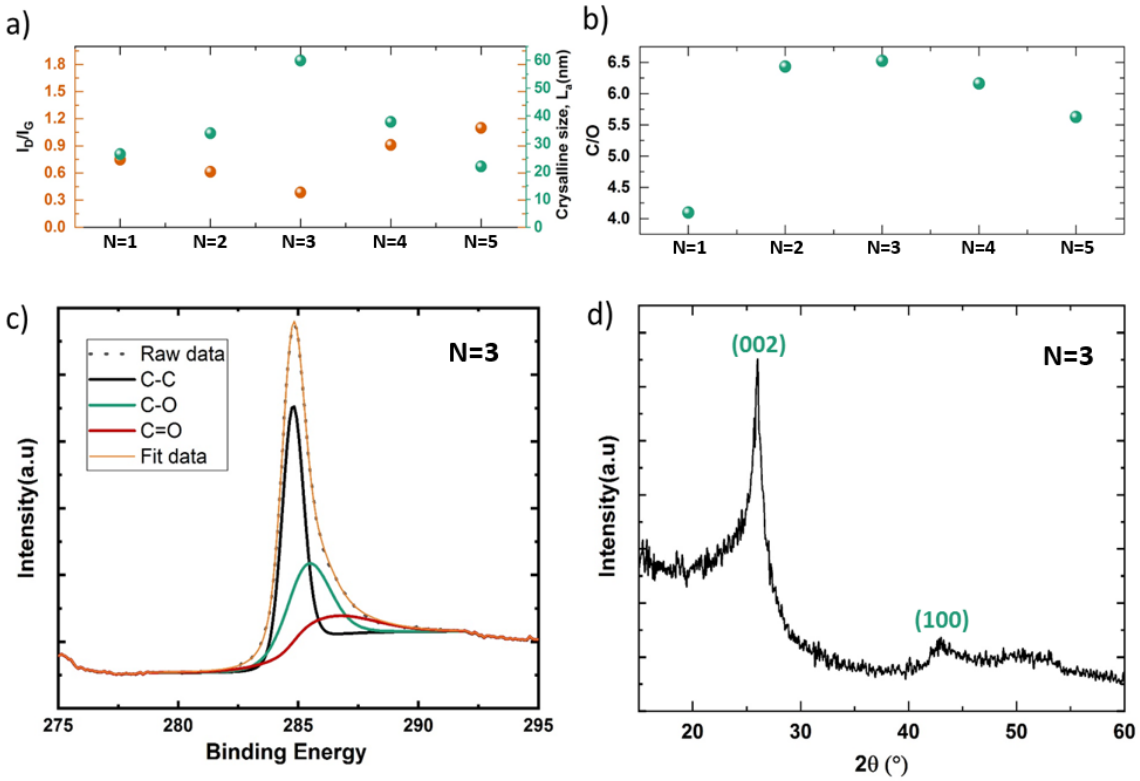

Figure 3.5 - a) The G and D peak intensity ratios and average domain size as a function of repeated laser writing; b) C/O ratio as a function of repeated laser writing; c) High-resolution XPS spectrum. d) XRD of powdered LSG after three times of laser writing.

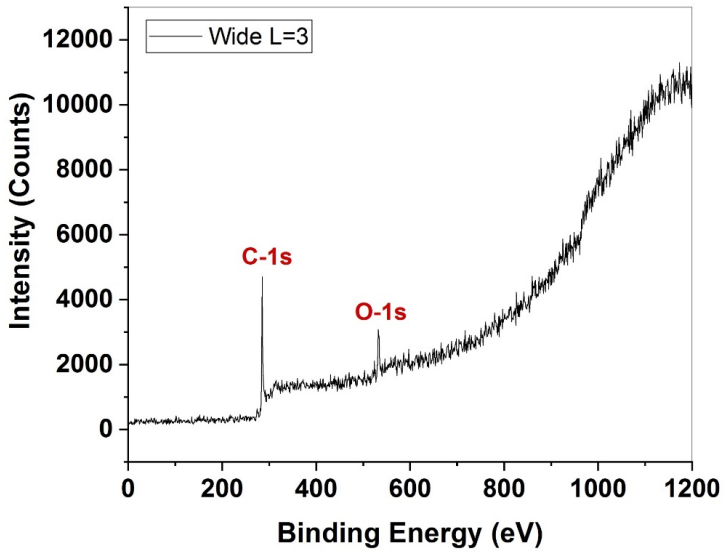

Figure 3.6 - XPS spectra of samples show the signature of the major elements carbon from the aryl group and oxygen from the ketone and ether bonds.

diffraction peak position is at 2Θ= 26.03°, representing the (002) planes. Therefore, the obtained interlayer spacing of 0.342 nm (d = λ/2 sin(Θ) = 0.154 nm/2sin(13.015°)) between (002) planes suggests a high degree of graphitization [119].

3.3 Biocompatibility

The biocompatibility of the LSG electrodes was assessed using HCT 116 cells and two methods: coulometric assay (alamarBlue cell viability assay) and confocal microscopy. The alamarBlue assay was used to quantify the cell viability, while the LIVE/DEAD fluorescence staining method (calcein for live cells and ethidium homodimer-1 for dead cells) was used to visualize the cell viability. The preparation methods of the samples were as follows:

- Cell culture. HCT 116 (ATCC CCL247) cells were cultured in McCoy's medium 5A 1× with a l-glutamine with 10% fetal bovine serum and 1% penicillin-streptomycin.

For detaching and counting the cells StemPro Accutase and trypan blue have been used, respectively. The cells were grown inside of a 37°C, humidified incubator with 5% CO2. All of the supplements and the media were bought from GIBCO life technologies.

- Cell viability tests. The LSG electrodes were placed on 48-well plate (for AlamarBlue assay) and 6-well plate (for confocal) and washed three times with ethanol followed by three times with 0.01mM PBS and three times with McCoy's medium. Then, 700 000 cells were seeded on top of the LSG for 24h. For confocal imaging: the culture medium was removed after 24 h and exchanged with 0.01M HBSS (GibcoTM HBSS without Calcium, Magnesium or Phenol Red), and then the cells were stained for 20 min at room temperature with LIVE/DEAD® Viability/Cytotoxicity Kit (Molecular ProbesTM; Eugene Oregon, USA). After that, the LSG was washed with HBSS and investigated immediately under the confocal. AlamarBlue assay: the culture medium was removed after 24 h and exchanged with a fresh one (200 µl), and then AlamarBlue cell viability assay (Cat. No. DAL1025) was used. Based on the vendor's protocol, 22µl of AlamarBlue reagent was added directly to the well and incubated for 2h at 37 °C. To analyze the data, the absorbance Bio-Rad microplate reader was used at 570 nm. Both experiments were done in six replicates.

The coulometric assay results are presented in Figure 3.7a, showing high biocompatibility of the LSG electrodes by maintaining high cell viability (>90%), which is considered as non-

cytotoxic according to ISO standards [158, 159]. The result is not significantly different from the control after 24h of incubation. In addition, the fluorescence staining method revealed the ability of HCT 116 cells to grow in a confluent way on the sensor (Figure 3.7b). Most of the cells on the sensor were calcein-stained 24h after growth, indicating high biocompatibility similar to the control (Figure 3.7 c). The control shows the viability of cells growing on a cover slide, while the sample shows the viability of the cells growing on top of the sensor. Error bars represent the standard deviation of six replicates. $p > 0.05$.

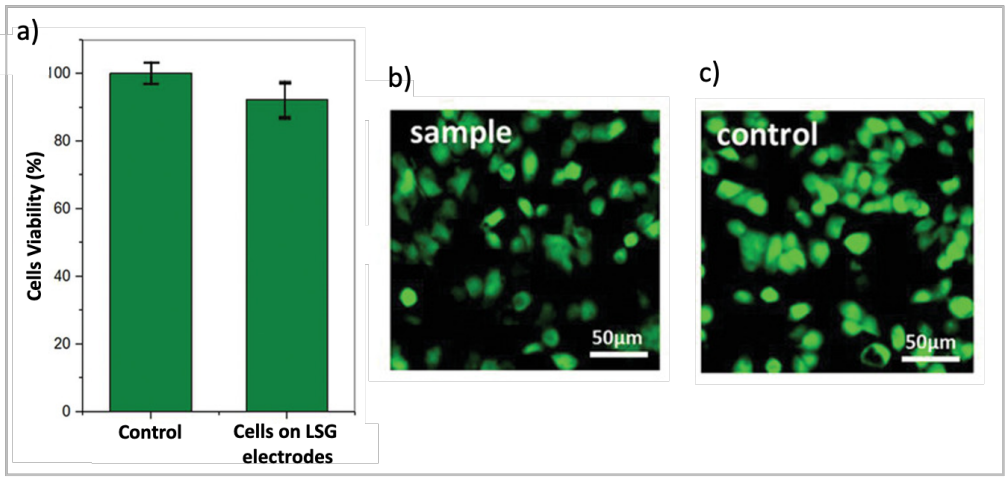

Figure 3.7 - Biocompatibility assessment of the sensor. a) AlamarBlue assay and b,c) confocal images show the viability of HCT116 cells to grow on top of the sensor after 24h.

3.4 Exposure to Harsh Environments

The operation of LSG electrodes under high temperature, high pressure, and in a seawater environment is presented as an illustrative application to cope with harsh environments. The effect of temperature on the LSG was evaluated by thermal

gravimetric (TGM) analysis, which involves the detection of the mass change caused by a temperature increase. As seen in Figure 3.8, the LSG was able to withstand temperatures of at least 400 °C. There was a substantial drop in mass after ~500 °C, mainly due to evaporation, sublimation, and increasing pressure in reacting environments [160].

The Red Sea is the warmest (up to 36 °C in surface waters [161]) and saltiest (20% above standard ocean salinity [162]) of all seas and offers conditions prone to corrosion and pressure-derived failure of electronic devices. To compare the performance of LSG electrodes with noble metals (e.g., gold), two sensor electrodes with the same shape were fabricated using laser technology and immersed into the Red Sea, highly saline water of ~30 psu (Figure 3.8b and 3.8d). The fabrication of gold electrodes requires a multi-step process. Firstly, the sputtering system (Q300T, Quorum) was used to deposit 100 nm of gold on the PI surface. The excellent adhesion of sputtered gold on untreated PI has already been studied and proved to be resistant to solid-state dewetting during annealing [163]. Subsequently, a Yb fiber laser (Universal Laser Systems® PLS6MW) was used to selectively remove the gold, exploiting a recently developed patterning technique [164], reproducing the same geometry used for the LSG sensor without damaging the PI. The gold electrodes were heavily damaged after only one measurement in seawater, whereas the LSG showed excellent stability even after many exposure cycles, showing its outstanding durability in the seawater, as can be seen in Figure 3.8c and e.

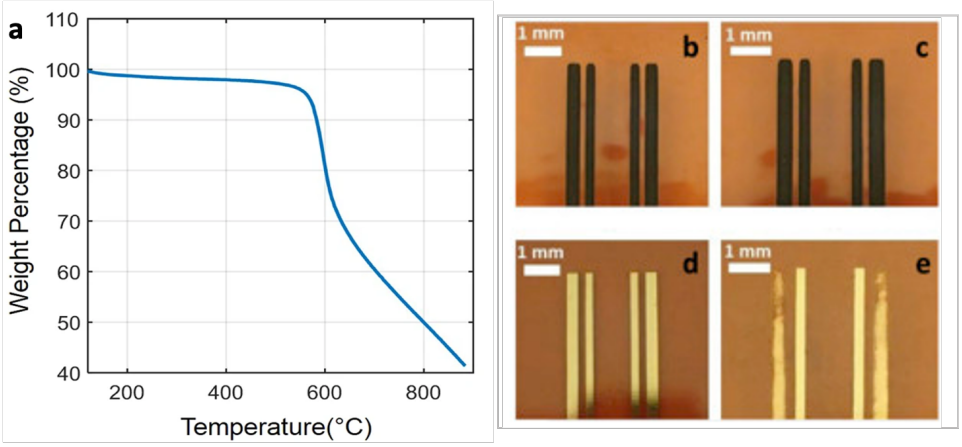

Figure 3.8 - a) TGM analysis of a LSG on PI in a nitrogen atmosphere. b) LSG electrodes before exposure and c) after exposure to seawater. d) Gold electrodes and d) after exposure to seawater.

Chapter 4

Multifunctional Graphene Sensors

Bending sensors generate an electrical signal based on the bending radius or curvature of the object [152, 165]. Such sensors provide a versatile sensing platform for detecting changes in a variety of physical parameters. They could be manufactured light, inexpensive, and durable, and to withstand vibration, thermal shock, and stretching without electromagnetic interference or sensor occlusions [166]. Medical [167, 168], automotive [169], industrial [170, 171], physical activity assessments [170, 172], and human–machine interactions[172] are only a few of the applications for bending sensors. In the case of passive resistive bending sensors, an electrically conductive patterns or electrodes deposited on a flexible substrate, and change resistance upon substrate bending. These electrodes are commonly developed via carbon-based materials [60, 173] and transition metals[174, 175], which govern the basic electrical properties of the sensor as explained in Chapter 2.1.

The intrinsic piezoresistivity of single-layer graphene is rather limited as the hexagonal mesh of graphene can withstand strains only below ~0.7% with gauge factors (GF) of ~1.4-2 [176-178]. Meanwhile, the responsivity of multilayered structures, such as graphene oxide [179, 180] and hydrogenated graphene oxide is significantly higher[176, 181]. The high variation of the electrical resistance of multilayer samples under strain was explained by the displacement of the layers and changing their overlapping area, which provides the ability to use these structures for force and strain sensors[181].

In this chapter, piezoresistance of graphene electrodes printed on flexible polyimide (PI) films is exploited. The LSG sensors are used for the detection of curvature, force, deflection, and flow. The sensor was customized for different applications simply by adopting the geometry, while achieving a homogeneous bidirectional response, temperature compensation, and high accuracy[152].

4.1 Methods and Operation Principle

The printed electrode pattern was structured in a meander shape to maximize the area of LSG, as shown in Figure 4.1a. The line segments are connected in series, such that resistance variations in each segment can contribute accumulatively to provide a large change in resistance, while keeping the minimum electrode width. The bending sensor utilizes porous LSG on a flexible PI film to transduce a signal via cantilever deflection, i.e., it is supported at one end with the other end free, as illustrated in Figure 4.1b. An external force, F, applied to the tip of the cantilever induces a uniaxial stress [182, 183],

$$\sigma = \frac{F(L-d)c}{I_A}, \tag{4.1}$$

where L is the cantilever length, c is the distance to the neutral axis, d is the distance from the anchor, and I_A is the area moment of inertia. The tensile stress occurs at the top of the cantilever, and compressive stress acts at its bottom. These longitudinal stresses vary linearly across the cantilever thickness and along its length. The maximum pressure, σ_{max}, originates at the surface of the cantilever at the anchor point, as seen in Figure 3.8b. The

sensor exposure to the external force, such as water flow, along the y axis, leads to a cantilever bending and fractional resistance change that can be described by [182-185]

$$\frac{\Delta R}{R} = \pi_l \sigma_{max} = \frac{6\pi_l (L - L_{pr}/2)}{wt^2} F, \tag{4.2}$$

where π_l is the piezoresistive coefficient, L_{pr} is the length of the piezoresistor, t and w are the thickness and width of the cantilever, respectively. Thus, the sensitivity of the transducer could be tailored by the length, cross-section area of the sensor substrate, and the length of the piezoresistor.

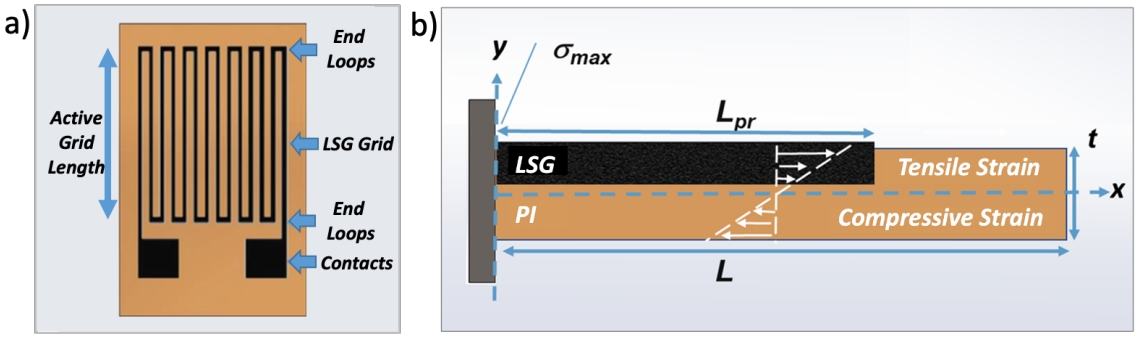

Figure 4.1 - a) LSG electrodes patterned on flexible PI sheet b) The schematic of a cross-section of a piezoresistive cantilever beam.

4.2 Characterization of LSG Bending Sensor

A typical factor used to characterize strain sensors is the Gauge factor (GF),

$$GF = \frac{dR/R}{dl/l} = \frac{d\rho/\rho}{\varepsilon} + 1 + 2\upsilon \tag{4.3}$$

where $\Delta l/l$ is the strain, R is the resistance under zero strain, ρ is the electrical resistivity, v is the Poisson ratio (v_{Kapton} = 0.34) [72]. An LSG electrode in the form of a strip with a length of 30 mm, a width of 2 mm, and initial resistance of ~0.7 kΩ was used to evaluate the GF. Both ends of the strip were fixed by sample holders (inset of Figure 4.2) of an

electromechanical pull tester (5900-Series, Instron Inc.), which provided a continuously increasing force and measurement of the resulting displacement. A continuous current of 1 mA was applied through the graphene strain sensor (as in all consecutive experiments) to measure the change of electrical resistance during the tensile deformation of the sensor with a Keithley 2400 Source Meter. Figure 4.2 reveals a linear relationship between strain and relative change in resistance. The increase in resistance is attributed to a narrow and long conductive porous structure. The $GF \simeq 11.2$ (Young modulus $\simeq 2.1$ GPa, yield strength $\simeq 83$ MPa) is extracted from the slope, and is in the range of the values of metal strain gauges. The intrinsic contribution to the piezoresistivity was found to have ($(d\rho/\rho)/dl/l = 0.84$) a positive sign, suggesting a positive piezoresistivity.

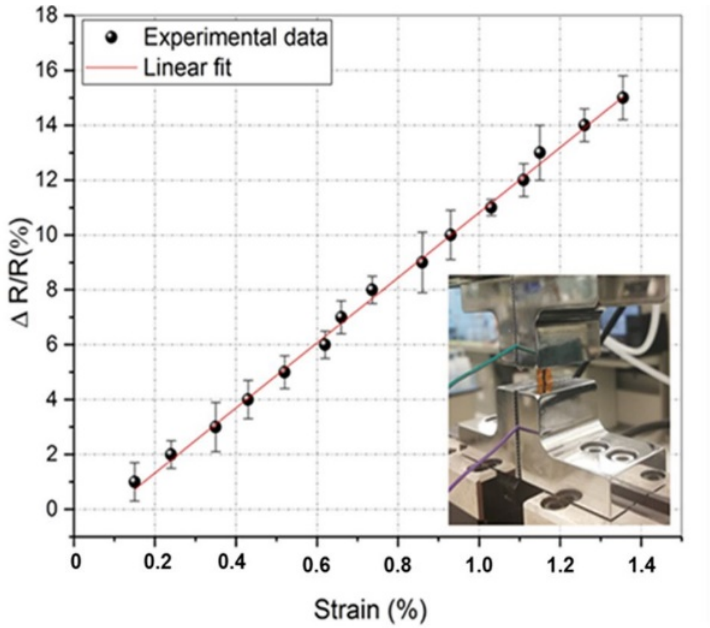

Figure 4.2 - Strain-induced resistance change of LSG.

4.3 Force, Deflection, and Flow Detection

The electromechanical pull tester was used to induce deflection of the LSG sensor, as shown in the insets of Figure 4.3. The resistance variation of the sensor in tension state (LSG on the convex side) has a linear relationship with the exerted force and the sensor deflection. The electrical resistance of the LSG sensor, shown in Figure 4.3a (width: 7 mm, length: 7.6 mm, number of turns: 11), increases at the rate of ~2.98 Ω/mN and ~0.21 Ω/µm at room temperature. Conversely, the LSG bending sensor shows a decreasing resistance in compression state (LSG on the concave side), reducing at the rate of ~2.91 Ω/mN, ~−0.21 Ω/µm (Figure 4.3b). The absolute change in resistance is tailored by the number of turns of the LSG electrodes as seen in Figure 4.4a. An increased number of turns with the same dimensions did not affect the normalized sensitivity, since the percentage change in resistance for a given strain for the entire LSG path is the same as for any single trace. Using shorter electrodes (7 mm) results in a

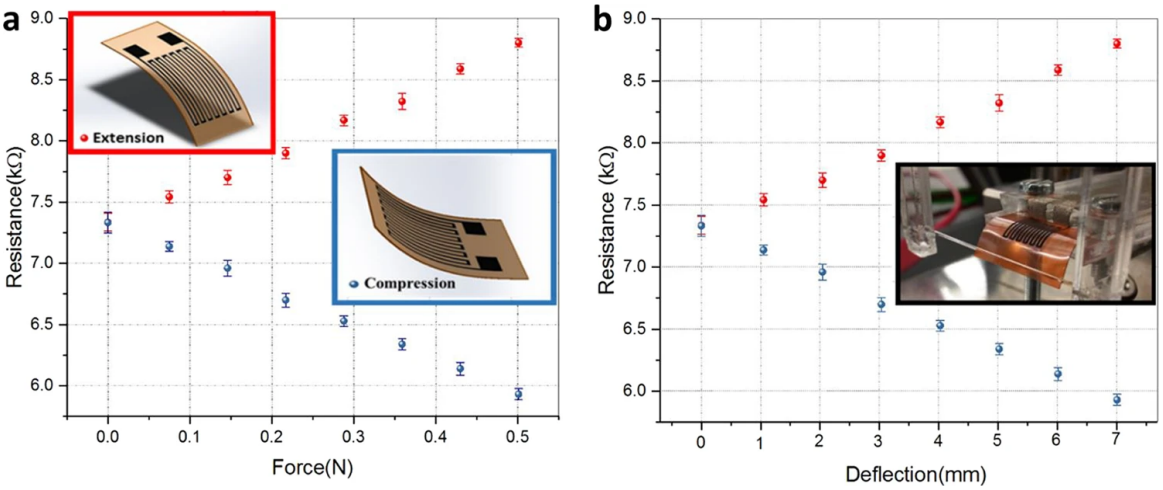

Figure 4.3 - Average resistance as a function of a force and b deflection induced during extension and compression of LSG. The error bars indicate the standard deviation. The coefficient of determination (R2) is 0.9961 during extension and 0.9984 during compression.

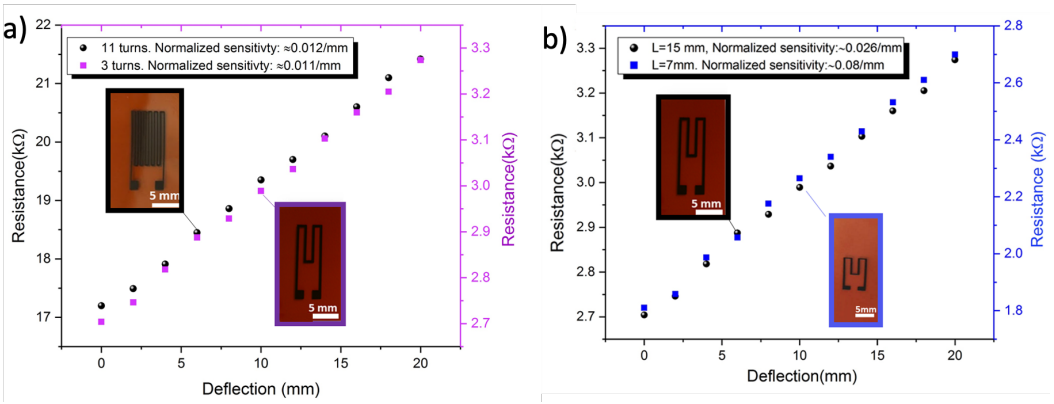

Figure 4.4 - a) Responses of LSG sensor for an increased number of turns with the same dimensions. b) Responses of LSG sensor for varying lengths with the same number of turns.

higher sensitivity than longer ones (15 mm) with the same number of turns (Figure 4.4b), as expected from Equation 4.3.

To test the response of a LSG bending sensor to different flow rates, a setup was constructed wherein a fluid flowing inside a tube bent the sensor toward the direction of fluid flow, as can be seen from Figure 4.5. The bulk flow of the fluid is quantized by the bending moment exerted on the bend sensor that is caused by the drag associated with the flowing fluid [169]. Two segments of opaque polyvinylchloride (PVC, 0.73 m length) and transparent acrylic (0.29 m) with the same internal diameter of 36 mm were used to make the flow tube for sensor testing. For flow rate management during testing, a ball valve was fitted on one end of the PVC pipe, which was connected to a submerged pump (DC Runner 2.1, Aqua Medic) in a seawater basin through a flexible hose. The ultrasonic flow meter (Siemens Sitrans, FUP 1010) was mounted on the PVC part of the flow tube to measure water flow rates to the test sensor, which was vertically fastened and adhesive-sealed through a slit in the acrylic tube. Since the acrylic tube was transparent, it allowed

for a clear view of the sensor bending at different flow speeds during testing. As a result, the flow experiments were carried out at speeds of up to 3 m/s to reduce the effects of turbulent flows. Figures 4.6 a and b demonstrate the bending sensor's outputs when the water flow causes tension and compression in the LSG electrodes, respectively. Within a speed range of 0.5–3 m/s, the sensor response is linear. For the instances of LSG tension and compression, the sensitivities determined for the flow sensor are 100/(m/s) and 110/(m/s), respectively.

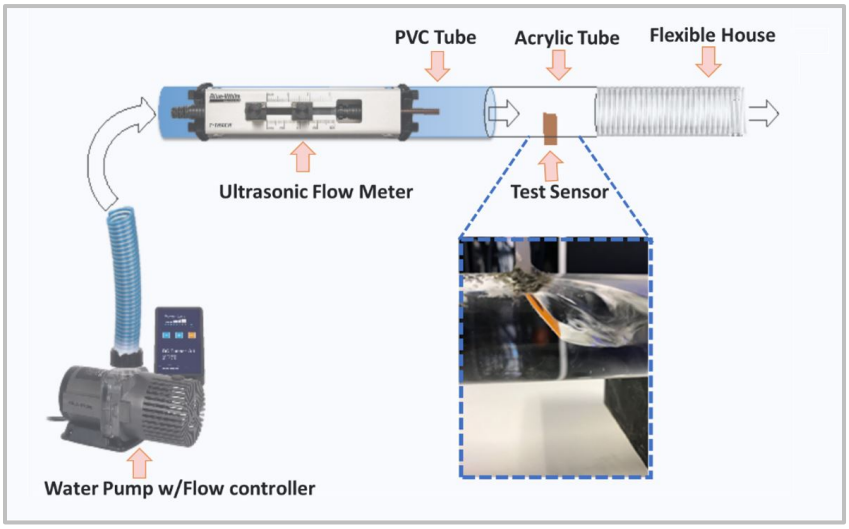

Figure 4.5 - Schematic of the flow test setup. The inset shows the bending the LSG sensor toward the direction of fluid flow.

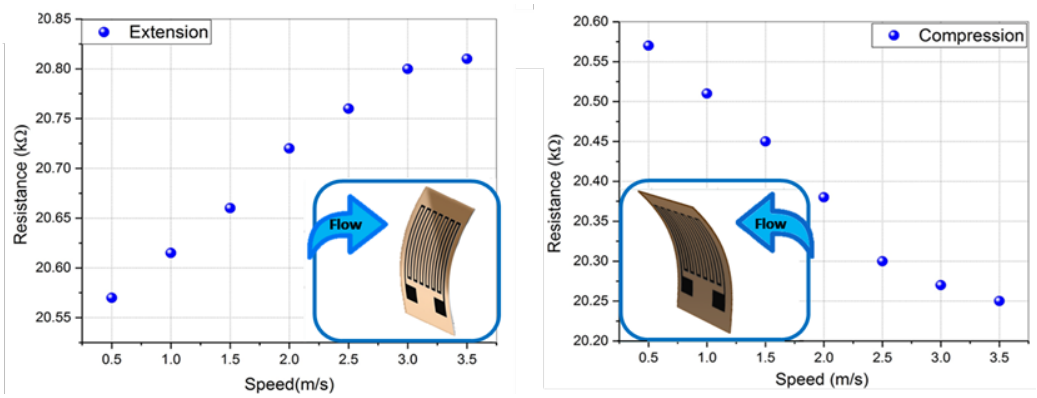

Figure 4.6 - The response of the bending sensor to different flow velocities, when the LSG electrode is a) extended and b) compressed.

4.4 Double Sided LSG Sensor

The bending sensor concept in combination with the simple fabrication process, allow fabricating a double-sided LSG sensor, where the LSG electrodes are patterned on both sides of the PI film, as illustrated in Figure 4.7. By utilizing a difference measurement, where the output signals of the sensor under compression and tension are subtracted, several advantages arise. First, an equal directional response is obtained for both bending directions, since compressive and tensile responses are added up. Second, the output voltage is zero under zero-load condition, allowing for higher signal amplification. Third, a rejection of common input signals is achieved. An example for the latter is the effect of temperature, which is removed by using the double-sided LSG sensor.

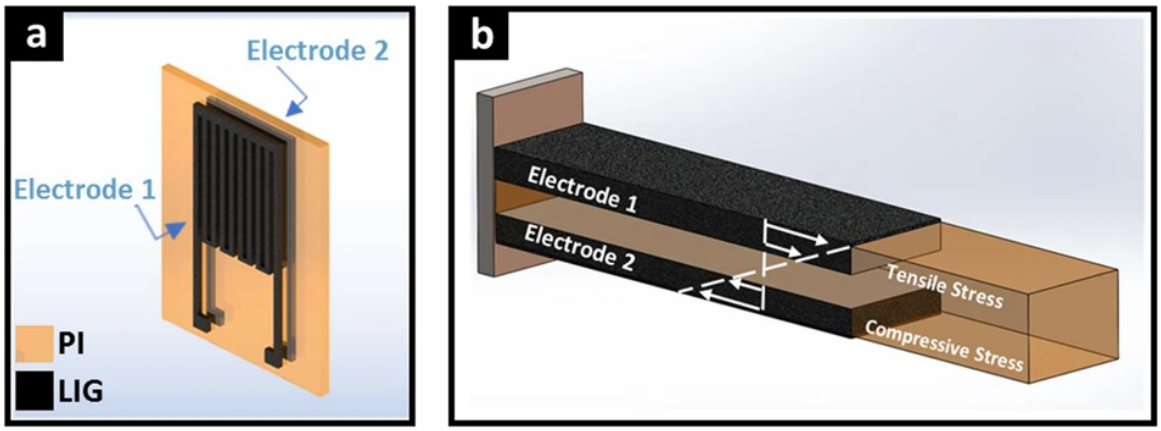

Figure 4.7 – a) Schematics of a double-sided LSG bending sensor and b) its cross-section with the stress, due to bending.

As previously reported, the resistance of LSG electrodes decreases by 4% over a temperature range of 20–60 °C [186]. By measuring the resistance change of both sensor electrodes of the LSG sensor (Figure 4.8a) and subtracting them from each other (Figure

4.8b), the electrode deflection and applied force can be determined, with the same sensitivity in both bending directions.

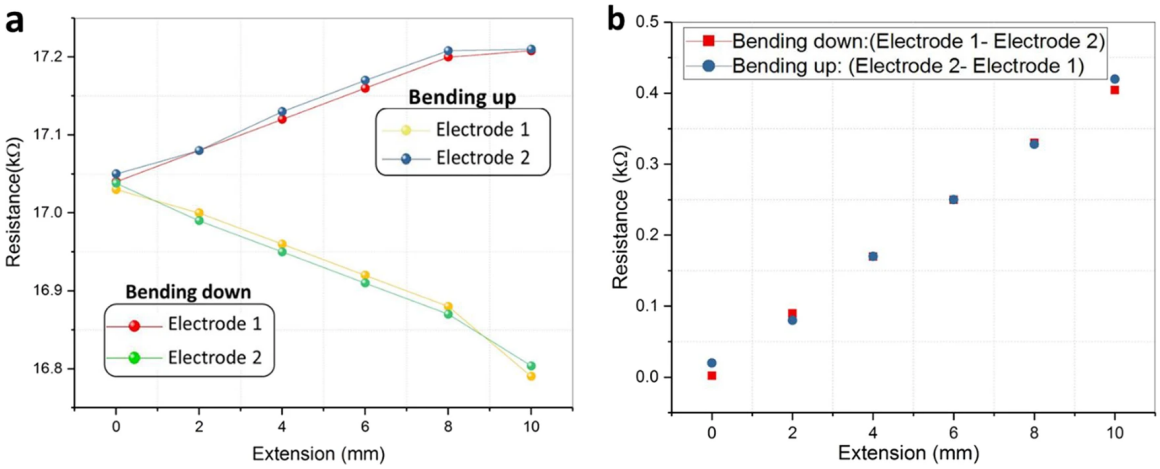

Figure 4.8 - a) The responses of a double-sided LSG sensor to bending with the LSG under tension and compression states. b) The results of difference measurements.

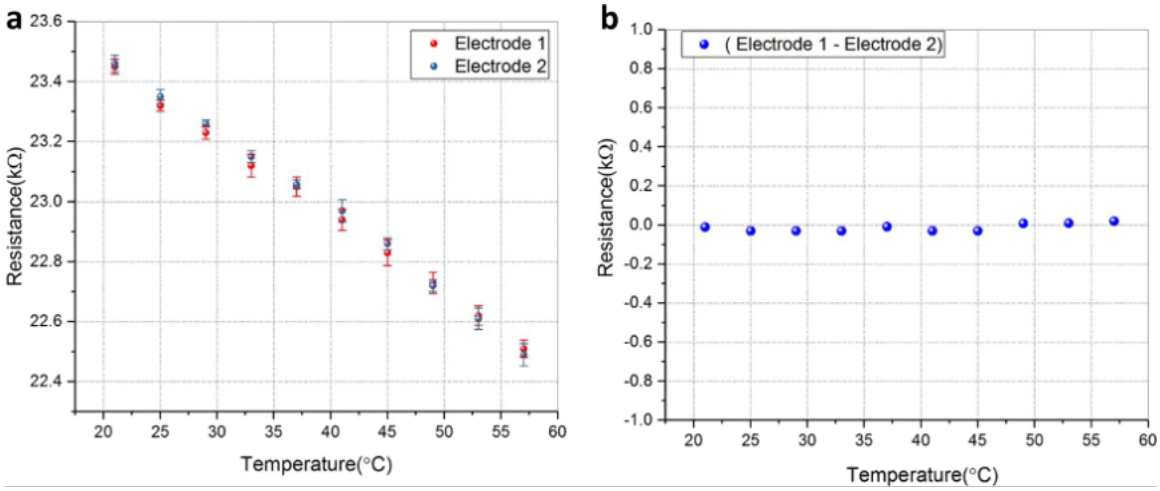

Figure 4. 9 - a) The resistance of the LSG sensor as a function of temperature. Each data point represents the average of three measurements; error bar connects the maximum and the minimum values. b) The result of subtracting the average output signals of electrodes from each other.

Since both LSG electrodes are affected by the same temperature (Figure 4.9a), signal subtraction results in a complete compensation of the temperature effect (Figure 4.9b).

This is possible, due to the close proximity of the printed electrodes (~50 µm) and high thermal conductivity of PI (0.46 $Wm^{-1} K^{-1}$).

4.5 Marine Animals Monitoring

Speed sensing of underwater animals is particularly difficult, due to the extrmem conditions in the Red Sea combined with the requirement for low weight, size, and power consumption. Speed sensing is essential for quantifying marine species' energy expenditure, which is important for understanding their feeding patterns, biogeography, life history, and various conservation activities. [187]. Through the use of bending sensors attached to animals, it may be possible to assess animal body velocity over time in order to determine energy expenditure [188]. In most cases, speed is measured by the overall dynamic body acceleration, in which a derivative of the acceleration represents the metabolic rate [188]. T As an indirect approach, this approach cannot estimate the energy budget when activities remain stationary and the flow velocity varies over time. Other methods have exploited turbines [189], paddle wheels rotated by ambient water flow[190], and reflectance of infrared light against a flexible paddle[191]. Meanwhile, commercially available flow sensors use various operating principles, such as differential pressure meters [192, 193], variable area flowmeter [193], electro- magnetic [194], vortex, [195], ultrasonic [196] and Coriolis mass [197]. Because of fragile moving parts or high installation and maintenance costs, these solutions offer limited capabilities. A buildup of foreign particles may also cause biofouling and blockage. To overcome some of these issues, additional protective housings have been employed, which increase the

device's size, buoyancy, and weight, which has been shown to influence animal behavior and swimming ability [171]. Research is also being conducted on the use of flexible, noninvasive, lightweight, low-powered, cost-effective, and flexible sensors for continuous tracking of body segments over extended periods of time and without reducing freedom of movement. The LSG bending sensors are beneficial for monitoring human movement over a long time in kinesiology, physiotherapy, rehabilitation, telehealth, or even controlling prosthetic limbs. The LSG bending sensors proves a powerful tool, when coupled with aquatic tags, such as Aquamote [198] and Daily diary [199], to allow reconstruction of fine-scale behavior. Animal monitoring experiments were carried out at the Oceanographic Foundation Research Center in Valencia on a Bottlenose dolphin (the genus Tursiops) and a Loggerhead sea turtle (Caretta caretta). To this end, an LSG sensor of 17.2 kΩ resistance, shown in Figure 4.10 (width: 7 mm, length: 15 mm, number of turns: 11), was integrated with a commercial tag (ICM-20948, TDK InvenSense), which was attached to the dolphin’s spine noninvasively by a vacuum sucker (inset of Figure 4.10), and the turtle’s carapace by a waterproof velcro (VLC02, Velcro® Brand Marine Grade Hook and Loop) and pure epoxy compound (Subcoat S, Veneziani Yachting) (Figure 4.11a).

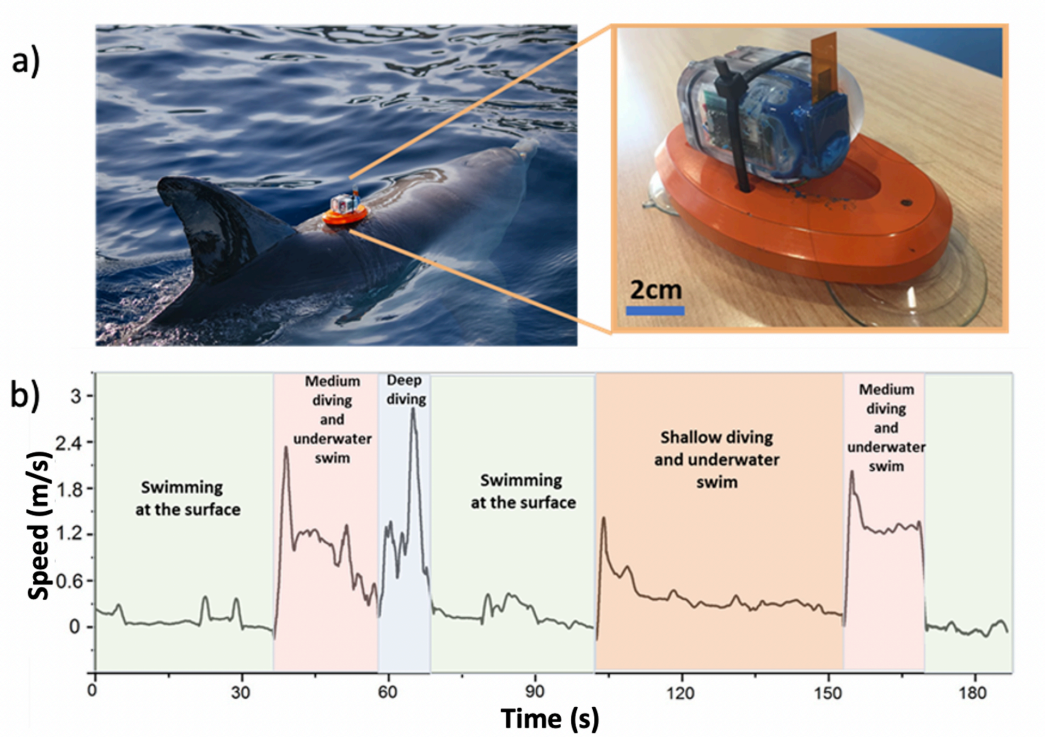

Figure 4.10 - a) LSG bending sensor integrated with ultra-low power Aquamote tag and attached to a dolphin's spine. b) The resistance of the LSG sensor and corresponding swim speed of the dolphin as a function of time for a duration of 3 min.

The resistance of the LSG tag was recorded during a dolphin's training session and translated to swimming speeds via a calibration obtained from Figure 4.6. Different maneuvers, such as shallow-, medium-, and deep diving and swimming (Figure 4.10b) were carried out by the dolphin in 3 min, and were clearly reflected in the sensor response, with a maximum speed of ~2.7 m/s reached during deep diving and an average speed of ~0.8 m/s, ~1.3 m/s, ~2 m/s, and ~0.4 m/s for shallow-, medium-, and deep diving and swimming, respectively. The overall average and median speeds of the Bottlenose dolphin were ~0.32 m/s and ~0.3 m/s, respectively. The speed recorded when the dolphin was swimming at the surface of the water is likely inaccurate, due to submerging of the sensor. A different sensor position could help remedying this problem.

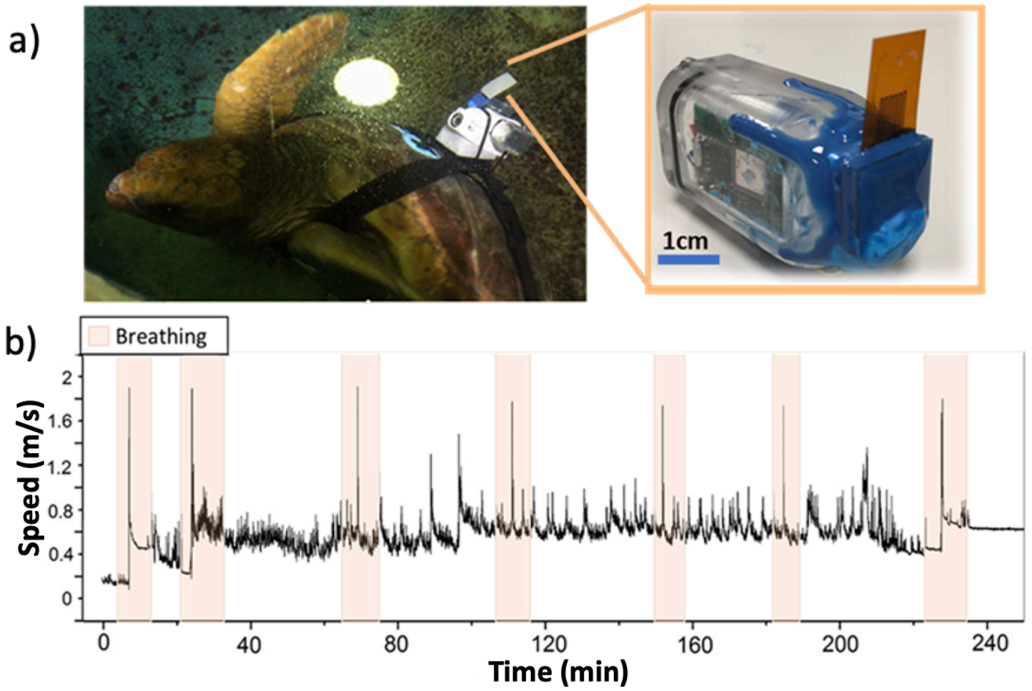

Figure 4.11 - a) LSG bending sensor integrated with commercial tag and attached to the sea turtle. b) The recorded speed of sea turtle as a function of time for a duration of 4h.

The measurements of the sea turtle's speed required a more sensitive speed sensor than the one used for the dolphin, due to the slower motion of the turtle. As described above, the sensitivity can be easily tailored by increasing the cantilever length or area. Therefore, the sensor design was modified to increase its area by the addition of a 2×2 cm^2 patch. The sea turtle reached the maximum speed of ~1.82 m/s, when swimming to the surface to breath, which happened seven times during the recorded ~4h, as seen in Figure 11b. The average and median speeds of the turtle were ~0.51 m/s and ~0.53 m/s, respectively. The turtle was constantly in motion with the lowest speed reaching ~0.1 m/s.

4.6 Flow Velocity Monitoring

Another LSG bending sensor (width: 7 mm length: 15 mm, number of turns: 3) was combined with a Daily Diary tag (TDR10-DD, Wildlife computers), which had a size of 20 × 20 mm^2 (Figure 4.12a), to measure the flow velocity of the underwater currents at the Al Fahal coral reef in the Cental Red Sea (geographic coordinates: 22.25285 °N, 38.96123 °E, average salinity:~35%, average temperature ~33 °C) (Figure 4.12b). The result of a flow measurement over ~1 h (Figure 4.12c) reveals that surface current flow had average and median speeds of ~0.47 m/s and ~0.48 m/s, respectively, with an occasional increase to a maximum speed of ~0.92 m/s. The minimum speed was ~0.21 m/s.

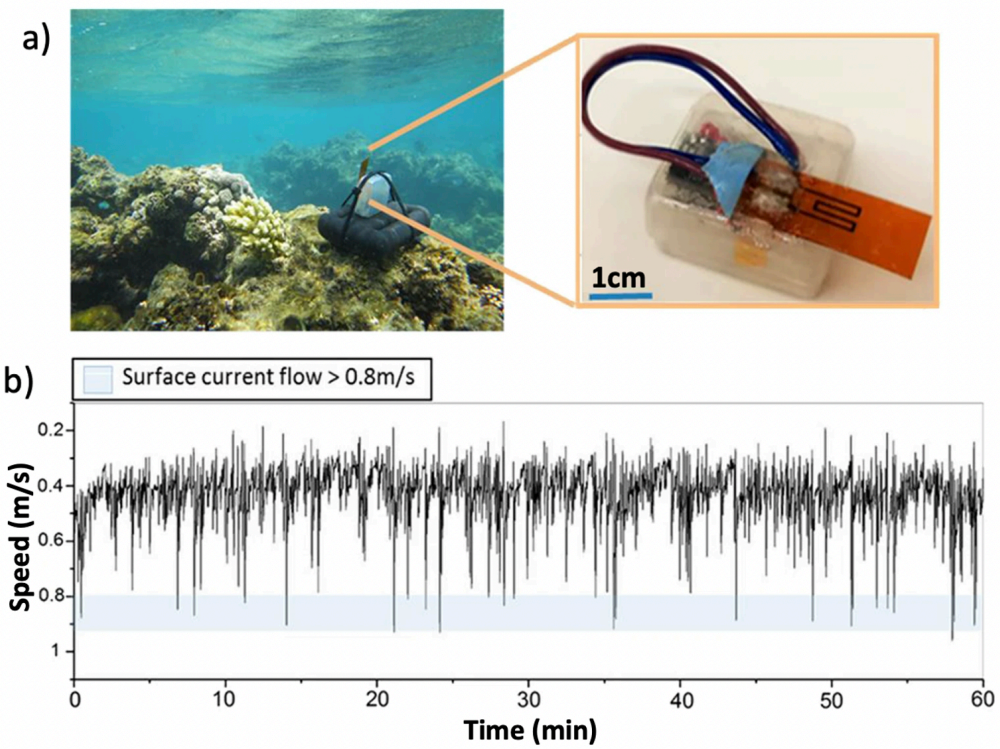

Figure 4.12 - a) Tag deployment in Al Fahal Reef of Red sea to measure flow velocity. Inset shows the LSG bending sensor integrated with a Daily Diary tag (scale bar: 1 cm). b) Recorded resistance as a function of time for a duration of 1hour.

4.7 Wearable Device

The schematic illustration of LSG bending sensors attached to various body locations for associated detection of joint-bending related motions, such as fingers, elbows, knees, ankle and neck is shown in Figure 4.13a. LSG sensors of various geometry were directly and non-invasively mounted using 0.1g of biocompatible petroleum jelly (Vaseline Products). The responses of the index finger bending forward and backward

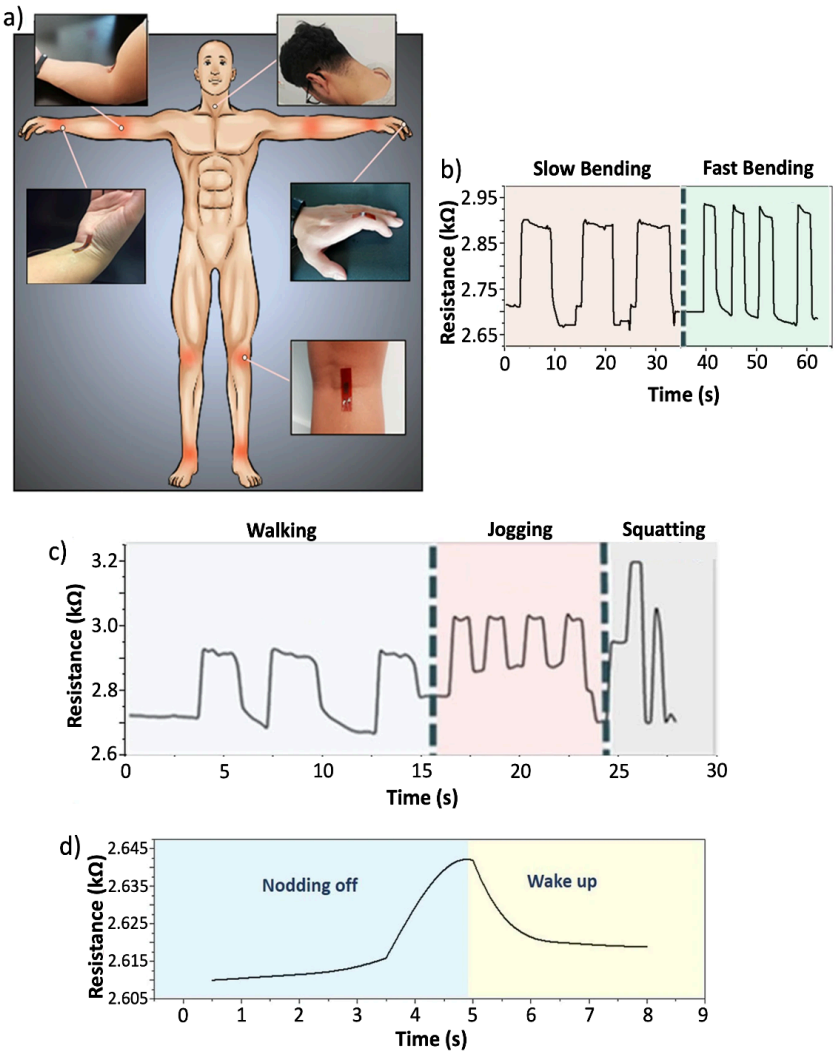

Figure 4.13 - a) Schematic of wearable LSG bending sensors attached to different positions of a human body to monitor joint-bending-related motions. b) Monitoring the response of finger bending c) Knee-related motion monitoring: walking, jogging, and squatting.

consecutively with various speeds (~0.1 bends /min and ~0.25 bends/min) are shown Figure 4.13b. Meanwhile, Figure 4.13c displays knee related motions which discriminate walking, jogging, and squatting according to their distinctly differentiated waveforms. The combinations of two or more LSG sensors would allow the measurement of multiple DOFs, such as torso, shoulder and ankle. A hypnagogic jerk (sleep start or hypnic jerk) is a brief contraction of the body that occurs involuntarily, when a person is beginning to fall asleep, which often causes the person to jump and awake suddenly. The associated movement of the head results in neck bending, which can be monitored for assessing drivers vigilance [200, 201]. This head movement was measured by means of an LSG bending sensor attached to the neck, as seen in Figure 4.13d.

4.8 Summary

The remarkable material qualities of LSG opened up new possibilities for a versatile, long-lasting printed bending sensor that can detect flow, deflection, or force in a variety of situations and on a variety of subjects. The flexibility in geometry and a simple fabrication process allow simple tuning of the bending sensor to achieve different sensitivities or dynamic ranges. Using tensile stress/strain measurements a Young modulus of 2.1 GPa and Yield Strength of 83 MPa were found for the sensor with LSG printed on 125 µm thick Kapton tapes. The GF of LSG is 11.2 with a piezoresistive coefficient of ~0.84. The sensor has a very large range with maximum strains reaching 1.4%. The LSG showed a linear response to compressive and tensile bending in cantilever

deflection and point load bending tests.. A double-sided electrode concept was developed by printing on both sides of the Kapton. In combination with a difference measurement an increased and homogeneous bidirectional response was obtained with full temperature compensation. The sensor can also survive harsh environment conditions over an extended period of time.

The proposed LSG sensors were used in a variety of applications to illustrate its versatility, including monitoring the speed of marine animals, measuring current flow velocity in a coral reef, and recording human joint bending and motion. Thereby, the LSG sensors feature light weight and minimal intrusiveness, accommodating the requirements to monitor animals with very different velocities and behaviors. Attached to the human body, the wearable sensors operated at large bending ranges, showing a great potential for personal healthcare monitoring, intelligent prostheses and human-machine interactions.

Chapter 5

Enhanced Sensing Performance

Although the sensitivity and dynamic range of LSG strain sensors could be tuned via the sensor geometry, the overall resistance variation was limited to a maximum of 10% and a gauge factor of ~ 11 [24]. More accurate and sensitive detection of deflection, force, and curvature would be possible with a higher change in the value of resistance for a small change in strain, which is critical in many automotive, industrial, and medical applications. Increasing the laser power within a given range has previously improved the electromechanical performance of LSG [118, 119], or by transferring the LSG pattern to an elastomeric substrate, such as PDMS[117], silicon rubber [202] or polystyrene [203]. The former frequently results in graphene separation from the substrate or thermal damage, which causes rapid performance decline and inaccurate measurements. Multi-step fabrication procedures are used in the latter, which is neither efficient nor cost-effective when generating high-volume end products. Furthermore, compared to fully automated technologies, the effort necessary in moving LSG to different substrates slows down the production process.

The multifunctional LSG strain sensor introduced in this chapter has widely tunable properties and greatly improved electromechanical performance. An extendable, plug-and-play sensor module was designed to readily integrate the LSG sensor into numerous applications, and it was used in velocity profile monitoring of Unmanned Aerial Vehicles (UAV) [204].

5.1 Methods and Operation Principle

The fabrication process of the LSG bending sensor follows the procedures described in Chapter 3.3. It also reported that samples with three iterations of repeated laser writing resulted in an increase of porosity and reduced intrinsic structural defects. The following experiments in this chapter were carried out with the LSG sensor realized using three times laser writing. The versatile fabrication process also allowed fabricating a double-sided LSG electrode with optimized geometry and size, as shown in Figure 5.1. Both electrodes were short in length (l = 5 mm) and structured in a meander shape (number of turns = 9) to achieve a large variation in resistance with the smallest electrode width. The working mechanism of the LSG strain sensor has been described in Chapter 4.1

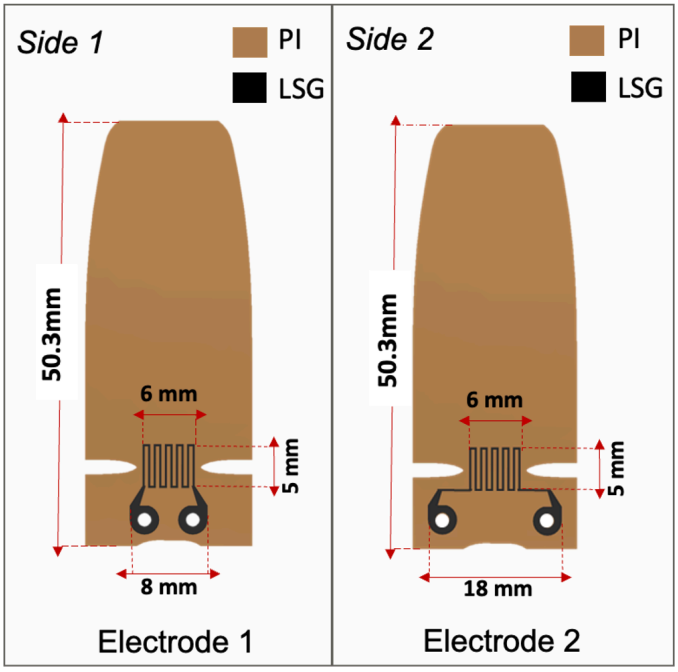

Figure 5.1 - Design of double-sided LSG bending sensor for repeated laser writing;

5.2 Electromechanical Performance

The effect of multiple lasers writing on the electromechanical parameters of the LSG has been evaluated by scribing the LSG sensor in the shape of a strip with a length of 20 mm while maintaining the same lasing power and speed as reported in Chapter 3.1. The width and thickness of LSG increased by 12% and 33%, respectively, after three laser writing times (Table 3.1). This increase in cross-section area could mean less electrical resistance for the same piece of LSG. However, the increased resistance and resistivity observed after each lasing step suggests the dominance of the effect of increased porosity [154, 155]. To measure GF, the LSG strip was firmly positioned in the sample holder of an electromechanical tensile testing machine (5900-Series, Instron.) to apply strain (inset of Figure 5.2a). A DC current of 1 mA was applied to the LSG strain gauge to detect the variation of the electrical resistance during the tensile test via Keithley 2400 sourcemeter controlled with LabView software in a two probe setup. Figure 5.2 shows a linear relationship between strain and relative change in resistance for all LSG samples, which is attributed to a narrowed and elongated conductive porous structure. The highest GF ≃91.2 (Young modulus ≃ 2.2 GPa, Yield Strength ≃80 MPa), shown in Figure 5.2b, was achieved with LSG scribed by using three times laser writing, which is an increase of 750% to one-time laser writing and 720% higher than the ones previously reported for LSG strain sensors. The increased GF is attributed to more polyporous and looser surface morphologies that provide for more displacement and the overlapping area of the graphene layers. A positive piezoresistivity was determined by an intrinsic contribution to the piezoresistivity ($(d\rho/\rho)/dl/l = 89.52$);

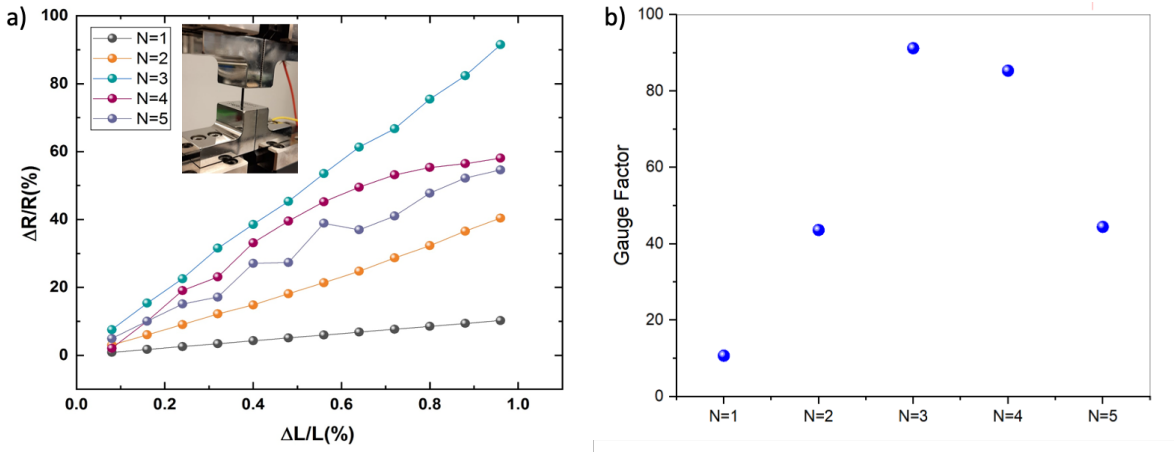

Figure 5.2 - a) The induced strain as a function of resistance change of LSG at different laser stages. b) Gauge factor dependence on a number of laser scribing

5.3 Enhanced Force, Deflection, and Airflow Detection

The electromechanical tensile testing machine was also utilized to provide deflection in both bending directions, as shown in the insets of Figure 5.3a. As expected, the resistance changes linearly with external force and deflection during sensor extension (LSG on the convex side). The electrical resistance of the LSG sensor scribed three times rises at the rate of 557 Ω/mN and 358 Ω/mm in ambient conditions (Figure 5.3a). Meanwhile, the LSG bending sensor exhibits reducing resistance during compression (LSG on the concave side), decreasing at the rate of -554 Ω/mN, -356 Ω/mm. In comparison to the sensor that is laser scribed once (38 Ω/mN, 24 Ω/mm), the sensor that was laser scribed three times showed ~15 times higher sensitivities in both directions.

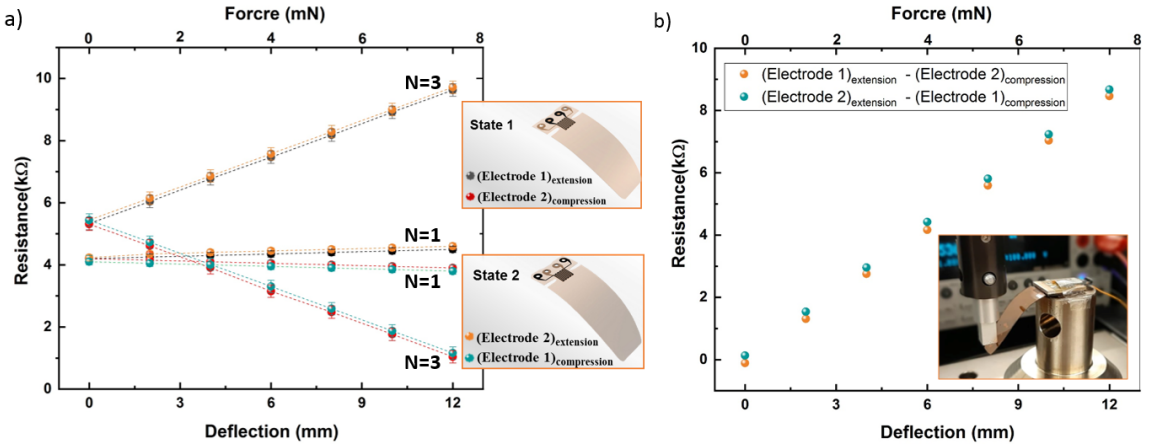

Figure 5.3 a) The responses of one time (N=1) and three times laser scribed (N=3), double-sided LSG sensors to bending under extension and compression states. b) The resultant difference measurements of three times laser scribed sensors.

The double-sided sensor configuration further increased sensor sensitivity, providing 1108 Ω/mN and 712 Ω/mm with zero output voltage under no-load condition (Figure 5.3b), as well as a rejection of common input signals, such as temperature. To examine the output of a LSG bending sensor to various airflow speeds, a setup was built wherein an air streaming in the tube induced sensor bending towards the direction of airflow (Figure 5.4a). The airflow was quantified by bending induced from the drag associated with the airflow. The flow tube was constructed from obscure PVC with a length of 0.25 m and a diameter of 50 mm. An adjustable-speed electric fan with a brushless DC motor (KV 2600, Dynam RC Planes) was used for the regulation of the flow up to 12 m/s. The motor was connected to an electronic speed control driven by signals from the microcontroller (Atmega328, Microchip Inc.) and powered by a Switch Mode Power Supply (S1000-12, Festnight Inc.) A forward-curved fan, which is well suitable for the movement of large volumes of air against comparatively low pressures, was fitted into the pipe, as shown in the inset of Figure 5.4a. The bending curvatures of the LSG sensor

induced by various speeds of airflow are shown in the inset of Figure 5.4b. The sensor showed a linear response within the speed range of 2–10 m/s with a sensitivity of 210 Ω/(m/s) for both extension and compression states.

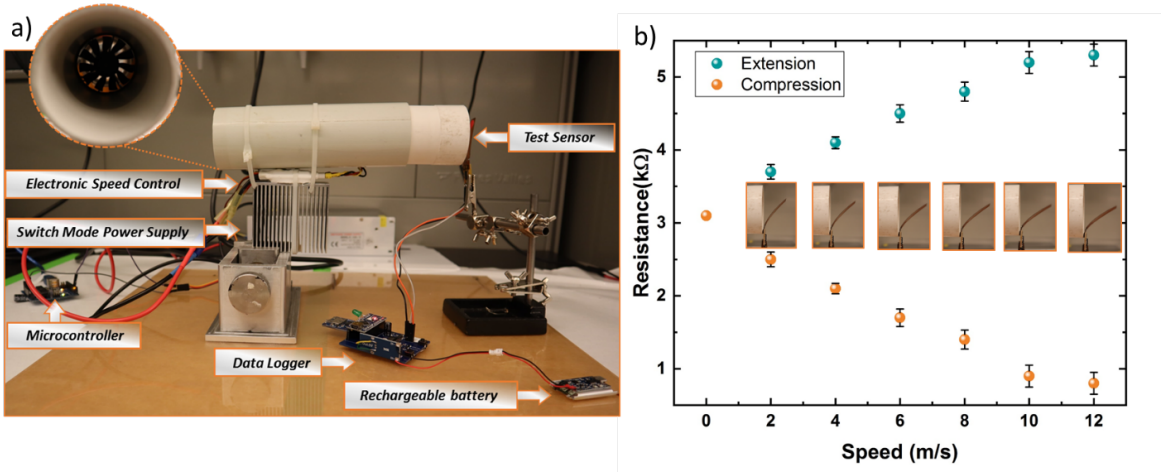

Figure 5.4 - Schematic of the flow test setup. The inset shows the speed-adjustable electric fan; b) Resistance measurements of LSG electrodes scribed on one side of the PI, in extension and compression states.

5.4 UAV Velocity Monitoring

Velocity updates of UAVs greatly enhance the navigation process, as the horizontal velocity is coupled with their roll and pitch angles [205]. The Inertial Measurement Unit (IMU), which is made up of accelerometers, gyroscopes, and magnetometers, is crucial for determining the drone's position and velocity [206]. Typically, the IMU alone provides a reliable state estimation solution, but the error will accumulate over time due to the mathematical integration of signals [207-209]. IMUs constructed with MEMs techniques, in particular, typically contain time-varying bias, cross-coupling errors, and random noise, resulting in error accumulation and signal drifting [210-212]. The global navigation

satellite systems (GNSS), which offer absolute position and velocity updates, have been used to solve this problem[147]. However, the GNSS support is not always available or reliable in confined areas, such as cities, forests, urban and indoor environments[213]. To obtain a long-term accurate navigation solution, at least one type of absolute update is required. Therefore, various navigation assistance methods were attempted based on technologies such as cameras, Light Detection and Ranging (LIDAR) [214], and Radio Detection and Ranging (RADAR) [215]. These techniques suffer from either being unable to operate in dark and featureless areas, high price, heavyweight, high power consumption, and high computational power. In this study, we use a LSG bending sensor to provide absolute velocity updates of UAVs in a real-life environment.

As demonstrated in the previous chapter, the LSG bending sensor proved as a valuable instrument when combined with a data logger for easy integration into various applications. In order to monitor the speed and flying direction of an in-house-made UAV/quadcopter drone, LSG electrodes were scribed three consecutive times and combined with ready-to-attach PCB assembly. The representation of the utilized circuit is shown in Figure 5.5a, where an operational amplifier (LMV324A, ON Semiconductor, Inc) was used for signal conditioning of the signal from the LSG sensor. This operational amplifier of this series is particularly designed for low voltage/low power applications. Meanwhile, a schematic of a custom PCB layout was designed on CAD software and illustrated in Figure 5.5b. A Parylene-C coating of ~1 µm in thickness was applied to the surface of the assembly to protect it from adverse environmental impacts, such as rain. As seen in the inset of Figure 5.6a, the scribed circuit board features vias for stable and

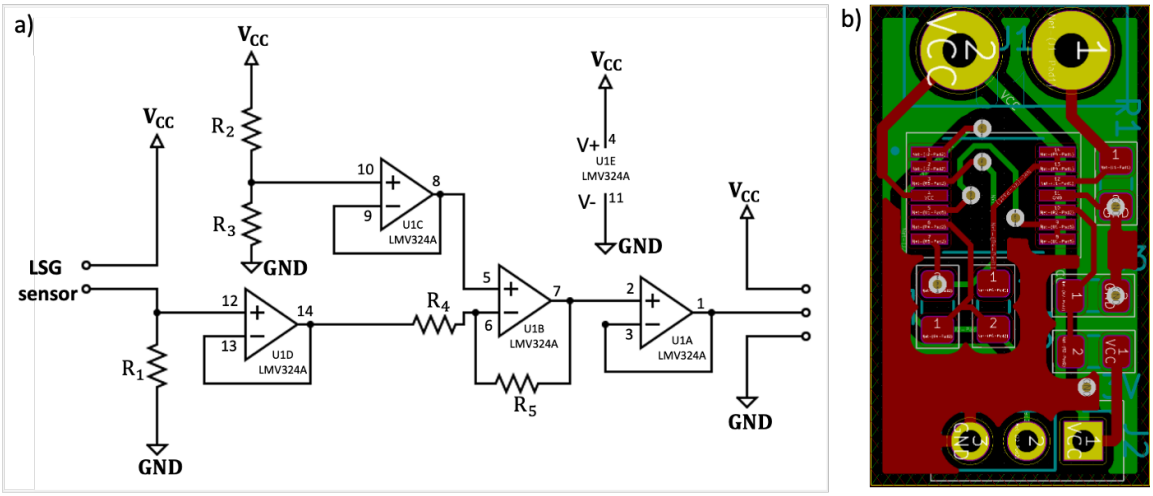

Figure 5. 5 - Block diagram of utilized circuit and corresponding PCB layout.

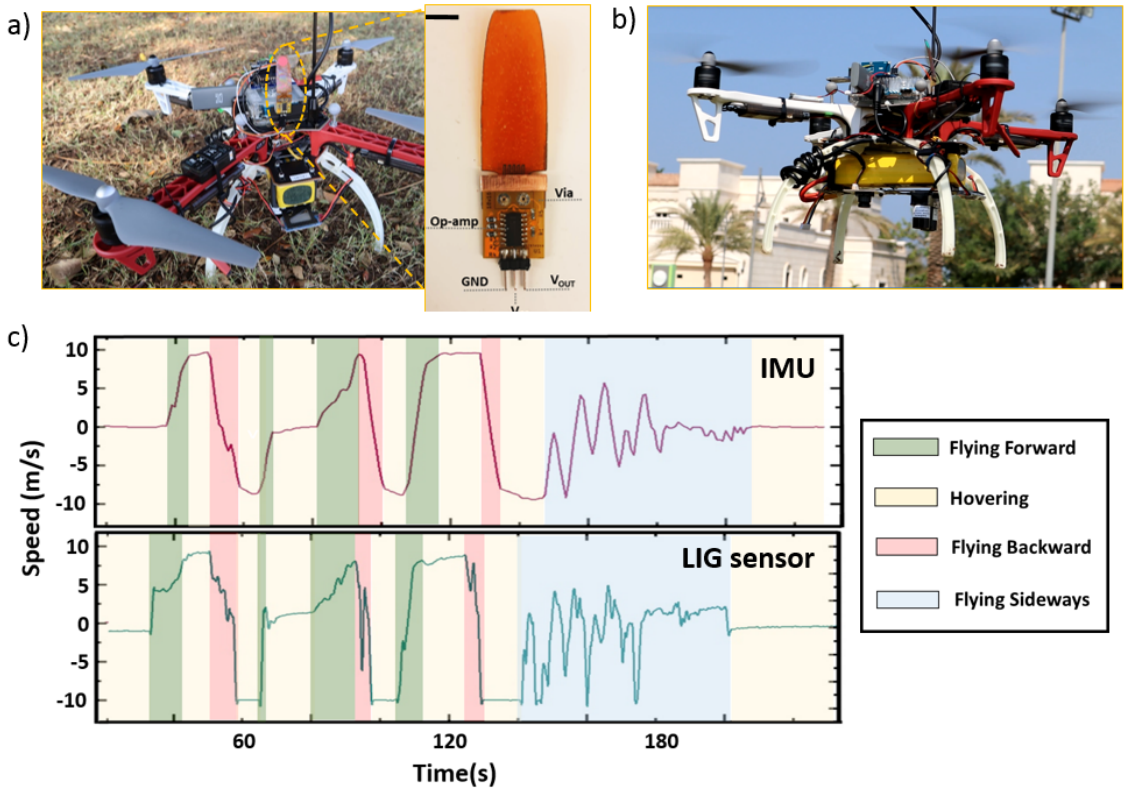

Figure 5.6 - a) LSG bending sensor integrated with PCB (scale bar: 1 cm) and the in-house made drone; b) Sensor deployment in an outdoor environment to measure the velocity of the drone. c) The reference data (top) and LSG sensor data (bottom) corresponding velocity of the drone as a function of time for a duration of time for a duration of 3.5min.

reliable electrical connection to the sensor. Figure 5.6a also shows a photograph of the deployed quadcopter system and LSG sensor module attached to the front side of its frame (F450, DJI) using double-sided mounting tape (FK-M241, Fantastick).

The open-source autopilot firmware was preloaded on the drone flight controller (4Mini, Pixhawk 4 Inc.). A serial connection was used to connect the companion single-board computer (XU4, Odroid Inc.) to the flight controller. A driver for the autopilot with a communication protocol was included in the package installed on the companion computer. For unidirectional, streaming communication, the package released all estimated data into objects known as topics, which could be conveniently retrieved and logged with timestamps. The autopilot firmware generated linear and angular velocities, which were recorded in real time into a file container using the Robot Operating System (ROS) tool. The UAV was controlled by a human in Position Mode during the experiment, which meant that it could actively brake level while being locked to a 3D spatial position. The LSG sensor's signals were acquired during drone flying sessions in an outdoor environment (Figure 5.6b), and the characterization gained from Figure 5.4b was used to calibrate the signals to flying speeds. The drone performed various motions in 3.5 minutes, including flying forward, backward, hovering, and flying sideways. These motions were explicitly reflected in the sensor and IMU responses with the greatest speed of 10 m/s, as shown in Figure 5.6c. Both signals were sampled equidistantly and synchronously to compare the sensor data with the signal produced by the IMU (Figure 5.6c). The correlation and root mean squared error (RMSE) analyses were utilized to make

the comparison. The Pearson coefficient of 0.91 suggests that the two signals have a strong positive association. Meanwhile, the IMU system's integration of the accumulated errors over time, as well as random vibrations of the LSG sensor caused by orthogonal turbulent flows generated by UAV propellers, are ascribed to a substantial root mean squared error (RMSE) of 3.61 m/s. The effect of the latter could be considerably minimized using low-cost wind shielding at two sides of the sensor.

5.5 Summary

Improved LSG sensor qualities could offer up new possibilities for high-performance bending sensors that can measure flow, deflection, or force. To improve the electromechanical performance of LSG, a method of repetitive laser writing was used. LSG with more polyporous and looser surface morphologies produced higher displacement and graphene layer overlapping area. This enabled the study to achieve a maximum GF of 91.2 and a piezoresistive coefficient of 89.5, which is 720 percent greater than previously recorded LSG strain sensors. By scribing the electrodes on both sides of the substrate, the sensitivities to force, deflection and airflow were increased even further. For easy integration into a variety of applications, parylene-C coated LSG sensors were packaged on a ready-to-attach PCB assembly. To this end, a LSG bending sensor was tested on a drone in an outdoor environment and performed very well as a cost-effective solution to provide absolute velocity updates.

Chapter 6

Pressure Sensor

Pressure sensors have been critical elements in many applications across various industries, and many different types of sensors have been developed to satisfy the needs of specific applications. The demand for flexible and lightweight pressure sensors has recently increased, necessitating the invention or use of novel technology. [216-218]. Extensive research has been undertaken to obtain robust pressure sensors for wearable devices [219, 220], human-machine interactions [221], environmental monitoring systems[222], electronic and marine skin applications [223]. In the past few years, pressure sensors based on nanostructured materials, including metal nanowires [224], carbon nanotubes [225], and ZnO nanowire arrays [226] have been explored based on a range of mechanism types such as capacitive, piezoelectric, triboelectric and piezo phototronic.

The large-scale production of such pressure sensor units using non-traditional materials presents challenges. For example, piezoresistive sensors show advantages, such as simple device structure, large measurement range, easy read-out mechanism, and potentially high pixel density [216]. However, the sensitivity of most resistive sensors reduces considerably at higher pressures (>5 kPa), which can be inadequate for certain applications [216]. Maintaining a high sensitivity over a wide pressure range is an important requirement for realizing reliable sensing systems.

Conventional pressures sensors are typically made of rigid materials and cannot conform to non-planar surfaces [218]. In the case of flexible, bendable sensors, it is also important to maintain the pressure sensing ability during deformation on curved and non-planar surfaces. Flexible sensors are relevant in applications for rollable touch displays, biomonitoring, and electronic skins [217]. Despite extensive research and development in the field of pressure sensors, the fabrication process often requires multiple steps, high-vacuum conditions, and time-consuming syntheses.

In this chapter, LSG is used to fabricate piezoresistive, mechanically flexible, lightweight, and robust pressure sensors with a broad measurement range, thereby offering promise across the whole spectrum of demands for pressure sensors. The sensors feature long-term stability, a low detection limit in combination with an extensive dynamic range of at least 20 MPa. This was demonstrated by operating the sensor at a depth of 2000 m in the very saline seawater. The sensor was also used for quantitative measures of tactile sensing and heart rate monitoring with identified distinct peaks associated with blood flow. A number of physical parameters were also systematically deduced from the pressure distribution of plantar pressure during gait analysis[227].

6.1 Methods and Transduction Mechanism

The printed electrode pattern was structured in a meander shape, the same one as described in Chapter 4.1. The layout of the sensor with dimensions is shown in Figure

6.1a. A stable electrical connection and protective coating were obtained via mechanical threading and PMMA, respectively, as described in Chapter 3.1.

The mechanism behind piezoresistive LSG pressure sensors is based on transducing pressure stimuli into a variation of resistance. The overall resistance of the sensor can be approximated as the sum of two components:

$$R \cong R_E + R_{LSG} \cong R_{LSG}, \tag{3.3}$$

where R_E is the resistance of the electrodes, and R_{LSG} is the piezoresistive material. Since the employed copper wires are highly conductive (R_{LSG} >> R_E), the pressure responses mainly result from changes in resistance of the LSG, which is introduced by cross-sectional deformation under external pressure, as shown in Figure 6.1b. The pressure stimulus decreases the distance between neighboring interlayers of graphene, which consequently increases the contact area and reduces the resistance.

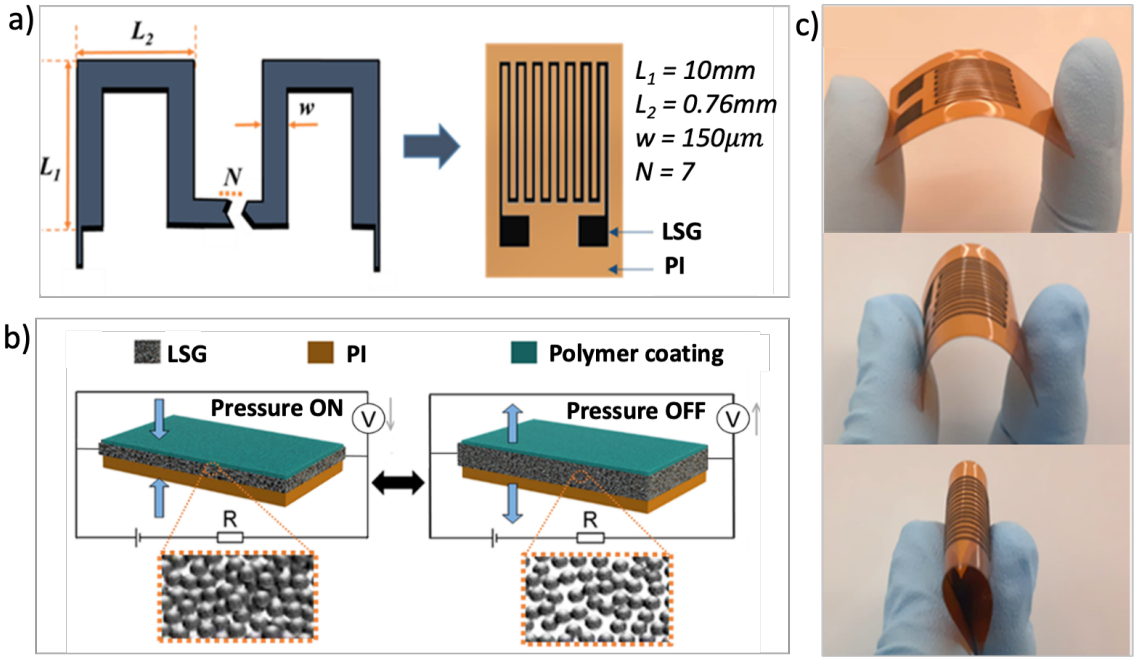

Figure 6.1 - a) Design of LSG pressure sensor. b) Operation principle and c) demonstration of the flexibility of LSG pressure sensors.

In other words, when an external force is applied, more graphene conductive routes are formed, resulting in a reduction in resistance. Because of its low Young modulus, LSG is easily deformed, and when the pressure is released, the porous LSG returns to its original state. The absolute change in resistance is tailored by the number of turns and dimensions of the meander-shaped LSG electrodes. The resulting sensors are also highly flexible, as shown in Figure 6.1c, where an LSG sensor is bent to various radii of curvature.

6.2 Characterization of LSG Pressure Sensors

LSG pressure sensors were examined using static pressures in an electromechanical pull tester (5900-Series, Instron Inc.) by applying a rectangular press load of 1 kN at 1 s intervals. The sensitivity of a piezoresistive pressure sensor is defined as [217]:

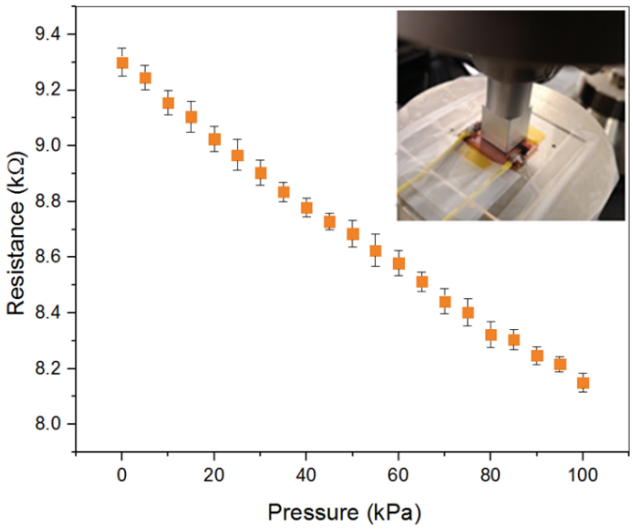

Figure 6.2 - The average resistance of five measurements of a coated LSG pressure sensor as a result of consecutive linear loading cycles in an electromechanical pull tester. The error bars indicate the standard deviation.

$$S = \frac{\Delta R/R}{p},$$

where p indicates the applied normal pressure and $\Delta R/R$ is the relative change in the resistance. A continuous current of 100 µA was applied with a Keithley 2400 Source Meter through the LSG pressure sensor (as in all consecutive experiments) to measure the change of electrical resistance during the compression of the sensor. Figure 6.2 shows the response of the sensor with an average linear sensitivity of 1.23×10^{-3} kPa^{-1} and a standard deviation of $\sigma \pm 0.005$ 10^{-3} kPa^{-1}. The performance of the sensor was then evaluated under a low-pressure regime using the sensor shown in Figure 6.1a. The lowest detectable pressure of 10 Pa resulted in a resistance change of 0.006%, as shown in Figure 6.3a. The response can also be observed in Supplementary Movie 1, where

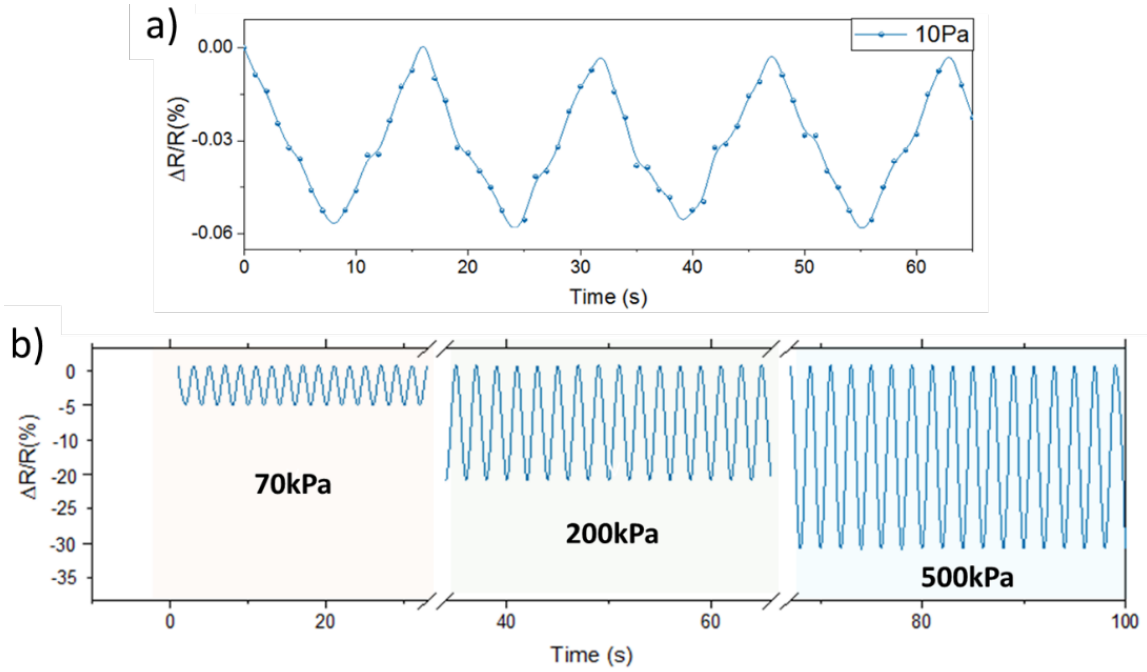

Figure 6.3 - a) LSG sensor responses to low pressure. b) The operational stability of an LSG sensor at different pressures.

the LSG pressure sensor is used to switch on a red LED. Figure 6.3b shows that the sensor repeatedly responds over multiple sinusoidal load cycles with 70 kPa, 200 kPa, and 500

kPa. A 15000-load cycle experiment (>100 hours) is presented in Figure 6.4 and shows no deterioration of the sensor response.

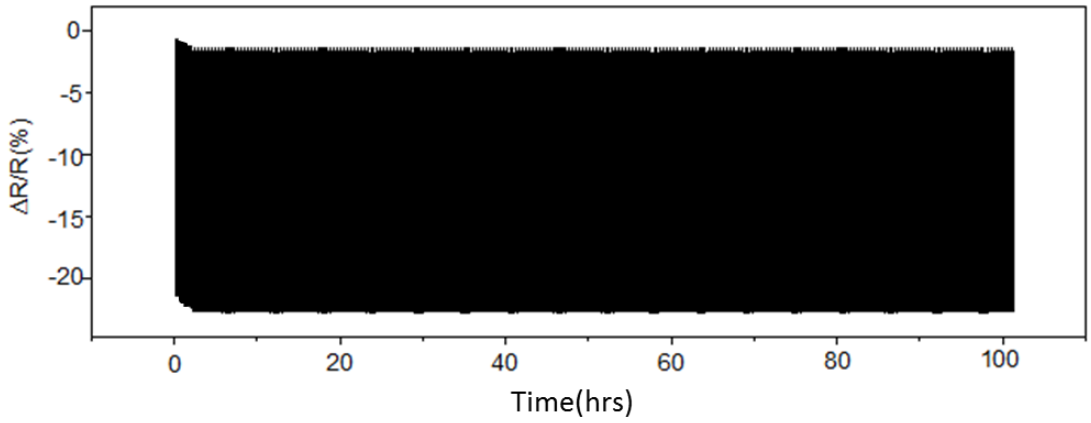

Figure 6.4 - Long-term cycling test applying 2 kN for 15000 cycles.

6.3 Underwater pressure monitoring

To evaluate the sensors for high-pressure underwater applications, they were placed inside of a pressure vessel (3755 PSI, OSECO) using Type T Hydraulic Deadweight Tester (DM-TQ-150-1AL/C, AMETEK), which is the primary calibration standard tool for high-pressure measurements. The sensor was installed within the vessel, connected to the Keithley's Series 2400 SourceMeter with waterproof wires, and the metallic cylinder assembly of 60 cm in height (15 cm diameter) was filled with Red Sea water, as illustrated in Figure 6.5a. Figure 6.5b shows cross-sections of two LSG sensors, which show that despite applying high pressures, there is no discernible change or damage in the structure of the LSG. The response shows a hysteresis error, quantified as the maximum difference between the loading and unloading curve divided by the full-scale output, of 2.9%, which is much lower than the hysteresis observed for conductive foams (Figure 6.6) [217, 228].

The findings indicate that there is no discernible change or degradation in the morphology of the LSG after high pressures are applied, and that the sensor cab be used to a depth of at least 2 km in the seawater.

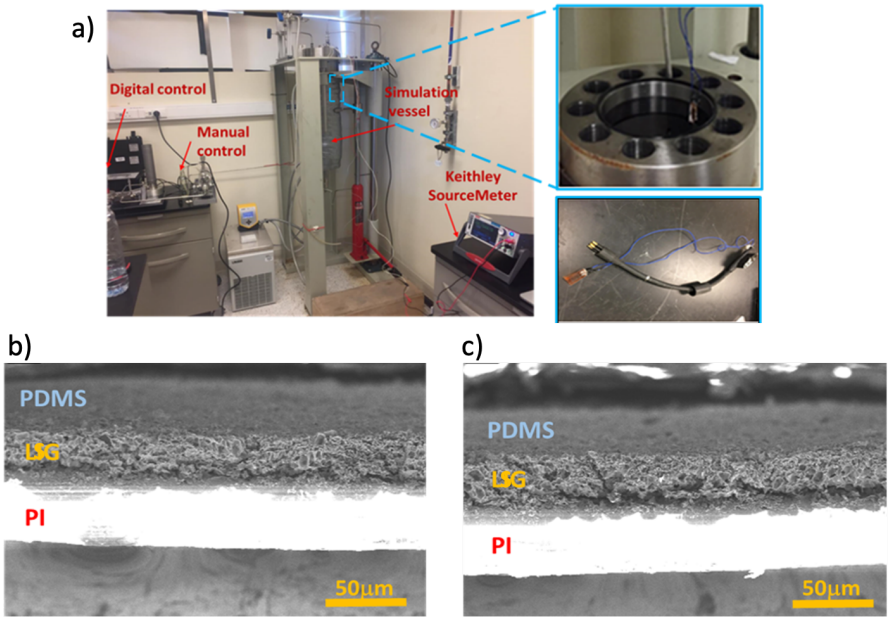

Figure 6.5 - a) Experimental setup for the high-pressure simulation and real-time testing in the harsh seawater environment. b) Cross-section of the LSG) before and c) after exposing it to high pressures of 20 MPa.

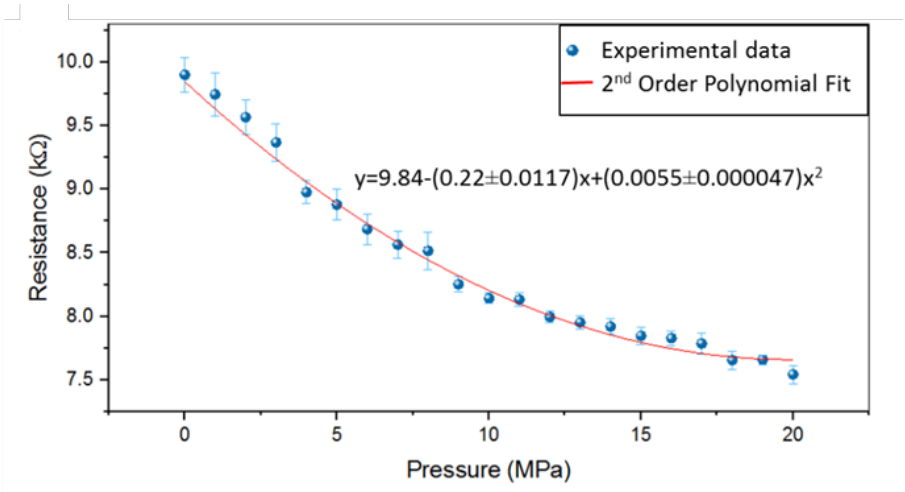

Figure 6.6 - The average resistance of five measurements of an LSG pressure sensor in the pressure vessel. The error bars indicate the standard devotion. The coefficient of determination (R^2) is 0.984.

6.4 Pulse rate monitoring

Daily pulse monitoring could provide abundant physiological and pathological information of the human cardiovascular system, but currently, popular optical methods have their limitations, especially at faster heart rates [228, 229]. While optical technologies have improved a lot, they still have inaccuracies and are prone to failure due to movement abnormalities at the sensor-skin interface and optical dispersion from time-varying motion (blood flow). Although mathematical strategies may be useful in some circumstances, the motion interference and heart-rate signals frequently overlap to the point where they are hard to distinguish [230]. Therefore, there is a need for improved wearable heart rate monitors. An alternative to optical methods is sensors that detect the pulse pressure wave on the radial artery [229, 230]. Due to its high sensitivity, the PMMA coated LSG pressure sensor was tested for this purpose. The LSG sensor in Figure 6.1a was attached to the wrist with an elastic band, allowing for real-time heart activity monitoring, as shown in Figure 6.7a. The magnified view in Figure 6.7b clearly shows two peaks associated with blood flow. *P1*, the 'novice wave,' is associated with cardiac shrinkage, while *P2* is the 'reflected wave' developed due to reflection from a peripheral blood artery. The radial artery augmentation index (AI), a determinant of the hardness of human blood, can be deduced using the obtained peaks:

$$AI = \frac{P2}{P1} * 100\%$$

From the signal shown in Figure 6.7b, $AI \cong 69\%$, which is a typical value for a healthy female [231]. Figure 6.7c shows the measurement over a duration of 10 s, from which a pulse rate of 84 beats per minute can be extracted.

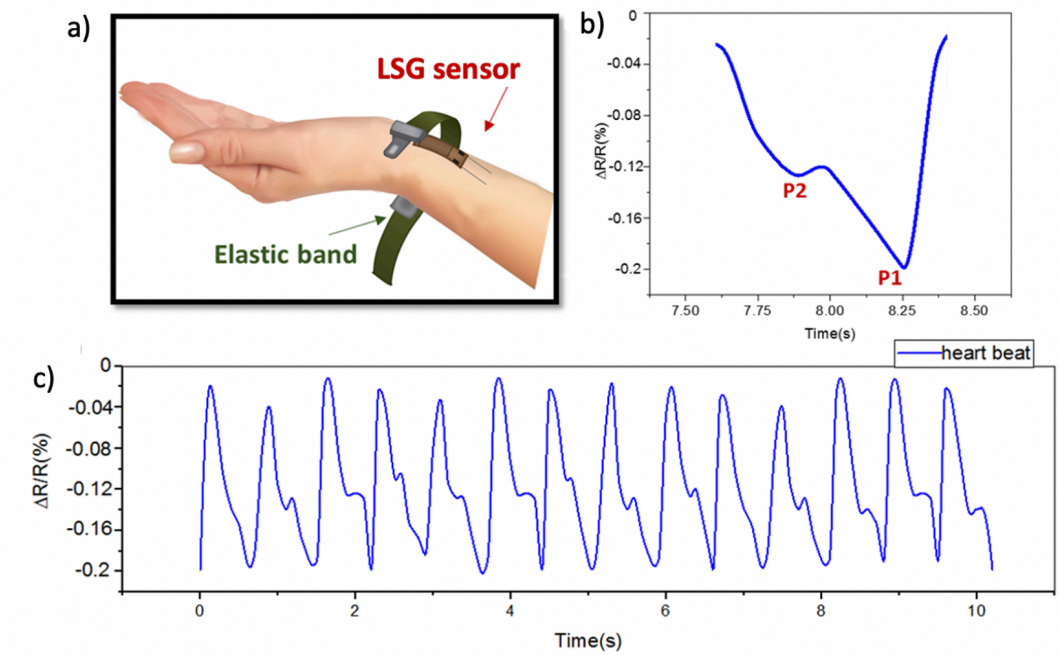

Figure 6.7 - a) Schematic of the wrist LSG pressure sensor for heart rate monitoring on the radial artery. b) Signal of one pulse. P1 is the 'novice wave,' associated with cardiac shrinkage, while P2 is the 'reflected wave' associated with the reflection from a peripheral blood artery. c) Measurements of the arterial pulse over 10 seconds.

6.5. Gait Analysis Sensors

The foot is the terminal link of the kinematic chain in human locomotion and it is subjected to daily repetitive pressures as a result of supporting the body's weight. Gait analysis has become a valuable technique for a thorough physical examination, joint kinematics, motion and muscle assessment, and treatment of limb deficits. [232]. Implementing a pressure sensor on foot for gait analysis necessitates robust yet flexible, imperceptible, and lightweight sensors to prevent interference with the gait. These

requirements are met by the LSG pressure sensors. A number of physical parameters were deduced from the pressure distribution of plantar pressure during gait analysis. We made five LSG sensors with the dimensions given in Figure 6.1a and used nylon stockings to connect them to the right foot of a test subject (55kg weight and 1.60 m height). As illustrated in Figure 6.8a, the sensors were utilized to detect pressure in five zones on the subject's foot: the heel (Zone A), lateral arch (Zone B), first metatarsal head (Zone C), lateral metatarsal (Zone D), and hallux (Zone E).

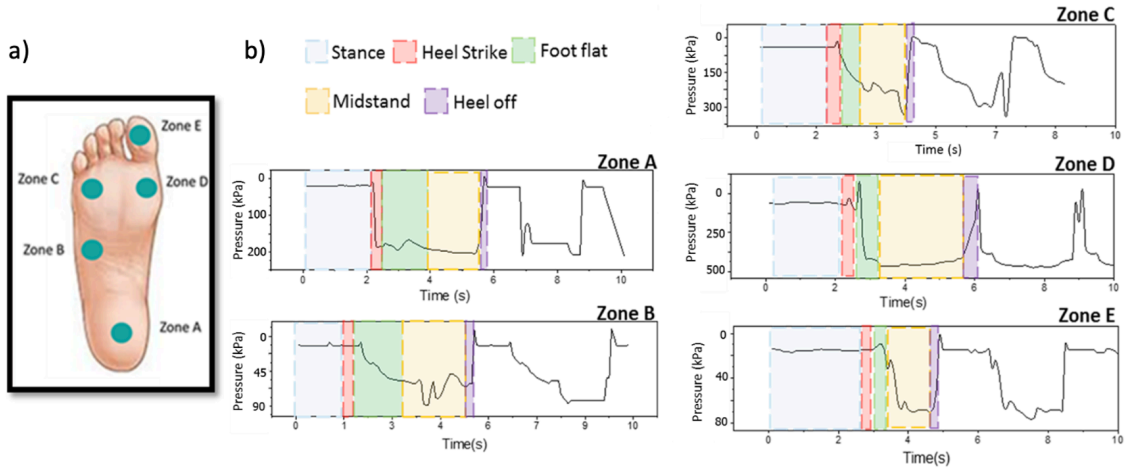

Figure 6.8 - a) Arrangement of LSG sensors on five zones for plantar pressure dynamic measurements. b) Signals obtained from the right foot of an able-bodied subject during a stride.

The signals in Figure 6.8b were recorded during several full gait cycles at a sampling rate of 100 Hz, where the fundamental five stages of a full cycle are highlighted (stance, heel off, foot flat, mid-stance, and heel off). The amplitude at different time points is associated with the foot falling on and off the ground during the walk. The highest variation of ~470 kPa was measured at the lateral metatarsal (Zone D), while the hallux experienced the least pressure on the foot in response to walking with a value of ~84 kPa.

6.6. Tactile Sensors

Measuring the intensity of touch is the realm of tactile sensors, which have attracted a lot of interest over the past years for robotic, prosthetic, and consumer applications [233, 234]. In order to mimic the tactile sense of the human skin, a sensitivity range between 0.01 N and 10 N is required [235], and typically, due to the shape of the structures, flexible sensors need to be employed. In many cases, durability is a concern since the sensors can be exposed to a corrosive environment, liquid, and elevated temperatures. LSG sensors feature high resistance to corrosion [236], biocompatibility, and an operating temperature range of up to ~400 °C. Figure 6.9 shows the response recorded from an LSG tactile sensor (structure as shown in Figure 6.1a) in response to being pushed with the index finger by a touch, softly pressed and hard-pressed. The output increased immediately at the moment of contact of the index finger and returned to the initial values after release.

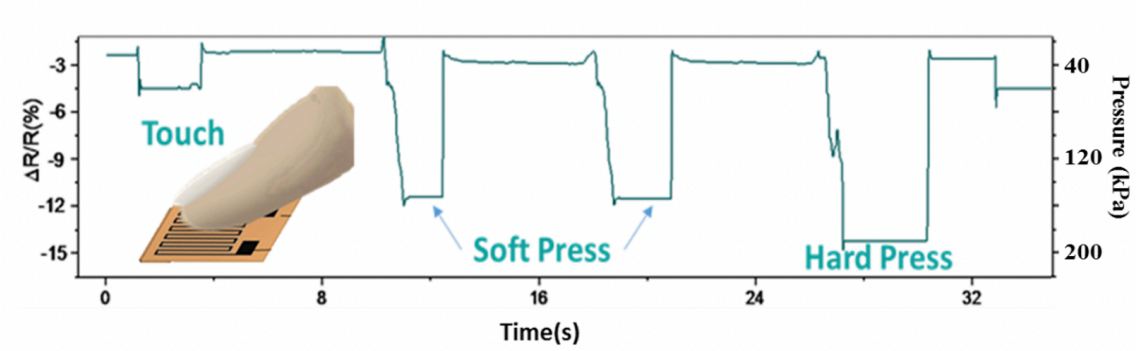

Figure 6.9 - The relative resistance variation induced by touch from the index finger.

6.7 Summary

Using LSG, versatile and reliable pressure sensors on flexible substrates have been developed with a wide pressure range. The pressure response resulted from the deformation of the conductive porous graphene structure, leading to changes in resistance, while a coating material served as a protection from sensor damage and electrical shunting. The size of the sensor may be easily customized thanks to the versatility of laser printing technology. It could be much smaller to allow for sensor integration, such as in the creation of a platform for conductivity, temperature, and depth (CTD) measurements for small marine organisms. In addition, the sensor has a high sensitivity of $1.23*10^{-3}$ kPa^{-1}, a low detection limit of 10 Pa, and outstanding cycle stability. It was used in a variety of applications, including a heart rate monitoring, gait analysis, and touch sensor, as well as underwater operations.

Chapter 7

Salinity Sensor

Human-induced rapid environmental changes have negatively impacted the marine environment, water quality, and marine biodiversity [237, 238]. Changes in oceanic physicochemical qualities have a huge impact on marine communities all around the world. In this context, large-scale, cross-disciplinary efforts are currently being made to build sensors capable of monitoring fundamental ocean phenomena. Salinity is a key factor in the regulation of global circulation, affecting water column stability, ion concentration and speciation, gas exchange between the air and the sea, and organism functional qualities [239]. Salinity has typically been determined manually by collecting samples and sending them to land-based laboratories for chemical composition analysis, which is time-consuming and labor-intensive [240].

The introduction of in situ biologging systems has enabled free-ranging animals to record the CTD of the water as they swim through their surroundings. These devices are typically bulky, mechanically rigid, produced with expensive multi-layer screening or standard micromachining/MEMS processes, and, most significantly, do not address the effect of biofouling [241, 242]. Indeed, the chemical composition of seawater, along with its biota, introduces two main challenges in salinity measurements, as seawater is (i) corrosive and (ii) rich in microorganisms that grow on solid surfaces and compromise sensor functioning [243]. Therefore, measurements conducted with existing solutions are not reliable long-term since the attachment of microorganisms on the electrodes causes

a drift of conductance towards lower values. Although work in the literature highlights that the attachment of organisms to the electrodes' surface could affect the measurement, none has addressed this issue. In addition, an increased interest in sensors on flexible substrates that can be attached to the curved surfaces of marine animals or follow their deformation, which is small in size, lightweight, and minimally intrusive, cannot be met with the existing CTD devices. Antimicrobial action and corrosion resistance associated with LSG make it a good contender for marine applications. Thus, LSG is used for reliable salinity measurements in hostile seawater environment [244, 245].

7.1. Methods and Operation Principle

A conductivity cell is a device that is comprised of electrodes that sense the electrical conductivity of a substance, such as seawater. Since the conductance of seawater is directly proportional to salinity, it is extensively used for salinity determinations. Ions present in a saline solution are responsible for the electrical conduction; therefore, the conductivity is directly correlated to salt concentration. Porous electrodes, such as LSG, improve the charge-transfer processes owing to large effective surface area, access to the electrolyte near the surface, and capacity for storing dissolution chemicals Thus, here LSG was used to realize conductivity cells using common two and four electrodes configurations.

Typically, a current, I, is driven through the solution, and the potential drop, V, is measured to obtain the conductance, G, by

$$G = \frac{I}{V}. \tag{3.4}$$

For two-electrode, such measurement was carried out by immersing electrodes in the saline solution, thereby forming a conductivity cell as shown in Figure 7.1a. Randles equivalent circuit is used to design an electrical model of LSG conductivity cell shown in

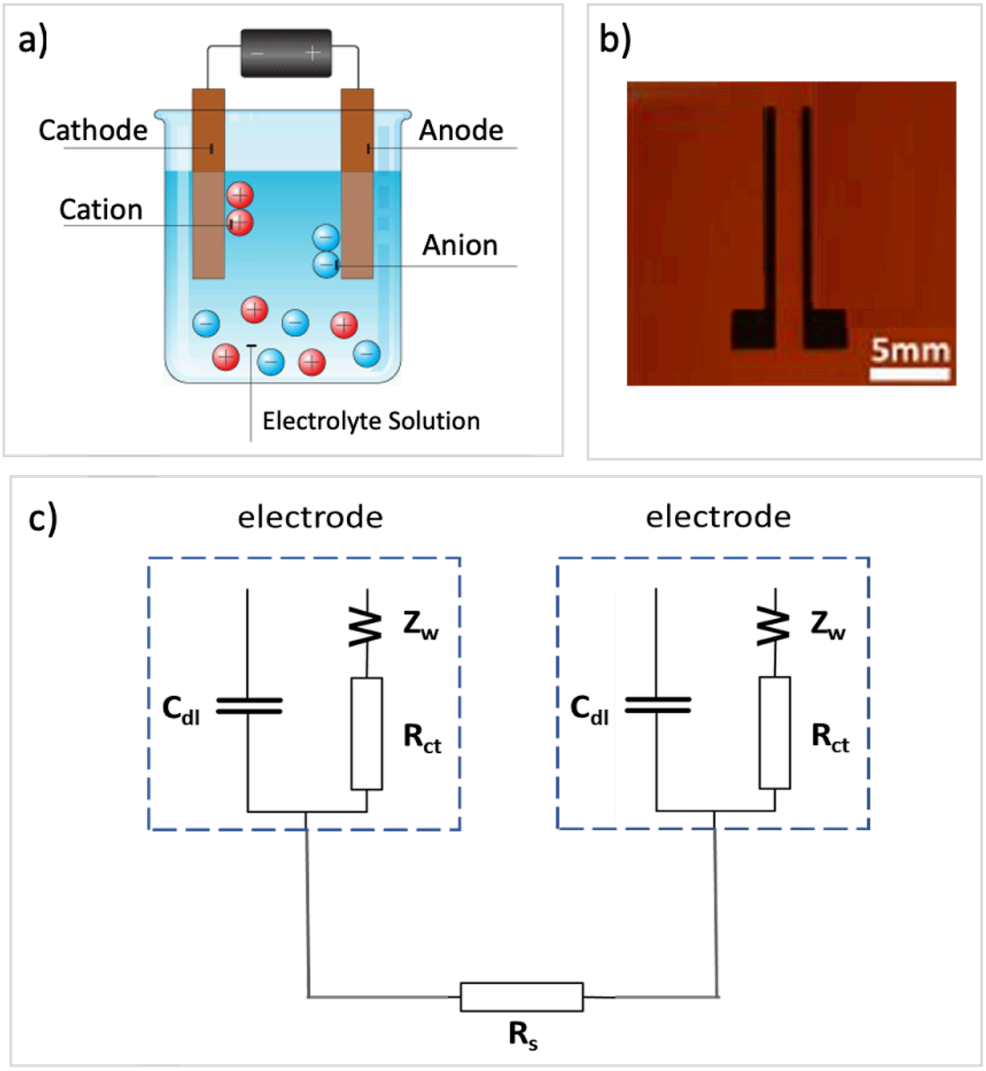

Figure 7.1 - a) Schematic of the two-electrode conductivity cell system. b) Two -electrode conductivity cell based on LSG. c) Randles equivalent circuit used to model parasitic phenomena in a two- electrodes cell

Figure 7.1c, taking into consideration the main parasitic components, i.e., (i) the formation of an electrical double layer on the electrode-solution interface electrical double layer, (ii) charge transfer phenomena caused by red-ox processes, and (iii) diffusion of ions close to the interface. The measured conductance is then multiplied by the cell constant K, a parameter related to the geometry of the cell, thereby obtaining the conductivity (*k*), which is the intrinsic property of the solution and does not depend on cell geometry.

The cell constant is given by

$$K = \frac{\text{distance between the electrodes}}{\text{surface area in contact with the solution}}, \tag{3.5}$$

whereas for planar electrodes and complex geometries, the cell constant must be calculated through software simulation, as reported by Hyldgård et al., [241, 246].

A conductivity cell composed of four electrodes is designed based on the simulation results reported in [246]. Two outer electrodes are used to drive an AC current, whereas two inner electrodes are used to measure the voltage drop across the water, as shown in Figures 7.2a and b. An AC is preferred to a DC current since the latter induces

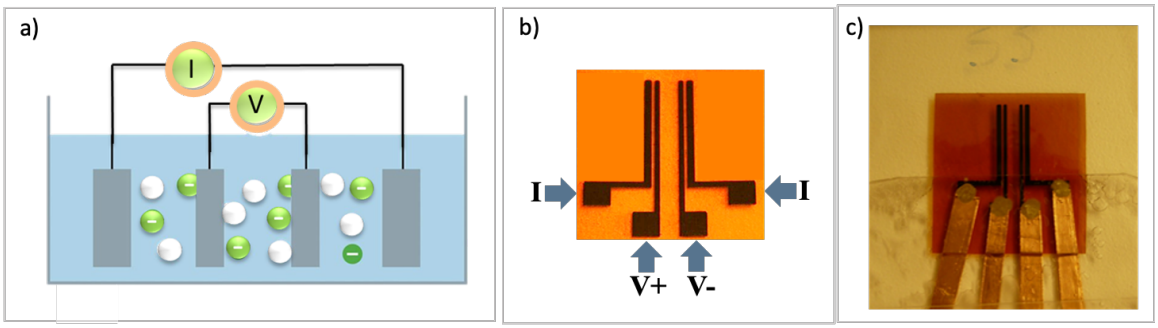

Figure 7.2 - a) Schematic of four-electrode conductivity cell. b) Conductivity cell realized using LSG. c) Fully assembled four-electrode conductivity cell based on LSG.

a constant ions drift towards the electrodes, consequently forming a large potential drop across the electrical double layer that affects the conductivity measurements. A four-electrode configuration substantially reduces the dependence on the electrical double layer [247], thus being suited for conductivity measurements in highly concentrated solutions, i.e., seawater. After fabricating the electrodes as described in Chapter 3.1, conductivity cells were attached to a 2mm thick PMMA sheet with instant adhesive glue to provide stable support (Figure 7.2c).

To investigate the performance of electrode conductivity cells, different solutions with 10, 18, 26, 34, 42, and 50 psu (1 psu=1 g/l) were made in a mixture of the corresponding amounts of NaCl and DI water. The solutions chosen allowed characterizing the sensor in a range of salinities that are typical for most of the water masses of the planet, both sea, and oceans. The cells were rinsed in DI water and soaked in the solution for 3 minutes. After measuring its properties, it was rinsed again in DI water and dried with nitrogen gas to minimize the contamination of the subsequent solution.

7.2 Four-Electrode Conductivity Cell

An impedance analyzer (Agilent 4294A), in combination with a four alligators fixture (Keysight 16089D Kelvin/Alligator Clip Leads), was used to characterize the response of a four-electrode sensor in the frequency range of 10-100 kHz. The phase and conductance were measured as a function of frequency with an AC current of 1 mA (RMS value). An averaging factor of 10 was used to improve the stability of the measured values. The

device showed a resistive response, as can be seen in Figure 7.3a by the phase values being close to zero. The transconductance in Figure 7.3b is frequency independent, and its value depends on the salinity. This allows differentiating the transconductance of the solutions across a wide range of frequencies.

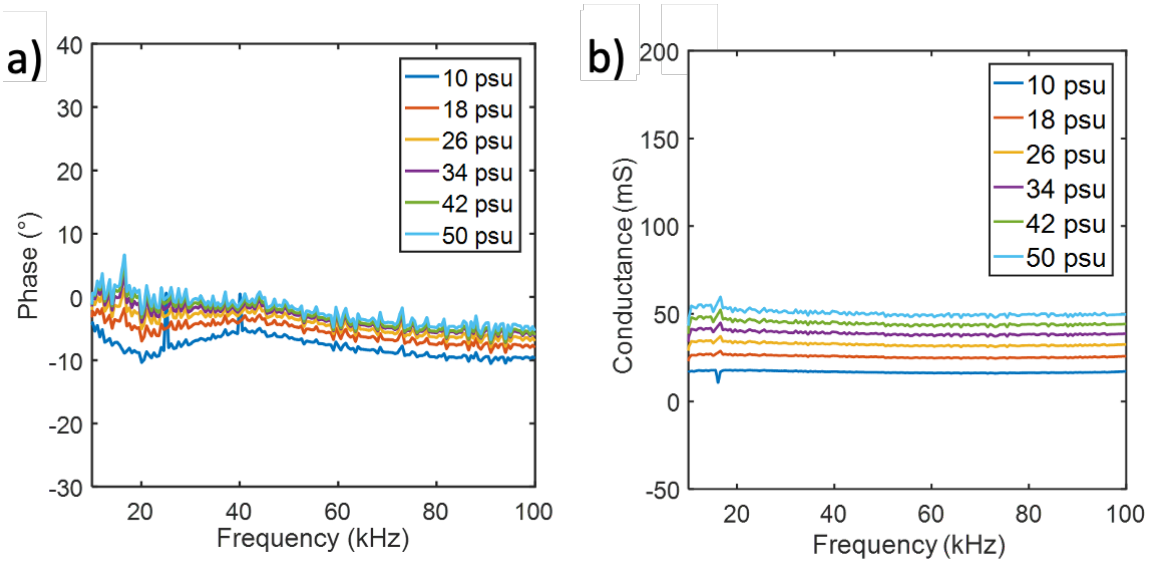

Figure 7.3 - Electrical characterization of the LSG sensor. a) The phase as a function of the frequency. b) The transconductance as a function of the frequency.

A test of the response time of the LSG sensor confirms that the procedure was sufficiently long to guarantee a stable value. To this end, the sensor was immersed in the solutions, and the transconductance was measured every ten seconds for five minutes. As shown in Figure 7.4 a stable value was obtained after ~2 minutes. The output signal stability was also tested for 10 hours by measuring conductance every hour, as shown in Figure 7.5.

The transconductance as a function of salt concentration is extracted from Figure 7.3b at a frequency of 20 kHz. Figure 7.6a shows the result, which is fit by a linear curve.

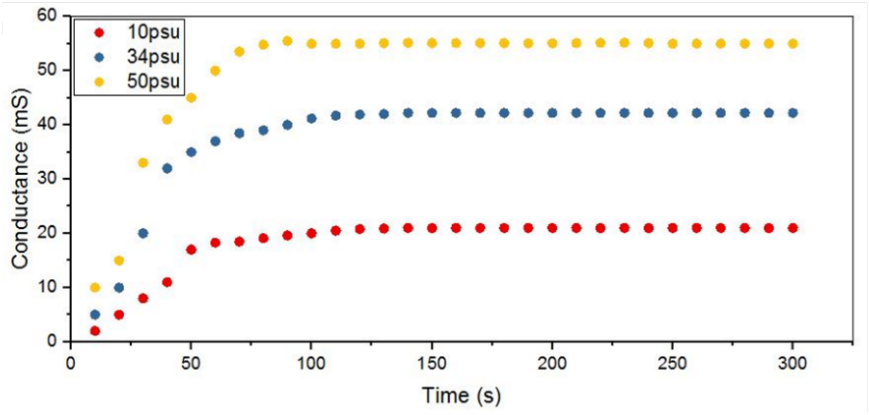

Figure 7. 4 - Response time of the LSG conductivity cell while immersed in different saline solutions.

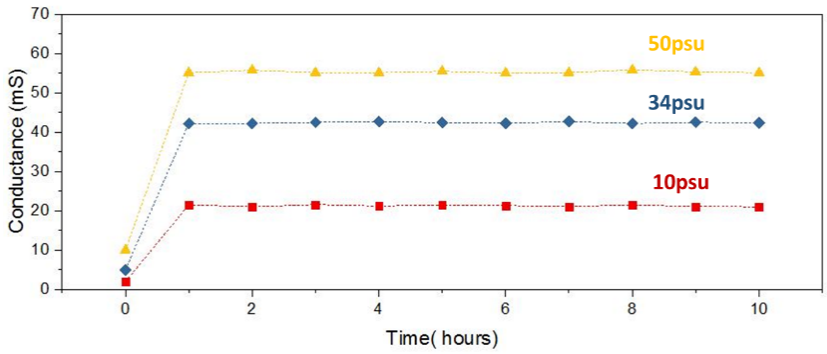

Figure 7.5 - The stability test of LSG conductivity cell while immersed in different saline solutions.

The linear fit provides a good approximation that has been used before [239] and the sensitivity of the LSG salinity sensor of 0.85 mS/psu was obtained. To investigate the response of the flexible LSG conductivity cell under bending, a sensor was glued on the outer wall of a plastic tube with a diameter of 2 cm, as seen in Figure 7.6b, and characterized following the same procedure. The response of the conductivity cell was consistent with the one in Figure 7.6a, indicating that the sensor's performance was maintained upon bending, and operation of the conductivity cell under various mechanical conditions is feasible. The values of transconductance are not the same as the

ones for a planar sensor because of geometrical factors. Indeed, the porous structure is stretched, leading to a larger electrodes area exposed to the saline solution; thus, modifying the geometry of the conductivity cell.

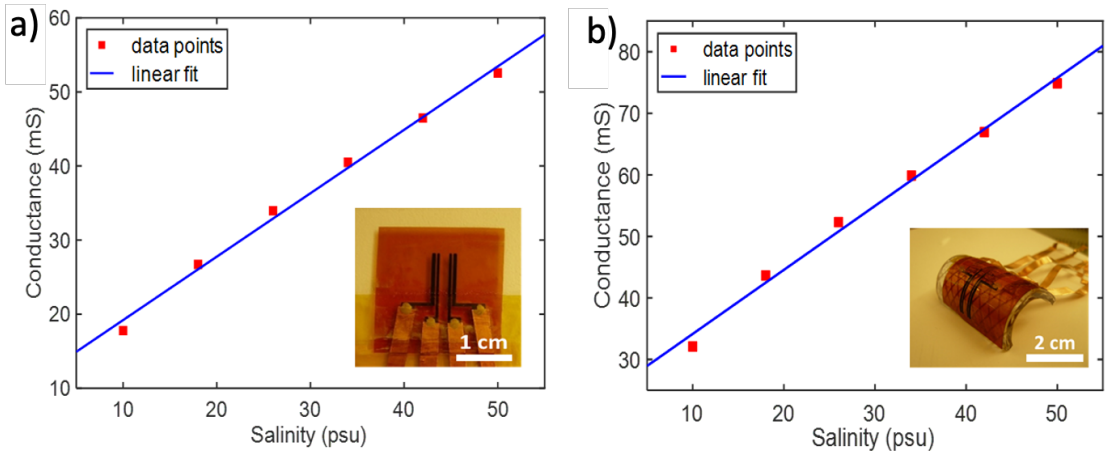

Figure 7.6 - Characterization of four-electrode conductivity cell. a) The transconductance as a function of salinity with a linear fit. b) The response of the sensor in the bent state.

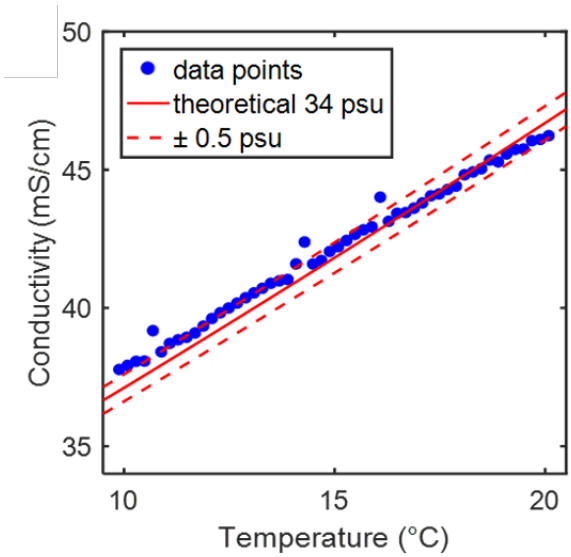

Figure 7.7 - Comparison between the theoretical curve and experimental results of conductivity as a function of temperature for the LSG conductivity cell.

In order to investigate the temperature dependence of the transconductance, a sensor was left in a 34 psu solution overnight at 4 °C, and the beaker was sealed with parafilm to avoid contamination. Then, the temperature was slowly increased until it

reached room temperature, whereby it was monitored with a commercial temperature sensor, and the transconductance was measured every 0.2 °C. Indeed, the temperature affects salinity measurements since the mobility of the ions increases with temperature [248]. Using UNESCO technical guidelines[249], the experimental values were fitted to theoretical ones. This fitting requires the introduction of a cell constant, *K*, taking into account that the transconductance, *G*, depends on the geometry of the conductivity cell. The conductivity, k, is related to the two parameters through cell constant, *K*. The multiplicative constant required for fitting the experimental data to the theoretical curve provides the value of $K = 1.2\ cm^{-1}$ for the LSG salinity sensor, obtaining the result reported in Figure 7.7. The experimental data points are in very good agreement with the theoretical ones and using the method described elsewhere [241] for determining the accuracy, a value of 0.5 psu can be extracted.

7.3 Two-Electrode Conductivity Cell

The spectrum was obtained using an impedance analyzer (Agilent 4294A) in combination with a 16334A Test Fixture (Tweezer Contacts), and two-electrode cells were characterized in the range of 100 Hz to 10 MHz. The impedance and phase were measured as functions of the frequency with an AC current of 1 mA (RMS value). A low driving current was chosen to minimize electrolysis of seawater, which may induce air bubbles on the electrodes' surfaces, thereby altering the value of the cell constant.

Figure 7.8a reveals that the impedance of the two-electrode conductivity cell decreases as a function of frequency. In the lower frequency range, the impedance slightly varies with the salinity and shows a poor correlation. On the other hand, at high frequencies, the impedance strongly depends on variations of the salt concentration, and the phase reaches approximately 0° at 10 MHz (Figure 7.8b). This confirms that the impedance at high frequencies is related to the medium's conductance, whereas capacitive, diffusive, and charge transfer effects are negligible. The hypothesis is supported by simulating Randles equivalent circuit using LTSpice, where electrode resistors (R_{el}) are connected in series with the solution resistor (R_S) and a parallel circuit of total capacitance (C_t), charge-transfer resistor (R_{ct}), and Warburg element (C_z). C_t is the equivalent capacitance associated with the double-layer (C_{dl}) and biofouling (C_{bf}) layer (Figure 7.9a).

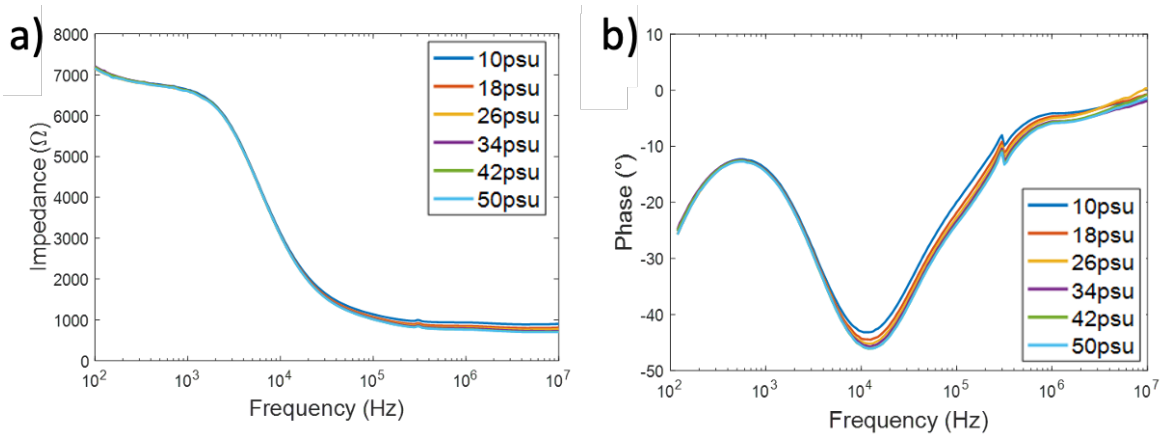

Figure 7. 8 - a) Impedance and b) phase measured as a function of frequency and salinity with a two-electrodes conductivity cell.

Using the component values of Table 7.1, a good agreement with the experimental curve is obtained, as shown in Figure 7.9 b, c. Since at high frequencies, the impedance is given

by the sum of the resistances of the electrodes and of the saline solution, parasitic effects, including biofouling, will be minimized in the response of the sensor.

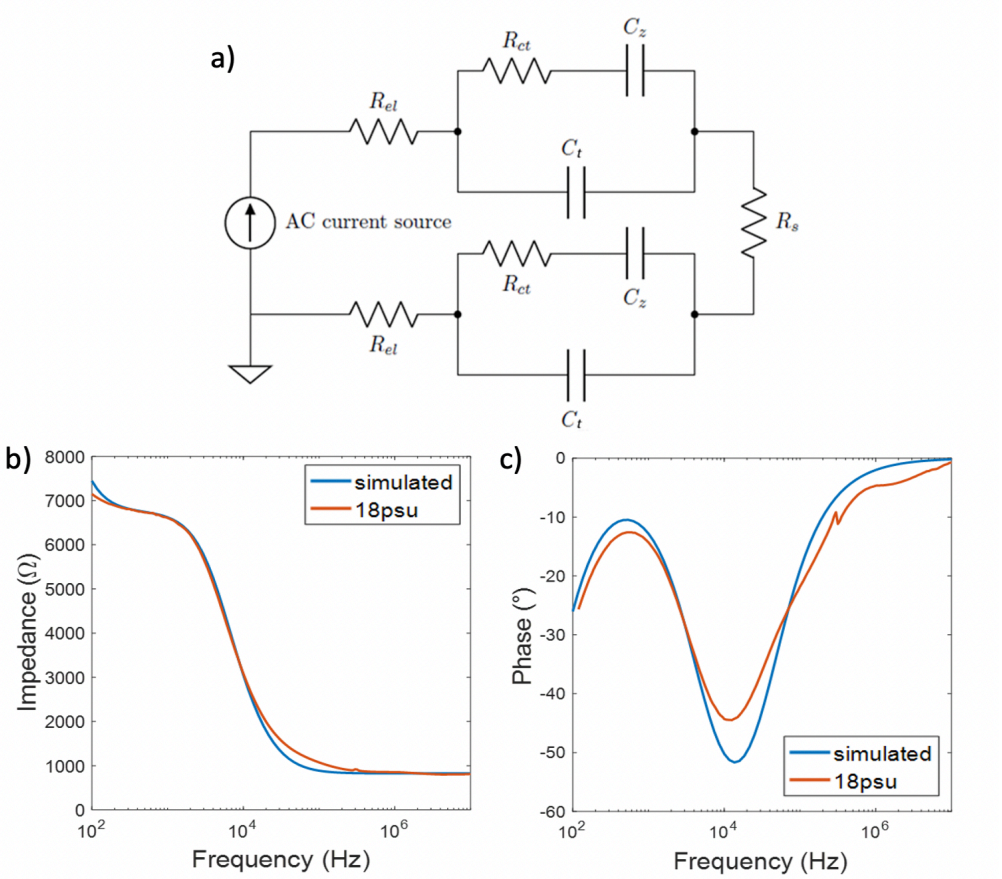

Figure 7.9 - a) Schematic of the equivalent circuit used for the simulation with LTSpice. b) Impedance over frequency obtained by simulation and experiment. c) Phase as a function of frequency obtained by simulation and experiment.

Table 7.1 - Simulation values of the components

R_{el}	350 Ω
R_{ct}	3000 Ω
C_z	1 uF
C_{dl}	11 nF
R_s	150 Ω
Current Source	1 mA (100 Hz-10 MHz)

The impedance, at 1MHz, as a function of salinity is shown in Figure 7.10a, where the frequency was chosen arbitrarily since the measurement is frequency independent within

the range of 1 MHz to 10 MHz. The results confirm that the impedance at high frequency is inversely proportional to the salinity. The response of the flexible two-electrode conductivity cell under bending was evaluated by gluing a sensor onto the outer wall of a plastic tube with a radius of 1 cm (inset of Figure 7.10). The measured values are consistent with the planar electrodes, indicating that the sensor's performance is maintained upon bending, and operation of the conductivity cell under various mechanical conditions is feasible.

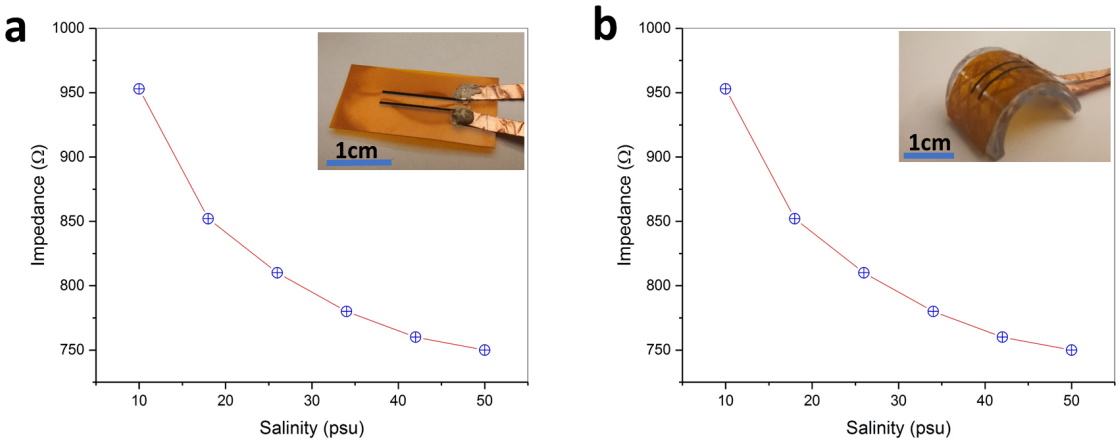

Figure 7. 10 - Sensor impedance extracted from Figure 3b at 1 MHz a) as a function of salinity and b) as a function of salinity while the sensor is bent with a 1 cm radius of curvature. The insets show photographs of the sensors.

In order to investigate the temperature dependence of the sensor, it was immersed into a 34 psu solution and placed into a temperature chamber (Su-221, Espec). The temperature was slowly increased from -4 °C to room temperature, and the impedance was measured every 0.5 °C. Since the impedance decreases linearly with temperature,

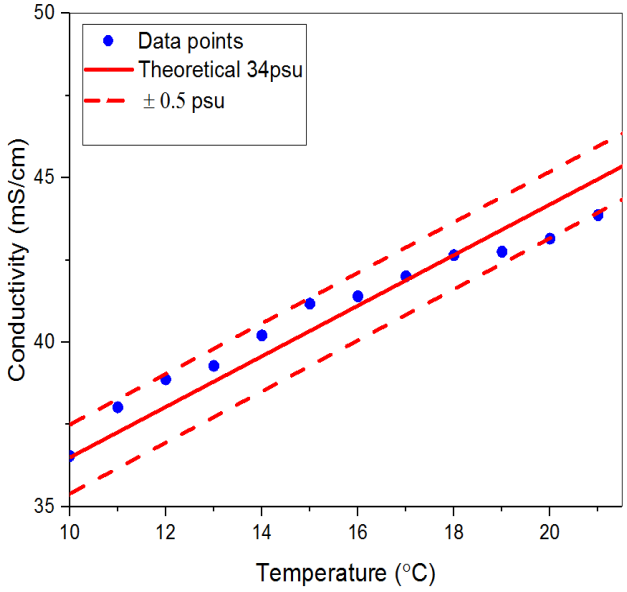

Figure 7.11 - Conductivity as a function of temperature for the LSG conductivity cell.

the conductance increases, this implies that temperature affects the salinity measurements, which is expected as the mobility of the ions increases with temperature. An evaluation of the accuracy of the sensor can be accomplished by fitting the experimental result to the theoretical curve based on the UNESCO technical papers in marine science [249]. The fitting requires to calculation of the conductivity, which is obtained by multiplying the measured conductance by the cell constant. A cell constant of K = 35 cm^{-1} provided a good fit and was used to obtain the result shown in Figure 7.11. The measurement results follow the theoretical curve, and an accuracy of 0.5 psu can be extracted.

7.4 Biofouling Assessment

In order to conduct a biofouling assessment and investigate biofoulants' recruitment on LSG and their effect on the performance of the sensor, both sensors were deployed at

a coral reef along the central Saudi Arabian coast of the Red Sea for up to 7 weeks (Figure 7.10a). This provided an extreme test of corrosion and biofouling because of the hypersaline nature of the Central Red Sea (salinity > 39) and the rapid recruitment and growth of biofouling organisms characteristic of coral reefs [250]. This period of time was needed for the fouling process to be substantial since biofouling is constituted by three main phases: (i) conditioning film, (ii) microfouling, and (iii) macrofouling [243]. Figure 7.10b shows the characteristic curve of the LSG salinity sensor before and after 7 weeks in the seawater. The values of transconductance are lower after the seawater exposure by 17% on average. This implies that the cell constant became higher; hence

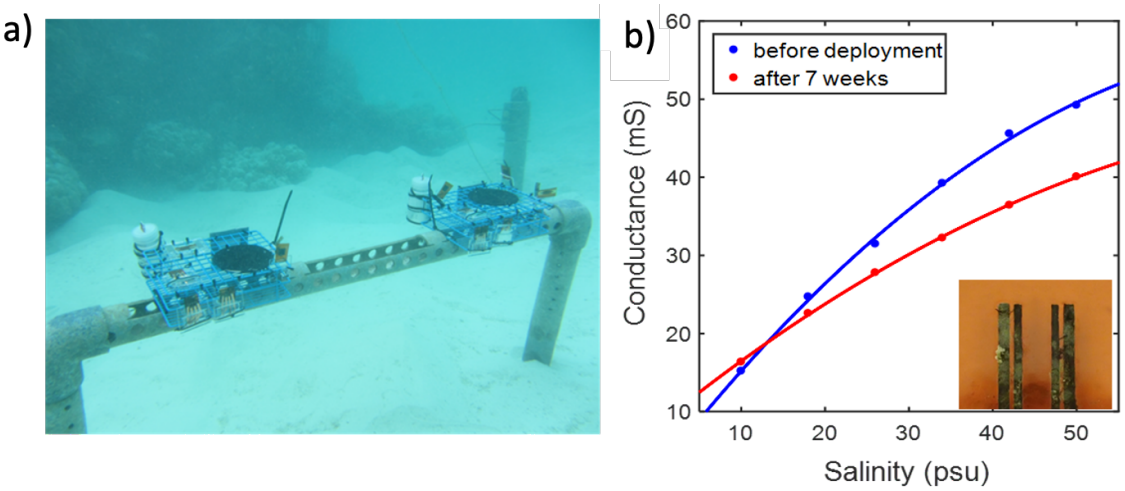

Figure 7.10 - a) The sensors deployment at Al Fahal reef in the Red Sea (geographic coordinates: 22.25285, 38.96123) for the biofouling study. b) LSG sensor response before and after deployment in the Red Sea for 7 weeks.

the area exposed to seawater was smaller, which was caused by the attachment of organisms to the LSG surface (see inset in Figure 7.10b). The area covered by biofoulants is about 22% (measured by ImageJ software). This value is in agreement with the shift

towards lower values of *G*. In fact, a decrease of the cell constant should induce approximately the same percentage decrease of *G*.

Meanwhile, Figure 7.11 shows the measurement results of the two-electrode LSG salinity sensor before deployment and after 1-3 weeks in the sea. The insets of Figure 7.13 show the accumulation of biofouling. Different impedance ranges are due to manual packaging with PMMA sheets, which changes the resistance of the connecting electrodes. No overall drift of the impedance is observed after prolonged exposure to seawater, therefore suggesting that this method can solve long-term biofouling issues. Using ImageJ software [251], the area of the graphene surface covered by biofoulants was found to be 18%, 32.27%, and 46.4% after 1, 2, and 3 weeks respectively. Nevertheless, the impedance values measured at 1 MHz before and after exposure to seawater are very similar and clearly enable discerning different salinities without being affected by the biofouling. This confirms the assumption that the biofouling layer attached to the LSG electrodes acts as an additional capacitor, which has a negligible impedance at high frequencies. The total capacitor (C_t), shown in Figure 7.9a, is associated with a parallel configuration of the double layer (C_{dl}) and the biofouling capacitor (C_{bf}). Some differences between the values before and after deployment are attributed to the connection with the tweezers used to carry out the measurement with the impedance analyzer, which affects the calibration and contact resistance. However, the response does not show an overall shift of the values, thereby confirming that high-frequency impedance spectroscopy allows achieving long-lasting and reliable salinity sensing systems.

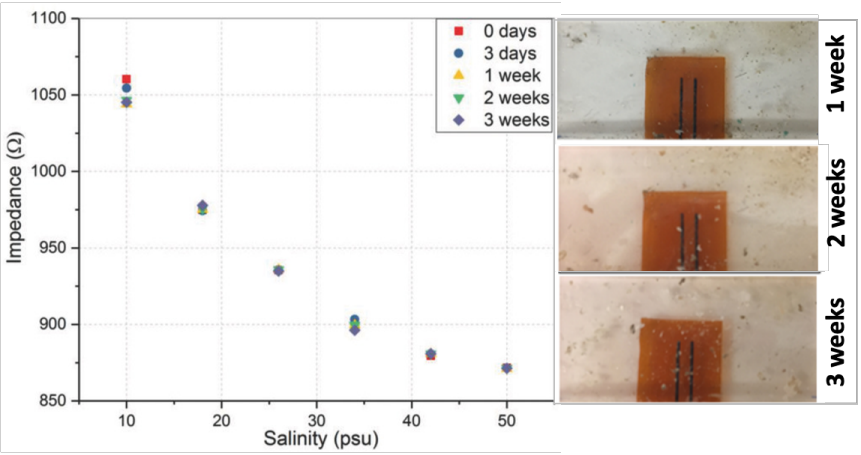

Figure 7.11 - Average response of two-electrode conductivity cells at high frequency (1 MHz) before deployment and after different periods of time in seawater.

7.5 Summary

The field of sensors for marine applications is rapidly growing because human impacts are altering oceanic physio-chemical properties, which are having drastic effects on marine communities worldwide. The existing salinity sensors are expensive, bulky, and rather intrusive, which considerably limits their applicability. LSG conductivity cells for salinity measurement offer flexibility, low cost, lightweight and mechanical as well as chemical resistance in seawater. The single-step fabrication method is a key feature, which distinguishes this sensor from standard MEMS processes used before for the fabrication of the electrodes. The four-electrode conductivity cell is characterized by a high sensitivity and allows operation in different configurations, i.e., planar or bent, with an accuracy of ±0.5 psu. The results show that the conductance can be measured at low frequencies (10-100 kHz). Although affected by biofouling, as opposed to previously reported results [245], the sensor can withstand prolonged exposure to the harsh marine environment and still operates after retrieval. For long-term measurements, a biofouling

study revealed that the previously reported antimicrobial action of LSG is not capable of preventing biofoulants' attachment to the surface in a real seawater environment, which strongly affects the measurement results in commonly used low-frequency setups. In order to overcome this issue, high-frequency impedance measurements with a two-electrodes conductivity cell were proposed. It was found that this measurement is not affected by the biofouling and reliably measures salinity even after 3 weeks of deployment in the waters of the Red Sea.

Chapter 8

Hall-Effect Magnetic Sensor

Magnetic sensing capabilities, integrated into flexible substrates, can provide unique properties, enabling to sense displacement, orientation, proximity, etc.[252-255]. Currently, silicon CMOS-based Hall sensors are the most commonly used magnetic field solid-state sensors, mainly due to low-cost production and compatibility with standard microelectronic processes. Flexible Hall effect sensors have been realized in different ways, including by stacked thin films, such as bismuth [254, 256], permalloy [254], and graphene[257], deposited on a flexible substrate, such as PI, PET, and PEEK. In particular, graphene has risen as a promising channel material for constructing high-performance magnetic sensors due to outstanding material merits, such as ultra-high carrier mobility, mechanical flexibility, atomically thin active body, and linear energy dispersion near the Fermi level [257, 258]. Graphene Hall sensors have been reported with high performance in several vital aspects, such as sensitivity, linearity, and temperature stability[259]. Since technologies for graphene processing are still at an early stage, there is a limit for its practical applications in advanced electronics.

In this chapter, LSG is used to fabricate highly flexible Hall Effect sensors. To demonstrate the potential application of the LSG Hall sensor, it was combined with a deformable elastomer and a flexible magnet to realize a compliant soft tactile sensor[260].

8.1 Methods and Operation Principle

Figure 8.1a illustrates a flexible large-area array of Hall-effect sensors. The versatility of the laser scribing technology allows tailoring the geometries and sizes of the sensors, as shown in Figure 8.1b**.** A single cross-shaped LSG Hall sensor, shown in the inset of Figure 8.1a (horizontal and vertical lengths of a = 8 mm and b = 3 mm, respectively; electrode strip width of *w* = 0.87 mm), was used in a four-terminal Hall-measurement configuration in all experiments reported herein.

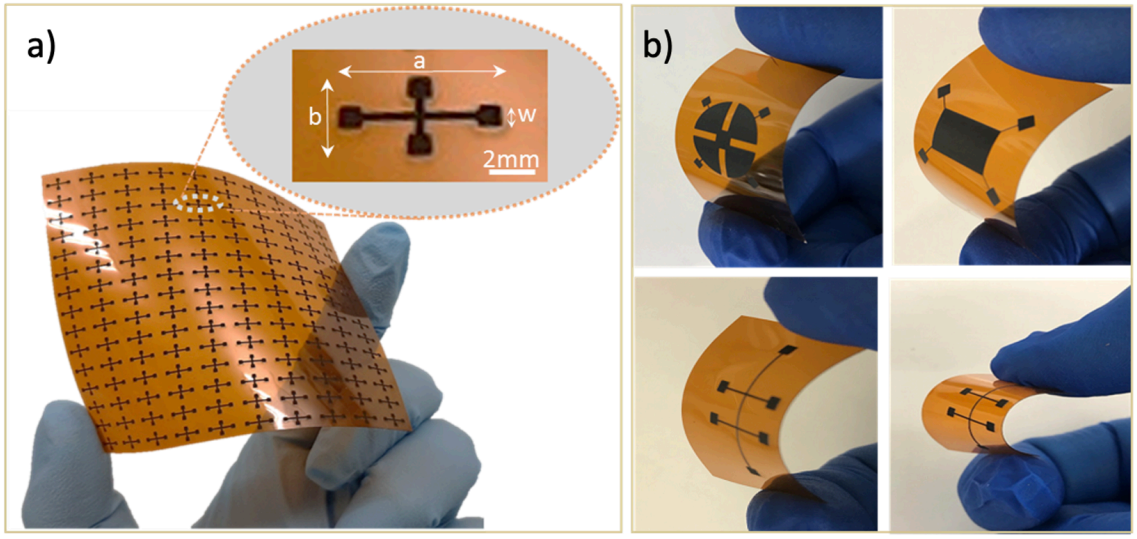

Figure 8.1 - a) An array of printed flexible LSG Hall effect sensors. The inset shows a single cross-shaped LSG Hall sensor and b)Examples of various device architectures and geometries.

Hall-Effect sensors are characterized by the generation of a transverse electric field upon application of an electric current and a magnetic field perpendicular to the current. The Lorentz force, which is a combination of two forces: electric and magnetic, is the primary physical principle underpinning the Hall effect. When an electron flows in electric

field, *E*, perpendicular to an applied magnetic field, *B*, it encounters a magnetic force normal to both directions given by

$$F=q(v \times B), \tag{8.1}$$

where elementary charge is denoted as *q* and particle velocity as *v*. The force exerted on charged particles by both fields is given by

$$F=q(E+v \times B). \tag{8.2}$$

In the context of a z-directed magnetic field and a constant current, I_c, flowing along the x-axis (Figure 8.2a), electrons exposed to the Lorentz force initially migrate away from the current direction toward the y-direction , leading to an increased surface electrical charge on this side of the specimen. The Hall voltage, V_H, is a voltage drop across the two sides of the specimen caused by this charge.

$$V_H = \frac{IB}{qnd}, \tag{8.3}$$

where *n* and *d* represent the charge carrier density and material thickness, respectively.

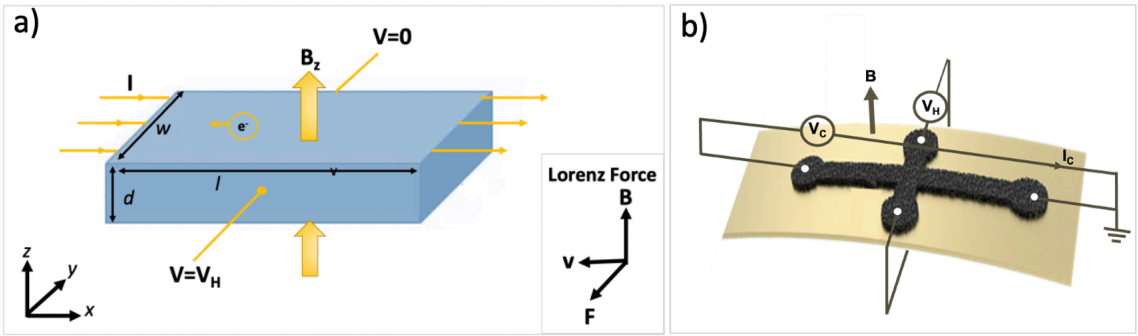

Figure 8.2 - a) Schematic of Hall-Effect sensor; b) Four-terminal Hall-measurement configuration of the Hall sensor.

The sensor sensitivity is defined as the slope of the Hall response normalized to the value of the supply current, I_c, or voltage V_c by

$$S_I = \frac{1}{I_c} \left| \frac{\partial V_H}{\partial B} \right|. \quad (8.4)$$

The other two important quantities of the material are the carrier mobility, μ, and the sheet carrier density, *n*. These values can be deduced using normalized voltage, S_v, and current sensitivities, S_I, by

$$\mu = S_v \frac{L}{W} \quad (8.5)$$

and

$$n = \frac{1}{S_I e} \quad (8.6)$$

where *L* is the length and *W* is the width of the Hall - effect sensing unit. A single cross-shaped LSG Hall sensor was examined in a four-terminal Hall-measurement configuration, as shown in Figure 8.2.

8.2 Characterization Techniques

The four-terminal LSG Hall-measurement configuration shown in Figure 8.2b was established using the Physical Properties Measurement System (PPMS, Ever Cool II, Quantum design Inc.). The Hall voltage, $V_{H,}$ was measured by applying a magnetic field ranging from -7 T to 7 T in the perpendicular direction, with a constant current flow, I_C, of 100 μA.

Extensive bending tests were performed by exposing the LSG Hall sensor to varying strain values and characterized using Manual Transport Measurement Setup depicted in Figure 8.3. The sample was first attached to the surface of flexible molds with various cross-section diameters, such that the bending radius followed the dimensions of the

molds. The PI bending was performed one time for bending radii of 2 mm, 5 mm, and 7.5 mm, with the LSG Hall sensor being on the external site of the curvature. The resultant tensile strain was then estimated by the ratio of the sensor thickness (161 µm) to the bending diameter. Additionally, the application of 1000 bending cycles was achieved using an electromechanical pull tester (5900-Series, Instron), where each bending cycle involved bending the sensor to a radius of 5 mm and releasing it. The noise measurements were conducted in ambient conditions, and a frequency range from 3 Hz to 1 kHz at zero magnetic fields through the circuitry shown in Figure 8.4. The B_1 and B_2 contacts of the LSG Hall sensor were connected to a Spectrum Analyzer (E4448A PSA), while a constant bias current I_C between the contacts A_1 and A_2 was applied by a Keithley 4200.

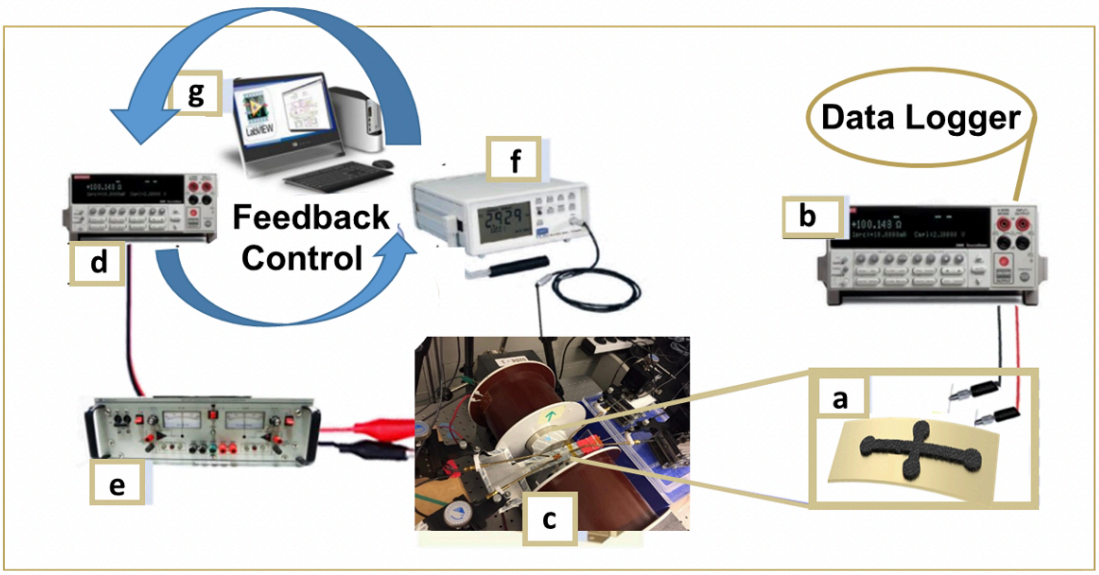

Figure 8.3 – The diagram of experimental setup. a) LSG Hall-effect sensing unit. b) Sourcemeter in resistance mode. c) Helmholtz coils. d) Sourcemeter series in current mode. e) Bipolar Amplifier. f) Gaussmeter. g) A PC with LabView for control and data storage.

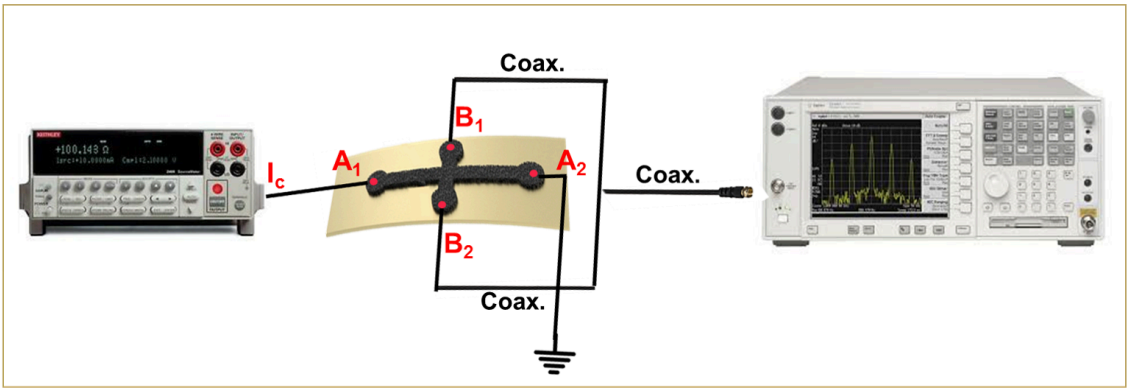

Figure 8.4 - The noise measurement setup.

8.3 Magneto-electro-mechanical response

The measured Hall voltage values were obtained by averaging over 1 minute and plotted as a function of the magnetic field in Figure 8.5. The Hall voltage shows a linear dependence on the applied magnetic field, as expected, with a current normalized sensitivity of ~1.12 V/AT, extracted from the slope of the plotted line. Using the standard protocols of the Van der Pauw measurements from the National Institute of Standards and Technology[261], carrier mobility, μ = 736 $cm^2V^{-1}s^{-1}$, and a sheet carrier density, n = $5.6 \cdot 10^{14}$ cm^{-2}, was found at room temperature. The obtained values are comparable with flexible bismuth[256], graphene[257, 262], and metal-based[263] Hall sensor elements on PI, PEEK, and Kapton Foil substrates. Meanwhile, the offset in the Hall voltage arises from misalignment of contacts and/or inhomogeneous current flow in the active sensor area. This is a common issue found in Hall-effect sensors, which can be minimized by various circuit techniques, such as auto-zeroing [264], chopper stabilization [265], and correlated double sampling [266].

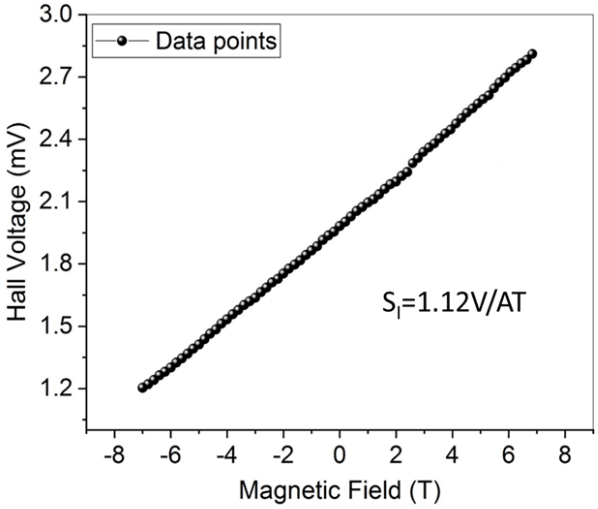

Figure 8.5 - Hall voltage over the external magnetic field at a current of 100 µA.

The output of the sensor before, during, and after exposure to different strains is shown in Figure 8.6a. The sensitivity remained stable after being bent to a minimum radius of 5 mm, which corresponds to a tensile strain of ~1.6%. The reduction in Hall sensitivity induced by an increased bending curvature can be attributed to the reduced active area perpendicular to the magnetic field. A decrease in bending radius (<5 mm) leads to the magnetic field component parallel to the current direction, B_x, to increase, and the component orthogonal to the current direction, B_y, to decrease, resulting in the reduction of the Hall voltage. The current normalized sensitivity measurements revealed no degradation after 1, 10, 100, and 1000 cycles of bending (radius of 5 mm), demonstrating the flexibility and robustness of the LSG Hall sensor devices (Figure 8.6b). This observation is consistent with results obtained from the SEM images (Figure 8.7), which revealed that there is no perceptible change or damage in the morphology of the LSG after 1000 bending cycles.

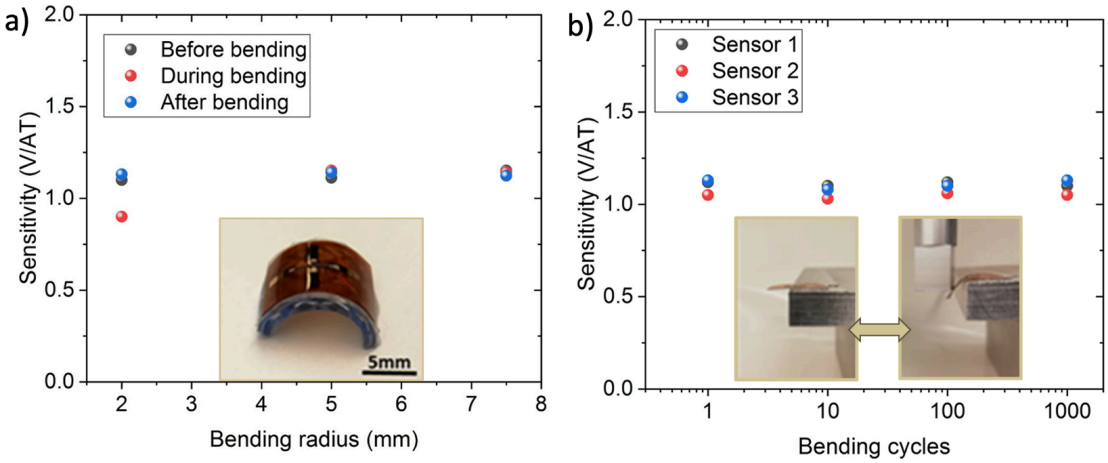

Figure 8.6 - a) The current normalized sensitivity for the LSG Hall sensors before, during, and after one time bending to a certain radius. b) The bending cycle measurements for the current normalized sensitivity of LSG the Hall sensor.

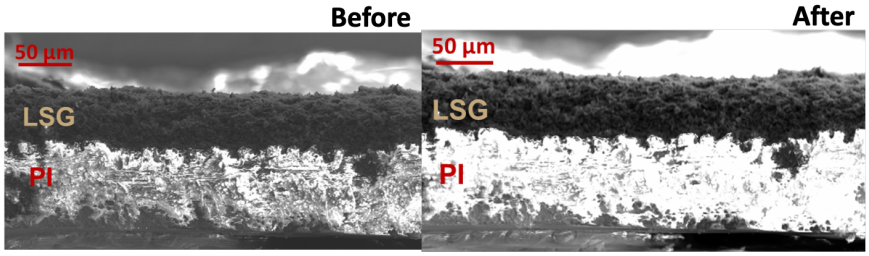

Figure 8.7 - Cross-section of the LSG Hall sensor a) before and b) after exposing it to bending cycles.

8.4 Effects of Temperature

Thermal gravimetric analysis was used to assess the effect of temperature on the LSG Hall sensor in Chapter 3.4. Here, the effect of temperature on the current normalized sensitivity was thoroughly examined. The sensitivity of the LSG Hall effect sensors remained stable from -33.15 °C to 400 °C, making them attractive solution for high- and low-temperature applications.

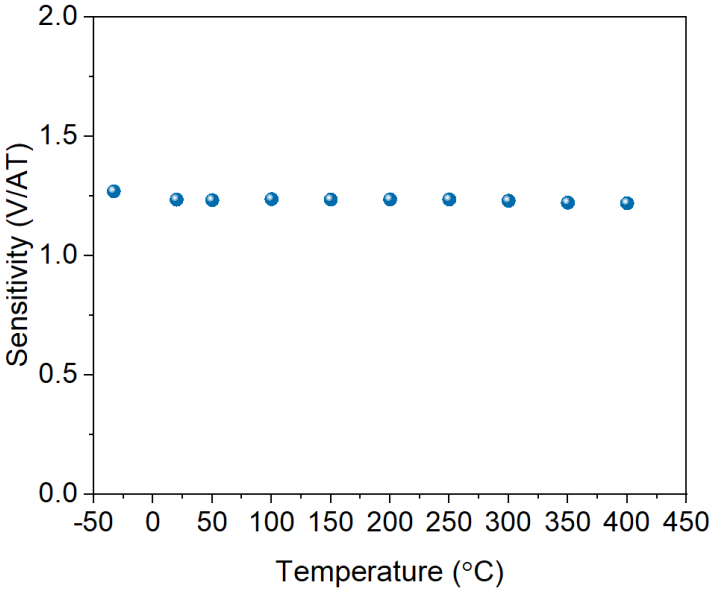

Figure 8.8 - The sensitivity of the sensor as a function of temperature.

8.5 Noise Measurements

The voltage noise spectral density, $V_{n,}$ and magnetic resolution, B_{min}, which are determined by both signal and noise levels, are important parameters, for instance, to evaluate the detection limit. The obtained voltage noise spectral density, V_n, shown in Figure 8.9a, reveals that the noise is dominated by *1/f* or Flicker noise up to a corner frequency, *fc* = 17.6 Hz. The origin of *1/f* noise in graphene Hall effect devices has been the subject of several experimental studies [259, 267-269], and it is widely accepted that it arises from 'exchange noise' due to, for example, carrier capture and release at traps, leading to fluctuations in the carrier density. Below the corner frequency, the noise increases linearly with increasing bias current (inset of Figure 8.9a), which is induced by the higher number of fluctuations in electron carrier density. Above the corner frequency, the thermal noise voltage floor is as low as 50 nV/$\sqrt{\text{Hz}}$, which is in the range

of previously reported values of ultra-low noise graphene Hall sensors [257, 259]. The magnetic resolution, B_{min}, can be calculated using the voltage noise spectral density, V_n, and the sensitivity of the sensor by [257, 267]

$$B_{min} = \frac{Vn}{S_I I_c}. \tag{8.7}$$

The magnetic resolution, B_{min}, of the LSG Hall sensor as a function of frequency is shown in Figure 8.9b, where the minimum detectable magnetic field is as low as 0.446 mT/$\sqrt{\text{Hz}}$.

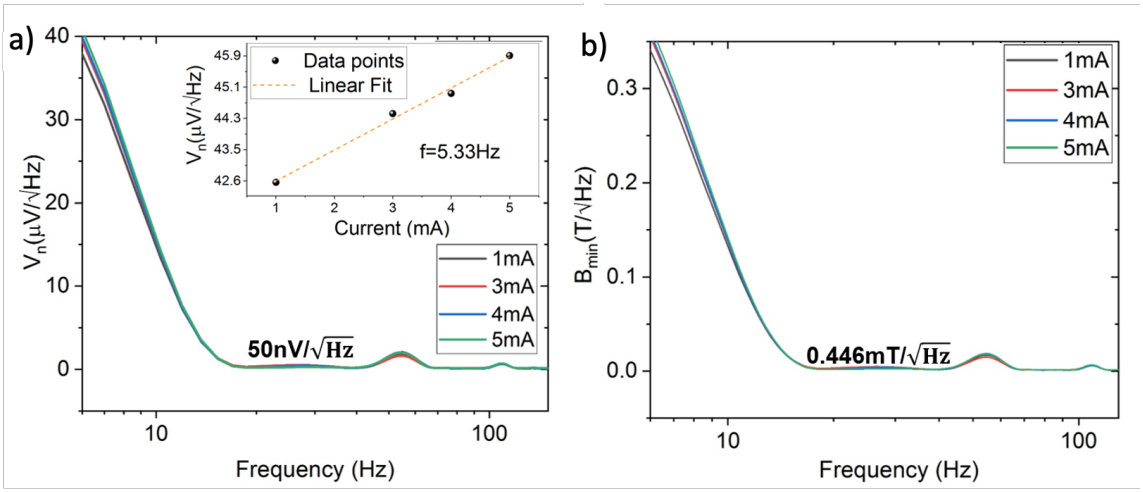

Figure 8.4 - a) Voltage noise density, V_n, and b) magnetic resolution, B_{min}, as a function of frequency.

8.6 Soft tactile sensor

An initial attempt to utilize a linear Hall sensor in the artificial hand of a robot has been proposed by Kyberdt et al. [270], where the external normal force applied to the surface of the elastomer induced the displacement of the embedded magnet, which was estimated by measuring the magnetic field vector through the Hall sensor. The force exerted to the elastomer could then be determined using the mechanical parameters of the elastomer. A rigid permanent neodymium magnet had been utilized in previous

investigations to provide a magnetic field [270-272]. The Hall effect sensor was quickly saturated after embedding the rigid component of the magnet into the soft structure of the tactile sensor [273], limiting the measurable force range. The permanent magnet also required a specific distance from the Hall sensor, restricting the structure's minimum thickness [273]. In this study, the rigid permanent magnet was replaced by a magnetic skin that has relatively similar mechanical properties as the elastomeric body and which allows customization of the magnetic properties [274, 275].

The developed LSG Hall sensor was integrated into a flexible and soft tactile sensor. The tactile sensor was realized by packaging a flexible magnet, a soft elastomer, and the LSG Hall sensor into a single architecture of 10 mm x 10 mm shape, as shown in Figure 8.10. Applying a normal force to the top of the platform changes the distance between the flexible magnet and the LSG Hall sensor through the deformation of the elastomer, causing a magnetic field variation at the sensor location. Three layers of the platform were fabricated separately and then stacked together using the sticky surface of the Ecoflex elastomer [276, 277]. The LSG Hall sensor (thickness of PI: 0.12 mm) was embedded in the bottom layer of the structure. The middle section is composed of silicone elastomer (2 mm thick Ecoflex, Smooth-on), which was prepared by casting into a mold and planarized using a casting blade. The top layer of the structure is an

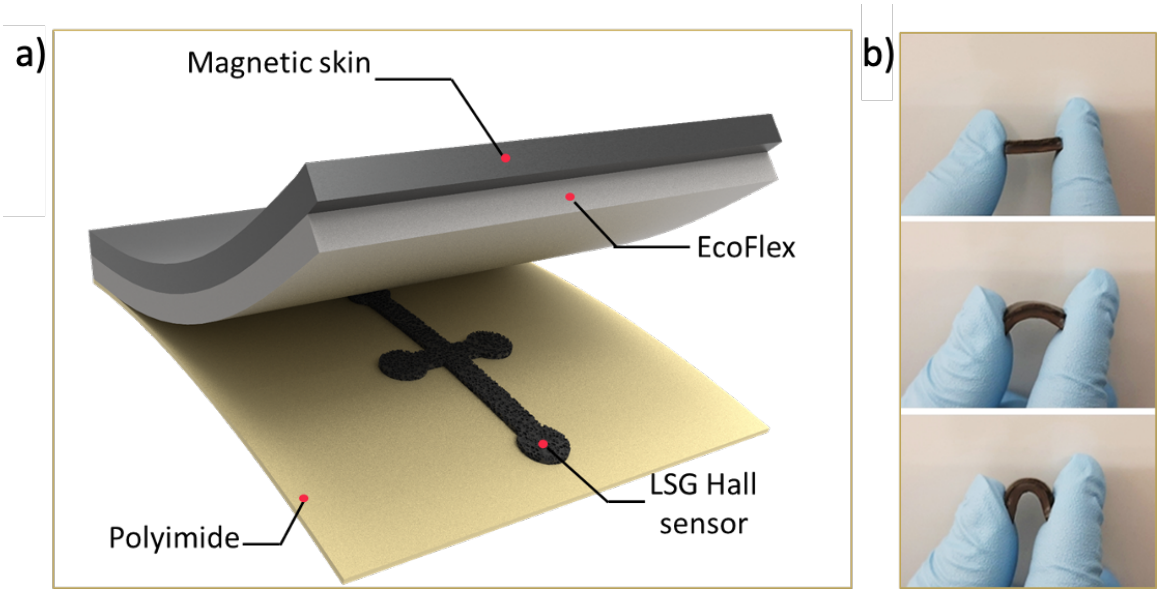

Figure 8.5 - a) Assembly of a flexible LSG tactile sensor. b) Optical photograph of the tactile sensor demonstrating its flexibility.

ultra-flexible magnet (thickness: 0.17 mm) composed of the same silicon-based elastomer matrix (Ecoflex, Smooth-on) and permanent magnetic particles (NdFeB, MQP-16-7FP).

The detailed fabrication process of the composite magnet was reported in [274]. In brief, the composite was prepared by mixing the Ecoflex (50 wt%) and the NdFeB powder (50 wt%) and molding. After curing, the magnetic composite was magnetized in the out-of-plane direction with a 1.8 T magnetic field (Figure 8.11). Figure 8.12 depicts the effect of NdFeB particle concentration on the modulus of elasticity and residual magnetization of magnetic skin. It's worth noting that raising the filler concentration leads in a stiffer material with more residual magnetism

The magnetic field distribution in the near magnet region (Figure 8.13) was characterized using the 3-axes magnetic field mapper shown in Figure 8.14. It consists of

a 3-axes robotic arm, with stepper motors actuating each axis, and a 3-axes Magneto Impedance sensor (BM1422AGV, Rohm). Only the *z* – component, B_z, of the magnetic

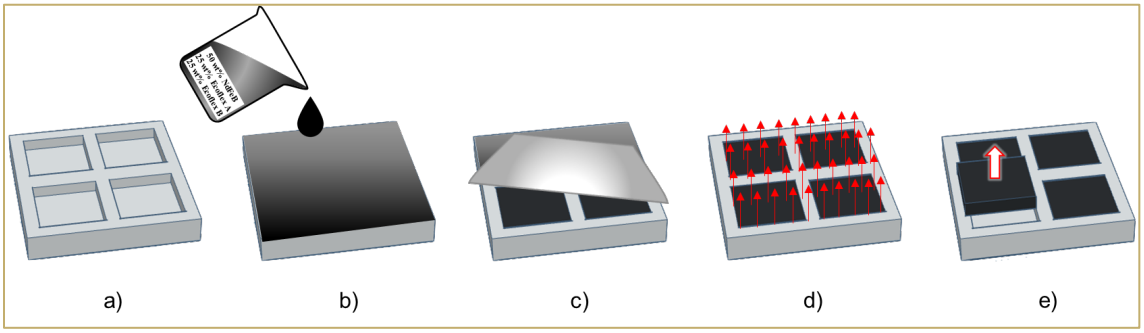

Figure 8.11 - The magnetic skin is achieved by a) 3D printing mold with the desired shape, b) mixing the silicon-based elastomer matrix with the magnetic powder, c) planarizing the mixture into the mold, d) magnetizing the magnetic skin by applying an external magnetic field of 1.8T, and finally, e)releasing the magnetic skin.

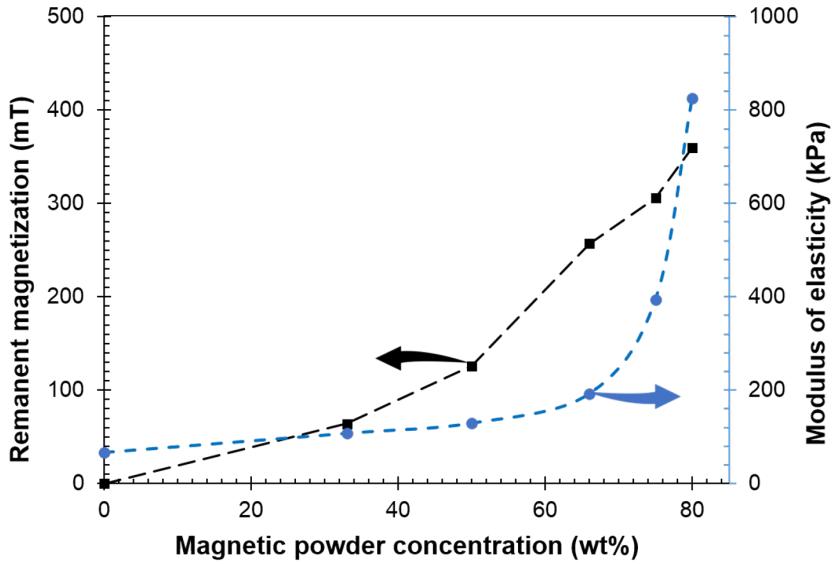

Figure 8.12 - Physical characterization of magnetic skin.

the field was measured (averaged over 30 measurement samples) at a distance of 10 mm above the magnet across the *xy* -plane, scanning with a step size of 500 µm. The geomagnetic field, measured at 20.78 µT before the sampling process, was removed from the measured magnetic field data. Figure 8.13 shows the magnetic field distribution for

a sampling area of 25 mm x 25 mm, totalling 50 sample points in both the *x* and *y* directions. The strength of the *z* component of the magnetic field, B_z, reaches 300 µT at the centre of symmetry (x = 12.5 mm, y = 12.5 mm, z = 10 mm) and diminishes with increasing distance from the center of the magnet in the *xy*-plane. The tactile sensor was then examined by applying a normal force up to 8N with a square-shaped load (1 x 1 cm) in an electromechanical tester. The force was applied to the center of the square-shaped sensor. The LSG Hall sensor was operated by applying a current of 100 µA, and the Hall voltage was measured using a multimeter (Agilent, U1272A).

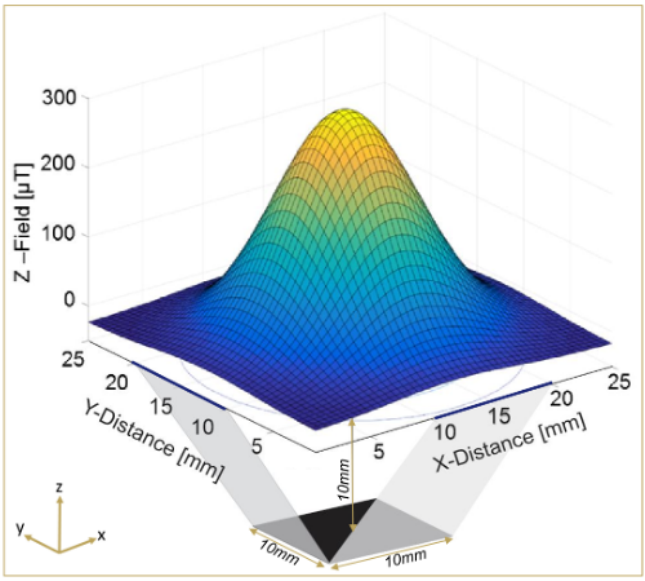

Figure 8.13 - a 3D surface plot of the z component of the magnetic field on the xy-plane at z = 10 mm above the magnet.

The response of the sensor in Figure 8.16 shows a linear increase of the Hall voltage with the applied force. An average sensitivity of 0.034 mV/N and a standard deviation of σ ± 0.002 N have been deduced from the obtained results. It should be noted that the sensitivity can be tailored and further optimized by the mass ratio of the NdFeB powder,

the stiffness of the elastomer, as well as the device dimensions, in particular the thickness of the elastomer.

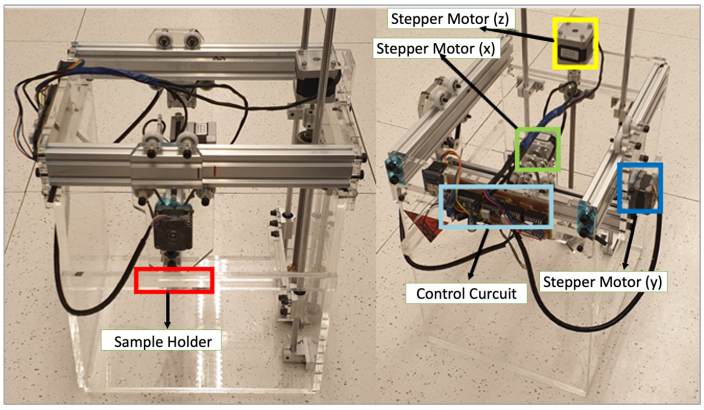

Figure 8. 6 - Measurement system for stimulation magnetic field properties of a flexible magnet.

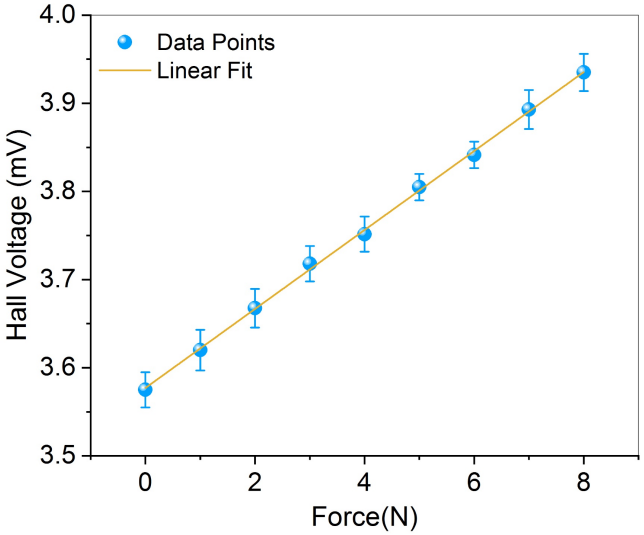

Figure 8.7 - The average output voltage of five measurements of a soft tactile sensor as a result of consecutive linear loading cycles. The error bars indicate the standard deviation.

8.7 Summary

A flexible, versatile, and robust graphene Hall sensor was realized with a facile, one-step fabrication process. The laser scribing approach has shown promise for widespread deployment of flexible graphene Hall sensors, particularly in hostile environments. The

LSG Hall sensors demonstrated no degradation after being bent to a minimum radius of 5 mm, corresponding to 1.6 % tensile strain, and after 1000 bending cycles, while having a linear response to magnetic fields and a normalized sensitivity of 1.12 V/AT. The sensor can withstand temperatures of up to 400 degrees Celsius. Up to a corner frequency of 17.6 Hz, flicker noise dominates the noise signal, followed by a low constant noise voltage floor of 50 nV/$\sqrt{\text{Hz}}$, corresponding to a magnetic resolution of 0.446 mT/$\sqrt{\text{Hz}}$. The LSG Hall sensor was incorporated into a magnetic field-based soft and flexible tactile sensor, which offers a linear response to the applied force with a sensitivity of 0.034 mV/N. It could be easily tailored further through optimization of fabrication process.

Chapter 9

Concluding Remarks

9.1 Conclusion

This work utilized a one-step laser scribing process to lower technological barriers and bring more widespread adoption of graphene. LSG was used as a versatile and multifunctional material to display physical coupling in several domains without the involvement of costly multi-step fabrication processes, chemical treatments, and synthesis. An array of wearable and robust graphene sensors were developed for low-cost measurements of various physical parameters, such as flow, strain, curvature, deflection, force, temperature, conductivity, pressure, and magnetic field. The sensitivity and dynamic range of the sensors were tailored using their geometries, laser parameters, and various designs. Methods to enhance the electromechanical performance of LSG sensors and to achieve a homogeneous bidirectional bending with temperature compensation were developed.

A double-sided electrode concept provided increased and homogeneous bidirectional response and full temperature compensation. A gauge factor of 91.2 is achieved after three-times laser writing at low power, which is an increase of 750% to one-time laser writing and 720% higher than the ones previously reported for LSG strain sensors. The pressure sensor offers a sensitivity of 1.23×10^{-3} kPa, and detection limit of 10 Pa combined with an extremely broad dynamic range of at least 20 MPa. Moreover, it provides outstanding stability of at least 15 000 bending cycles. A two-electrode cell is

used to measure the impedance, and thereby the conductivity, of the water in the MHz frequency range. It offers an accuracy of ±0.5 psu, which is not affected by sensor deformation. While biofouling is strongly affecting commonly employed low frequency conductivity measurements, in the MHz frequency range, it acts like a short-circuited capacitance. Biofouling independent salinity sensing can be achieved using a two-electrode impedance measurement at a frequency of 1 MHz. At low frequencies (10 kHz–100 kHz), a four-electrode conductivity cell has a linear response to salinity and a high sensitivity of 0.85 mS/psu. These characteristics considerably relax the requirements for the circuit of the data logger. The LSG Hall sensor offers a linear response to magnetic fields with a normalized sensitivity of ~1.12 V/AT. It also exhibits a low constant noise voltage floor of ~ 50 nV/Hz for a bias current of 100 µA at room temperature, which is comparable with state-of-the-art low-noise Hall sensors. The sensors combine a high bendability, come with high robustness and operating temperatures from -33.15 °C to 400 °C.

The scope of LSG electrode applications has benefitted from its ability to withstand harsh environmental conditions, such as high pressure, temperature, salinity, and bending conditions. Due to its advantageous characteristics, such as low cytotoxicity, biocompatibility, corrosion resistance, the LSG sensors are a prime choice for multiple healthcare, underwater, and robotics applications. Wearable and multifunctional LSG sensors provided new opportunities for analyzing humans and animals motion and mobility, microsleep detection, heart rate monitoring on the radial artery, plantar pressure measurements, and tactile sensing. Another promising application was

concerned with externally worn robotic hardware for tactile sensing and UAV speed monitoring. The developed sensors could easily be integrated with custom-made PCB assembly and miniaturized data-loggers to monitor the velocity of underwater currents, conductivity, temperature, and pressure at a depth of 2 km in seawater. The LSG sensor platform could also accommodate less intrusive attachment to the curved surfaces of marine animals and integration of the sensor on CTD devices for small-sized marine animals while advancing scientific exploration. LSG sensors enabled device concepts in soft robotics, as LSG Hall sensor was combined with a deformable elastomer and flexible magnet to realize low-cost, compliant, and customizable tactile sensors.

9.2 Outlook

Despite the fact that numerous LSG-based physical sensors have demonstrated their feasibility and reliability, there are still a number of obstacles to overcome. Table 9.1 provides a description of these difficulties as well as some potential solutions. To reach the mainstream market, the LSG technology must provide a path to high-throughput, low-cost production. The laser scan rate, in particular, should be increased without losing LSG characteristics while preserving acceptable part-to-part tolerance. CO2 lasers with speeds ranging from 2 to 6 m/min are used to create 3D porous graphene, as shown in Figure 2.7. Although this laser provides a faster route to prepare graphene than conventional CVD and exfoliation processes, the scribing rate is insufficient to compete with the production of some alternative conductive materials, such as copper, aluminum, and silver. These materials can be currently roll-to-roll stamped out on a machine that runs at

up to 30m/min, producing 250,000 units per hour[278]. Conductive metals could also be produced with flex printers that run at 40 m/min, however curing durations slow the yield. The incumbent metal foil strain gauge technology, for example, is the major competition for the LSG strain sensor. The biggest barrier to LSG strain sensor commercialization is that the incumbent is a simple, well-established, and low-cost technology. The LSG process, on the other hand, is suitable for roll-to-roll manufacturing, allowing for future scale-up production.

The requirement to improve the packing density, or the number of devices printed per unit area, is another issue for direct lasing technology. LSG's minimum known spatial resolution (~12 μm) is micro-scale and similar to several printed electronics approaches; yet, it is insufficient for downsized and compact sensors. As a result, future research efforts should focus on achieving a narrower line width at the nanoscale scale. Fabrication of vertical graphene designs should also be looked at in order to boost LSG density in a given footprint area for better areal performance metrics. Because LSG can respond to several physical stimuli at the same time, distinguishing the type and strength of each stimulus could be challenging. To eliminate interference between various stimuli for specific end applications, specialized sensing devices with low cross-sensitivity and appropriate decoupling algorithms are required. Because of the mismatch in mechanical, thermal, and electrical characteristics, integrating LSG transducers with other flexible electronics could be difficult. To maintain structural integrity while supplying power and data in a steady manner, multilevel connectors such as stretchy conductors would be necessary. The study of information processing in conjunction with LSG sensors is an

intriguing research topic that could lead to a variety of cutting-edge applications, including artificial intelligence, intelligent robotics, and medical and healthcare assessments.

Table 9.1 - Challenges and potential solutions to enable further development of LSG physical sensors.

	Challenges	Potential solutions
Fabrication	Slow printing process	Parallel processing strategies, including the adoption of spatial light modulators, holographic laser processing, multilayer beams, and/or patterned light field to be developed. A major leap forward can be expected by implementing roll-to-roll fabrication to increase the yield, like in many printing technologies.
	Limited resolution	Alternative lasers with smaller focal spot sizes are needed to achieve high spatial resolution. The possibilities of femtosecond - laser direct writing and vertical LSG architectures are attractive options for future investigations.
	Flexible-rigid readout interface	Multilevel interconnections such as stretchable conductors would be required to preserve structural integrity while delivering power and data in a stable manner. Integration technologies that are utilized in and developed for hybrid electronics could be adopted for LSG electrodes.
Performance	Cross-sensitivity	Effective decoupling algorithms should be realized to avoid interference between the multiple stimuli for specific applications.
	Motion induced noise	Mechanical noise could be reduced by using a redundant sensor while applying algorithms to pick up the real signals from noise.
Applications	Sensor-human interface	Benefitting from the low cytotoxicity and biocompatibility of LSG, LSG physical sensors could be tested on patients as part of clinical trials. The comfortability and compliance of sensors need to be systematically assessed.
	Underwater monitoring	A protective coating has to be applied to avoid interference with the measurement due to shunt currents. The coating should not compromise the electrical properties of the LSG and the part-to-part tolerance.
	Internet of things (smart home, city, grids, etc.)	Effective IoT connectivity protocols should be selected to provide a trade-off between power and bandwidth consumption. The reliability of LSG physical sensors could then be evaluated in crowded, noisy, and more complex environments.

BIBLIOGRAPHY

1. Popkova, E.G., Y.V. Ragulina, and A.V. Bogoviz, *Fundamental differences of transition to industry 4.0 from previous industrial revolutions*, in *Industry 4.0: Industrial Revolution of the 21st Century*. 2019, Springer. p. 21-29.
2. Baheti, R. and H. Gill, *Cyber-physical systems.* The impact of control technology, 2011. **12**(1): p. 161-166.
3. Jazdi, N. *Cyber physical systems in the context of Industry 4.0*. in *2014 IEEE international conference on automation, quality and testing, robotics*. 2014. IEEE.
4. Rajkumar, R., et al. *Cyber-physical systems: the next computing revolution*. in *Design automation conference*. 2010. IEEE.
5. Wu, F.-J., Y.-F. Kao, and Y.-C. Tseng, *From wireless sensor networks towards cyber physical systems.* Pervasive and Mobile computing, 2011. **7**(4): p. 397-413.
6. Lenka, R.K., et al., *Building scalable cyber-physical-social networking infrastructure using IoT and low power sensors.* IEEE Access, 2018. **6**: p. 30162-30173.
7. Alexandre, R. and O. Postolache. *Wearable and IoT technologies application for physical rehabilitation*. in *2018 International symposium in sensing and instrumentation in IoT era (ISSI)*. 2018. IEEE.
8. Kabadayi, S., A. Pridgen, and C. Julien. *Virtual sensors: Abstracting data from physical sensors*. in *2006 International Symposium on a World of Wireless, Mobile and Multimedia Networks (WoWMoM'06)*. 2006. IEEE.
9. Bogue, R., *Towards the trillion sensors market.* Sensor review, 2014.

10. Bryzek, J., *Roadmap for the trillion sensor universe.* Berkeley, CA, April, 2013. **2**.

11. Sony, S., S. Laventure, and A. Sadhu, *A literature review of next-generation smart sensing technology in structural health monitoring.* Structural Control and Health Monitoring, 2019. **26**(3): p. e2321.

12. Sezen, B. and S.Y. Cankaya, *Effects of green manufacturing and eco-innovation on sustainability performance.* Procedia-Social and Behavioral Sciences, 2013. **99**: p. 154-163.

13. Tsoulfas, G.T. and C.P. Pappis, *Environmental principles applicable to supply chains design and operation.* Journal of Cleaner Production, 2006. **14**(18): p. 1593-1602.

14. Rao, P. and D. Holt, *Do green supply chains lead to competitiveness and economic performance?* International journal of operations & production management, 2005.

15. Fuller, D., et al., *Reliability and validity of commercially available wearable devices for measuring steps, energy expenditure, and heart rate: systematic review.* JMIR mHealth and uHealth, 2020. **8**(9): p. e18694.

16. Senesky, D.G., et al., *Harsh environment silicon carbide sensors for health and performance monitoring of aerospace systems: A review.* IEEE Sensors Journal, 2009. **9**(11): p. 1472-1478.

17. Werner, M.R. and W.R. Fahrner, *Review on materials, microsensors, systems and devices for high-temperature and harsh-environment applications.* IEEE Transactions on Industrial Electronics, 2001. **48**(2): p. 249-257.

18. Moghadam, F.P., M.S. Bajgiran, and S. Aghaee, *A Survey on Big Data usage in the Internet of Things.*

19. Calautit, K., D.S. Nasir, and B.R. Hughes, *Low power energy harvesting systems: State of the art and future challenges.* Renewable and Sustainable Energy Reviews, 2021. **147**: p. 111230.

20. Sandeep Kumar, V. and A. Venkatesh, *Advances in graphene-based sensors and devices.* J. Nanomed. Nanotechol, 2013. **4**: p. e127.

21. Zhang, Z., et al., *Top-down bottom-up graphene synthesis.* Nano Futures, 2019. **3**(4): p. 042003.

22. Munoz, R. and C. Gómez-Aleixandre, *Review of CVD synthesis of graphene.* Chemical Vapor Deposition, 2013. **19**(10-11-12): p. 297-322.

23. Tour, J.M., *Top-down versus bottom-up fabrication of graphene-based electronics.* Chemistry of Materials, 2014. **26**(1): p. 163-171.

24. Kaidarova, A. and J. Kosel, *Physical Sensors Based on Laser-Induced Graphene: A Review.* IEEE Sensors Journal, 2020.

25. Li, J., V. Mishukova, and M. Östling, *All-solid-state micro-supercapacitors based on inkjet printed graphene electrodes.* Applied Physics Letters, 2016. **109**(12): p. 123901.

26. Randviir, E.P., et al., *The fabrication, characterisation and electrochemical investigation of screen-printed graphene electrodes.* Physical Chemistry Chemical Physics, 2014. **16**(10): p. 4598-4611.

27. Tran, T.S., N.K. Dutta, and N.R. Choudhury, *Graphene inks for printed flexible electronics: graphene dispersions, ink formulations, printing techniques and applications.* Advances in colloid and interface science, 2018. **261**: p. 41-61.

28. Blayo, A. and B. Pineaux. *Printing processes and their potential for RFID printing*. in *Proceedings of the 2005 joint conference on Smart objects and ambient intelligence: innovative context-aware services: usages and technologies*. 2005.

29. Han, X., et al., *Scalable, printable, surfactant-free graphene ink directly from graphite.* Nanotechnology, 2013. **24**(20): p. 205304.

30. Sinar, D. and G.K. Knopf, *Cyclic liquid-phase exfoliation of electrically conductive graphene-derivative inks.* IEEE Transactions on Nanotechnology, 2018. **17**(5): p. 1020-1028.

31. Xu, Y., et al., *Liquid-phase exfoliation of graphene: an overview on exfoliation media, techniques, and challenges.* Nanomaterials, 2018. **8**(11): p. 942.

32. Xu, L., et al., *Ag–graphene hybrid conductive ink for writing electronics.* Nanotechnology, 2014. **25**(5): p. 055201.

33. Liu, Z., et al., *Transparent conductive electrodes from graphene/PEDOT: PSS hybrid inks for ultrathin organic photodetectors.* Advanced Materials, 2015. **27**(4): p. 669-675.

34. Kim, Y.D. and J. Hone, *Screen printing of 2D semiconductors.* Nature, 2017. **544**(7649): p. 167-168.

35. Arapov, K., et al., *Conductive screen printing inks by gelation of graphene dispersions.* Advanced Functional Materials, 2016. **26**(4): p. 586-593.

36. Lin, M., et al., *Preparation of pristine graphene paste for screen printing patterns with high conductivity.* Chemical Physics Letters, 2018. **713**: p. 98-104.

37. Arapov, K., et al., *Conductivity Enhancement of Binder-Based Graphene Inks by Photonic Annealing and Subsequent Compression Rolling.* Advanced Engineering Materials, 2016. **18**(7): p. 1234-1239.

38. Secor, E.B., et al., *Gravure printing of graphene for large-area flexible electronics.* Advanced materials, 2014. **26**(26): p. 4533-4538.

39. Secor, E.B. and M.C. Hersam, *Graphene inks for printed electronics.* Evanston, USA, 2015.

40. Singh, M., et al., *Inkjet printing—process and its applications.* Advanced materials, 2010. **22**(6): p. 673-685.

41. Shin, K.Y., J.Y. Hong, and J. Jang, *Micropatterning of graphene sheets by inkjet printing and its wideband dipole-antenna application.* Advanced materials, 2011. **23**(18): p. 2113-2118.

42. Li, J., et al., *Efficient inkjet printing of graphene.* Advanced materials, 2013. **25**(29): p. 3985-3992.

43. Torrisi, F., et al., *Inkjet-printed graphene electronics.* ACS nano, 2012. **6**(4): p. 2992-3006.

44. Kamyshny, A. and S. Magdassi, *Conductive nanomaterials for printed electronics.* Small, 2014. **10**(17): p. 3515-3535.

45. Costa, J.C., et al., *Flexible sensors—from materials to applications.* Technologies, 2019. **7**(2): p. 35.

46. Kalantar-Zadeh, K., et al., *Emergence of liquid metals in nanotechnology.* ACS nano, 2019. **13**(7): p. 7388-7395.

47. Yang, J., W. Cheng, and K. Kalantar-Zadeh, *Electronic skins based on liquid metals.* Proceedings of the IEEE, 2019. **107**(10): p. 2168-2184.

48. Fan, B., et al., *Sputtered porous Pt for wafer-scale manufacture of low-impedance flexible microelectrodes.* Journal of Neural Engineering, 2020. **17**(3): p. 036029.

49. Le, N.N., et al., *Optimization of copper electroplating process applied for microfabrication on flexible polyethylene terephthalate substrate.* Advances in Natural Sciences: Nanoscience and Nanotechnology, 2015. **6**(3): p. 035007.

50. Yu, Y., C. Yan, and Z. Zheng, *Polymer-Assisted Metal Deposition (PAMD): A Full-Solution Strategy for Flexible, Stretchable, Compressible, and Wearable Metal Conductors.* Advanced Materials, 2014. **26**(31): p. 5508-5516.

51. Wahl, T., J. Hanisch, and E. Ahlswede, *Comparison of the Al back contact deposited by sputtering, e-beam, or thermal evaporation for inverted perovskite solar cells.* Journal of Physics D: Applied Physics, 2018. **51**(13): p. 135502.

52. Alrammouz, R., et al., *A review on flexible gas sensors: From materials to devices.* Sensors and Actuators A: Physical, 2018. **284**: p. 209-231.

53. Liu, Z., et al., *Flexible electronics based on inorganic nanowires.* Chemical Society Reviews, 2015. **44**(1): p. 161-192.

54. Segev-Bar, M. and H. Haick, *Flexible sensors based on nanoparticles.* ACS nano, 2013. **7**(10): p. 8366-8378.

55. Shengbo, S., et al., *Highly sensitive wearable strain sensor based on silver nanowires and nanoparticles.* Nanotechnology, 2018. **29**(25): p. 255202.

56. Hobbs, R.G., N. Petkov, and J.D. Holmes, *Semiconductor nanowire fabrication by bottom-up and top-down paradigms.* Chemistry of Materials, 2012. **24**(11): p. 1975-1991.

57. Han, S.T., et al., *An overview of the development of flexible sensors.* Advanced materials, 2017. **29**(33): p. 1700375.

58. Burghard, M., H. Klauk, and K. Kern, *Carbon-based field-effect transistors for nanoelectronics.* Advanced Materials, 2009. **21**(25-26): p. 2586-2600.

59. Zhang, L., et al., *Advanced nanostructured carbon-based materials for rechargeable lithium-sulfur batteries.* Carbon, 2019. **141**: p. 400-416.

60. Angione, M.D., et al., *Carbon based materials for electronic bio-sensing.* Materials today, 2011. **14**(9): p. 424-433.

61. Li, S., et al., *Recent advances of carbon-based flexible strain sensors in physiological signal monitoring.* ACS Applied Electronic Materials, 2020. **2**(8): p. 2282-2300.

62. Nag, A., et al., *Multi-Walled Carbon Nanotubes-Based Sensors for Strain Sensing Applications.* Sensors, 2021. **21**(4): p. 1261.

63. Prasek, J., et al., *Methods for carbon nanotubes synthesis.* Journal of Materials Chemistry, 2011. **21**(40): p. 15872-15884.

64. See, C.H. and A.T. Harris, *A review of carbon nanotube synthesis via fluidized-bed chemical vapor deposition.* Industrial & engineering chemistry research, 2007. **46**(4): p. 997-1012.

65. Kranz, L., et al., *Doping of polycrystalline CdTe for high-efficiency solar cells on flexible metal foil.* Nature communications, 2013. **4**(1): p. 1-7.

66. Macrelli, G., A.K. Varshneya, and J.C. Mauro, *Ultra-thin glass as a substrate for flexible photonics.* Optical Materials, 2020. **106**: p. 109994.

67. Gupta, S., et al., *Ultra-thin chips for high-performance flexible electronics.* npj Flexible Electronics, 2018. **2**(1): p. 1-17.

68. Amara, S., et al., *High-Performance Flexible Magnetic Tunnel Junctions for Smart Miniaturized Instruments.* Advanced Engineering Materials, 2018. **20**(10): p. 1800471.

69. Garner, S., S. Glaesemann, and X. Li, *Ultra-slim flexible glass for roll-to-roll electronic device fabrication.* Applied Physics A, 2014. **116**(2): p. 403-407.

70. Eder, F., et al., *Organic electronics on paper.* Applied Physics Letters, 2004. **84**(14): p. 2673-2675.

71. Rubehn, B. and T. Stieglitz, *In vitro evaluation of the long-term stability of polyimide as a material for neural implants.* Biomaterials, 2010. **31**(13): p. 3449-3458.

72. Bauer, C. and R. Farris, *Determination of poisson's ratio for polyimide films.* Polymer Engineering & Science, 1989. **29**(16): p. 1107-1110.

73. Goitisolo, I., J.I. Eguiazábal, and J. Nazábal, *Effects of reprocessing on the structure and properties of polyamide 6 nanocomposites.* Polymer Degradation and Stability, 2008. **93**(10): p. 1747-1752.

74. Nishino, T., et al., *In situ observation of surface deformation of polymer films by atomic force microscopy.* Review of Scientific Instruments, 2000. **71**(5): p. 2094-2096.

75. Maddipatla, D., B.B. Narakathu, and M. Atashbar, *Recent Progress in Manufacturing Techniques of Printed and Flexible Sensors: A Review.* Biosensors, 2020. **10**(12): p. 199.

76. Xie, Z., et al., *Polymer Pen Lithography Using Dual-Elastomer Tip Arrays.* Small, 2012. **8**(17): p. 2664-2669.

77. Li, D., et al., *Printable transparent conductive films for flexible electronics.* Advanced Materials, 2018. **30**(10): p. 1704738.

78. Mata, A., A.J. Fleischman, and S. Roy, *Characterization of polydimethylsiloxane (PDMS) properties for biomedical micro/nanosystems.* Biomedical microdevices, 2005. **7**(4): p. 281-293.

79. Vashisth, A., et al., *ReaxFF Simulations of Laser-Induced Graphene (LIG) Formation for Multifunctional Polymer Nanocomposites.* ACS Applied Nano Materials, 2020. **3**(2): p. 1881-1890.

80. Ye, R., D.K. James, and J.M. Tour, *Laser-induced graphene.* Accounts of chemical research, 2018. **51**(7): p. 1609-1620.

81. Sha, Y., et al., *Laser induced graphitization of PAN-based carbon fibers.* RSC advances, 2018. **8**(21): p. 11543-11550.

82. Carvalho, A.F., et al., *Laser-induced graphene strain sensors produced by ultraviolet irradiation of polyimide.* Advanced Functional Materials, 2018. **28**(52): p. 1805271.

83. Zhang, Z., et al., *Visible light laser-induced graphene from phenolic resin: A new approach for directly writing graphene-based electrochemical devices on various substrates.* Carbon, 2018. **127**: p. 287-296.

84. Li, G., W.-C. Law, and K.C. Chan, *Floating, highly efficient, and scalable graphene membranes for seawater desalination using solar energy.* Green Chemistry, 2018. **20**(16): p. 3689-3695.

85. Li, Y., et al., *Laser-Induced Graphene in Controlled Atmospheres: From Superhydrophilic to Superhydrophobic Surfaces.* Advanced Materials, 2017. **29**(27): p. 1700496.

86. Cai, J., C. Lv, and A. Watanabe, *Laser direct writing of high-performance flexible all-solid-state carbon micro-supercapacitors for an on-chip self-powered photodetection system.* Nano Energy, 2016. **30**: p. 790-800.

87. Nasser, J., et al., *Laser induced graphene fibers for multifunctional aramid fiber reinforced composite.* Carbon, 2020. **158**: p. 146-156.

88. Lamberti, A., et al., *New insights on laser-induced graphene electrodes for flexible supercapacitors: tunable morphology and physical properties.* Nanotechnology, 2017. **28**(17): p. 174002.

89. Duy, L.X., et al., *Laser-induced graphene fibers.* Carbon, 2018. **126**: p. 472-479.

90. Cardoso, A.R., et al., *Molecularly-imprinted chloramphenicol sensor with laser-induced graphene electrodes.* Biosensors and Bioelectronics, 2019. **124**: p. 167-175.

91. Beduk, T., et al., *One-step electrosynthesized molecularly imprinted polymer on laser scribed graphene bisphenol a sensor.* Sensors and Actuators B: Chemical, 2020: p. 128026.

92. Wang, F., et al., *Laser-induced graphene: preparation, functionalization and applications.* Materials technology, 2018. **33**(5): p. 340-356.

93. Zhang, Y., et al., *A flexible non-enzymatic glucose sensor based on copper nanoparticles anchored on laser-induced graphene.* Carbon, 2020. **156**: p. 506-513.

94. Yang, Y., et al., *A laser-engraved wearable sensor for sensitive detection of uric acid and tyrosine in sweat.* Nature Biotechnology, 2020. **38**(2): p. 217-224.

95. Hui, X., et al., *A highly flexible and selective dopamine sensor based on Pt-Au nanoparticle-modified laser-induced graphene.* Electrochimica Acta, 2019. **328**: p. 135066.

96. Fenzl, C., et al., *Laser-scribed graphene electrodes for aptamer-based biosensing.* ACS sensors, 2017. **2**(5): p. 616-620.

97. Ye, R., D.K. James, and J.M. Tour, *Laser-induced graphene: from discovery to translation.* Advanced Materials, 2019. **31**(1): p. 1803621.

98. Li, G., *Direct laser writing of graphene electrodes.* Journal of Applied Physics, 2020. **127**(1): p. 010901.

99. Kurra, N., et al., *Laser-derived graphene: a three-dimensional printed graphene electrode and its emerging applications.* Nano Today, 2019. **24**: p. 81-102.

100. Thamaraiselvan, C., et al., *Laser-induced graphene and carbon nanotubes as conductive carbon-based materials in environmental technology.* Materials Today, 2019.

101. Li, L., et al., *High-performance pseudocapacitive microsupercapacitors from laser-induced graphene.* Advanced Materials, 2016. **28**(5): p. 838-845.

102. Ren, M., J. Zhang, and J.M. Tour, *Laser-induced graphene synthesis of Co3O4 in graphene for oxygen electrocatalysis and metal-air batteries.* Carbon, 2018. **139**: p. 880-887.

103. Yoon, H., et al., *A chemically modified laser-induced porous graphene based flexible and ultrasensitive electrochemical biosensor for sweat glucose detection.* Sensors and Actuators B: Chemical, 2020. **311**: p. 127866.

104. Cai, J., et al., *Laser direct writing of heteroatom-doped porous carbon for high-performance micro-supercapacitors.* Energy Storage Materials, 2020. **25**: p. 404-415.

105. Wang, F., et al., *Laser-induced nitrogen-doped hierarchically porous graphene for advanced electrochemical energy storage.* Carbon, 2019. **150**: p. 396-407.

106. Basu, A., et al., *CO2 laser direct written MOF-based metal-decorated and heteroatom-doped porous graphene for flexible all-solid-state*

microsupercapacitor with extremely high cycling stability. ACS Applied Materials & Interfaces, 2016. **8**(46): p. 31841-31848.

107. Zhang, C., et al., *Monolithic and flexible ZnS/SnO2 ultraviolet photodetectors with lateral graphene electrodes.* Small, 2017. **13**(18): p. 1604197.

108. Ge, L., et al., *A laser-induced TiO 2-decorated graphene photoelectrode for sensitive photoelectrochemical biosensing.* Chemical Communications, 2019. **55**(34): p. 4945-4948.

109. Yagati, A.K., et al., *Laser-induced graphene interdigitated electrodes for label-free or nanolabel-enhanced highly sensitive capacitive aptamer-based biosensors.* Biosensors and Bioelectronics, 2020: p. 112272.

110. Zhu, J., et al., *Biomimetic turbinate-like artificial nose for hydrogen detection based on 3D porous laser-induced graphene.* ACS applied materials & interfaces, 2019. **11**(27): p. 24386-24394.

111. You, R., et al., *Laser fabrication of graphene-based flexible electronics.* Advanced Materials, 2020. **32**(15): p. 1901981.

112. Liu, Y.-Q., et al., *Laser fabrication of graphene-based electronic skin.* Frontiers in chemistry, 2019. **7**: p. 461.

113. Kumar, R., et al., *Laser-assisted synthesis, reduction and micro-patterning of graphene: recent progress and applications.* Coordination Chemistry Reviews, 2017. **342**: p. 34-79.

114. Wan, Z., et al., *Laser-Reduced Graphene: Synthesis, Properties, and Applications.* Advanced Materials Technologies, 2018. **3**(4): p. 1700315.

115. Tao, L.-Q., et al., *An intelligent artificial throat with sound-sensing ability based on laser induced graphene.* Nature communications, 2017. **8**(1): p. 1-8.

116. Luo, S., P.T. Hoang, and T. Liu, *Direct laser writing for creating porous graphitic structures and their use for flexible and highly sensitive sensor and sensor arrays.* Carbon, 2016. **96**: p. 522-531.

117. Rahimi, R., et al., *Highly stretchable and sensitive unidirectional strain sensor via laser carbonization.* ACS applied materials & interfaces, 2015. **7**(8): p. 4463-4470.

118. Biswas, R.K., et al., *Improved conductivity of carbonized polyimide by CO 2 laser graphitization.* Journal of Materials Chemistry C, 2020. **8**(13): p. 4493-4501.

119. Lin, J., et al., *Laser-induced porous graphene films from commercial polymers.* Nature communications, 2014. **5**(1): p. 1-8.

120. Huang, Y., et al., *Laser Direct Writing of Heteroatom (N and S)-Doped Graphene from a Polybenzimidazole Ink Donor on Polyethylene Terephthalate Polymer and Glass Substrates.* Small, 2018. **14**(44): p. 1803143.

121. Zhu, C., et al., *Direct laser writing of graphene films from a polyether ether ketone precursor.* Journal of Materials Science, 2019. **54**(5): p. 4192-4201.

122. Lamberti, A., et al., *A highly stretchable supercapacitor using laser-induced graphene electrodes onto elastomeric substrate.* Advanced Energy Materials, 2016. **6**(10): p. 1600050.

123. Yazdi, A.Z., et al., *Direct Creation of Highly Conductive Laser-Induced Graphene Nanocomposites from Polymer Blends.* Macromolecular Rapid Communications, 2017. **38**(17): p. 1700176.

124. Wahab, H., et al., *Machine-learning-assisted fabrication: Bayesian optimization of laser-induced graphene patterning using in-situ Raman analysis.* Carbon, 2020. **167**: p. 609-619.

125. Ferrari, A.C., et al., *Raman spectrum of graphene and graphene layers.* Physical review letters, 2006. **97**(18): p. 187401.

126. Dong, H., S. Guo, and L. Zhao, *Facile Preparation of Multilayered Graphene with CO2 as a Carbon Source.* Applied Sciences, 2019. **9**(21): p. 4482.

127. Tittle, C.M., et al., *Robust superhydrophobic laser-induced graphene for desalination applications.* Advanced Materials Technologies, 2018. **3**(2): p. 1700207.

128. Behrent, A., et al., *Process-property correlations in laser-induced graphene electrodes for electrochemical sensing.* Microchimica Acta, 2021. **188**(5): p. 1-14.

129. Wu, Y., et al., *Piezoresistive stretchable strain sensors with human machine interface demonstrations.* Sensors and Actuators A: Physical, 2018. **279**: p. 46-52.

130. Stanford, M.G., et al., *Laser-induced graphene for flexible and embeddable gas sensors.* ACS nano, 2019. **13**(3): p. 3474-3482.

131. Murray, R., et al., *Design of Experiments and Optimization of Laser-Induced Graphene.* ACS Omega, 2021.

132. Tiliakos, A., et al., *Morphic transitions of nanocarbons via laser pyrolysis of polyimide films.* Journal of Analytical and Applied Pyrolysis, 2016. **121**: p. 275-286.

133. Vivaldi, F.M., et al., *Three-dimensional (3D) laser-induced graphene: structure, properties, and application to chemical sensing.* ACS Applied Materials & Interfaces, 2021. **13**(26): p. 30245-30260.

134. Stanford, M.G., et al., *Laser-induced graphene triboelectric nanogenerators.* ACS nano, 2019. **13**(6): p. 7166-7174.

135. Singh, E., et al., *Superhydrophobic graphene foams.* small, 2013. **9**(1): p. 75-80.

136. Khan, M.A., et al., *Magnetic Composite Hydrodynamic Pump With Laser-Induced Graphene Electrodes.* IEEE Transactions on Magnetics, 2017. **53**(11): p. 1-4.

137. Gerringer, J.C., et al., *Radio Frequency Heating of Laser-Induced Graphene on Polymer Surfaces for Rapid Welding.* ACS Applied Nano Materials, 2019. **2**(11): p. 7032-7042.

138. Han, T., et al., *Multifunctional flexible sensor based on laser-induced graphene.* Sensors, 2019. **19**(16): p. 3477.

139. Ye, R., et al., *Laser-induced graphene formation on wood.* Advanced Materials, 2017. **29**(37): p. 1702211.

140. Zhu, J., et al., *Cost-effective fabrication and high-frequency response of non-ideal RC application based on 3D porous laser-induced graphene.* Journal of Materials Science, 2018. **53**(17): p. 12413-12420.

141. Zhang, P., et al., *Flexible laser-induced-graphene omnidirectional sound device.* Chemical Physics Letters, 2020. **745**: p. 137275.

142. Chen, Y., et al., *UV Laser-Induced Polyimide-to-Graphene Conversion: Modeling, Fabrication, and Application.* Small Methods, 2019. **3**(10): p. 1900208.

143. Kumar, P., K. Subrahmanyam, and C. Rao, *Graphene produced by radiation-induced reduction of graphene oxide.* International Journal of Nanoscience, 2011. **10**(04n05): p. 559-566.

144. Stanford, M.G., et al., *High-Resolution Laser-Induced Graphene. Flexible Electronics beyond the Visible Limit.* ACS Applied Materials & Interfaces, 2020. **12**(9): p. 10902-10907.

145. Wang, Z., et al., *Patterned laser-induced graphene for terahertz wave modulation.* JOSA B, 2020. **37**(2): p. 546-551.

146. Bobinger, M.R., et al., *Flexible and robust laser-induced graphene heaters photothermally scribed on bare polyimide substrates.* Carbon, 2019. **144**: p. 116-126.

147. Nasser, J., et al., *Laser induced graphene printing of spatially controlled super-hydrophobic/hydrophilic surfaces.* Carbon, 2020. **162**: p. 570-578.

148. Dong, J., et al., *Control of superhydrophilic and superhydrophobic graphene interface.* Scientific reports, 2013. **3**(1): p. 1-6.

149. Ferrari, A.C. and J. Robertson, *Interpretation of Raman spectra of disordered and amorphous carbon.* Physical review B, 2000. **61**(20): p. 14095.

150. Eckmann, A., et al., *Probing the nature of defects in graphene by Raman spectroscopy.* Nano letters, 2012. **12**(8): p. 3925-3930.

151. Zhou, H., et al., *Raman scattering of monolayer graphene: the temperature and oxygen doping effects.* Journal of Physics D: Applied Physics, 2011. **44**(18): p. 185404.

152. Kaidarova, A., et al., *Wearable multifunctional printed graphene sensors.* npj Flexible Electronics, 2019. **3**(1): p. 1-10.

153. Lucchese, M.M., et al., *Quantifying ion-induced defects and Raman relaxation length in graphene.* Carbon, 2010. **48**(5): p. 1592-1597.

154. Li, J.-C., et al., *Porous reduced graphene oxide membrane with enhanced gauge factor.* Applied Physics Letters, 2016. **108**(1): p. 013108.

155. Hakamada, M., et al., *Influence of porosity and pore size on electrical resistivity of porous aluminum produced by spacer method.* Materials transactions, 2007. **48**(1): p. 32-36.

156. Lee, S.-H., D. Kang, and I.-K. Oh, *Multilayered graphene-carbon nanotube-iron oxide three-dimensional heterostructure for flexible electromagnetic interference shielding film.* Carbon, 2017. **111**: p. 248-257.

157. Zhang, W., et al., *3D laser scribed graphene derived from carbon nanospheres: an ultrahigh-power electrode for supercapacitors.* Small Methods, 2019. **3**(5): p. 1900005.

158. Poggio, C., et al., *Comparative cytotoxicity evaluation of eight root canal sealers.* Journal of clinical and experimental dentistry, 2017. **9**(4): p. e574.

159. Villa, N., et al., *A New Calcium Silicate-Based Root Canal Dressing: Physical and Chemical Properties, Cytotoxicity and Dentinal Tubule Penetration.* Brazilian Dental Journal, 2020. **31**: p. 598-604.

160. Menczel, J.D. and R.B. Prime, *Thermal analysis of polymers: fundamentals and applications*. 2009: John Wiley & Sons.

161. Chaidez, V., et al., *Decadal trends in Red Sea maximum surface temperature.* Scientific reports, 2017. **7**(1): p. 1-8.

162. Rasul, N.M. and I.C. Stewart, *The Red Sea: the formation, morphology, oceanography and environment of a young ocean basin*. 2015: Springer.

163. Kvítek, O., et al., *Annealing of gold nanolayers sputtered on polyimide and polyetheretherketone.* Thin Solid Films, 2016. **616**: p. 188-196.

164. Buttner, U., K.N. Salama, and C. Sapsanis, *Selective laser etching or ablation for fabrication of devices*. 2018, Google Patents.

165. Wei, Y., et al., *Highly stable and sensitive paper-based bending sensor using silver nanowires/layered double hydroxides hybrids.* ACS applied materials & interfaces, 2015. **7**(26): p. 14182-14191.

166. Saggio, G., et al., *Resistive flex sensors: a survey.* Smart Materials and Structures, 2015. **25**(1): p. 013001.

167. Zhou, H. and H. Hu, *Human motion tracking for rehabilitation—A survey.* Biomedical signal processing and control, 2008. **3**(1): p. 1-18.

168. Kaniusas, E., et al., *Method for continuous nondisturbing monitoring of blood pressure by magnetoelastic skin curvature sensor and ECG.* IEEE Sensors Journal, 2006. **6**(3): p. 819-828.

169. Giouroudi, I., et al., *Magnetostrictive bilayer sensor for micro torque measurements.* Sensor Letters, 2007. **5**(1): p. 304-307.

170. Levangie, P.K. and C.C. Norkin, *Joint structure and function: a comprehensive analysis.* 2011.

171. Jepsen, N., et al., *The use of external electronic tags on fish: an evaluation of tag retention and tagging effects.* Animal Biotelemetry, 2015. **3**(1): p. 1-23.

172. Wang, P.T., et al., *A durable, low-cost electrogoniometer for dynamic measurement of joint trajectories.* Medical engineering & physics, 2011. **33**(5): p. 546-552.

173. Jang, D., et al., *Design of a highly flexible and sensitive multi-functional polymeric sensor incorporating CNTs and carbonyl iron powder.* Composites Science and Technology, 2021. **207**: p. 108725.

174. Akkuş, Ü.Ö., E. Balcı, and S. Berber, *Mo2TiC2O2 MXene-based nanoscale pressure sensor.* Physica E: Low-dimensional Systems and Nanostructures, 2020. **116**: p. 113762.

175. Kumar, R., et al., *Transition metal dichalcogenides-based flexible gas sensors.* Sensors and Actuators A: Physical, 2020. **303**: p. 111875.

176. Frank, O., et al., *Compression behavior of single-layer graphenes.* ACS nano, 2010. **4**(6): p. 3131-3138.

177. Gong, L., et al., *Interfacial stress transfer in a graphene monolayer nanocomposite.* Advanced Materials, 2010. **22**(24): p. 2694-2697.

178. Eswaraiah, V., K. Balasubramaniam, and S. Ramaprabhu, *One-pot synthesis of conducting graphene–polymer composites and their strain sensing application.* Nanoscale, 2012. **4**(4): p. 1258-1262.

179. Wang, Y., et al., *Flexible electrically resistive-type strain sensors based on reduced graphene oxide-decorated electrospun polymer fibrous mats for human motion monitoring.* Carbon, 2018. **126**: p. 360-371.

180. Xu, M., et al., *Highly stretchable strain sensors with reduced graphene oxide sensing liquids for wearable electronics.* Nanoscale, 2018. **10**(11): p. 5264-5271.

181. Hosseinzadeh, A., et al., *Graphene based strain sensors: a comparative study on graphene and its derivatives.* Applied Surface Science, 2018. **448**: p. 71-77.

182. Doll, J.C., S.-J. Park, and B.L. Pruitt, *Design optimization of piezoresistive cantilevers for force sensing in air and water.* Journal of applied physics, 2009. **106**(6): p. 064310.

183. Harkey, J. and T.W. Kenny, *1/f noise considerations for the design and process optimization of piezoresistive cantilevers.* Journal of microelectromechanical systems, 2000. **9**(2): p. 226-235.

184. Doll, J.C., et al., *Piezoresistive cantilever optimization and applications.* MRS Online Proceedings Library (OPL), 2009. **1222**.

185. Park, S., et al. *Optimization of piezoresistive cantilever performance*. in *Hilton Head Sensors, Actuators and Microsystems Workshop*. 2008.

186. Marengo, M., G. Marinaro, and J. Kosel. *Flexible temperature and flow sensor from laser-induced graphene*. in *2017 IEEE SENSORS*. 2017. IEEE.

187. Bograd, S.J., et al., *Biologging technologies: new tools for conservation. Introduction.* Endangered Species Research, 2010. **10**: p. 1-7.

188. Gleiss, A.C., R.P. Wilson, and E.L. Shepard, *Making overall dynamic body acceleration work: on the theory of acceleration as a proxy for energy expenditure.* Methods in Ecology and Evolution, 2011. **2**(1): p. 23-33.

189. Sato, K., et al., *Stroke frequency, but not swimming speed, is related to body size in free-ranging seabirds, pinnipeds and cetaceans.* Proceedings of the Royal Society B: Biological Sciences, 2007. **274**(1609): p. 471-477.

190. Wilson, R.P., et al., *Diel dive depth in penguins in relation to diel vertical migration of prey: whose dinner by candlelight?* Marine Ecology Progress Series, 1993. **94**: p. 101-104.

191. Shepard, E.L., et al., *Flexible paddle sheds new light on speed: a novel method for the remote measurement of swim speed in aquatic animals.* Endangered Species Research, 2008. **4**(1-2): p. 157-164.

192. Mulligan, A.E., et al., *Differential pressure systems and methods for measuring hydraulic parameters across surface water-aquifer interfaces*. 2014, Google Patents.

193. Tardi, G., et al., *Experimental assessment of a variable orifice flowmeter for respiratory monitoring.* Journal of Sensors, 2015. **2015**.

194. Han, Y., et al., *Flow measurement of oil-in-water emulsions using arc-type conductivity probes and electromagnetic flowmeter.* IEEE Transactions on Instrumentation and measurement, 2018. **67**(3): p. 667-677.

195. Zheng, D., T. Zhang, and Y. Hu, *Experimental investigations of the location of a piezoelectric probe in a vortex flow sensor.* Measurement Science and Technology, 2007. **18**(12): p. 3777.

196. Fuchs, S.I., et al., *Multiple breath washout with a sidestream ultrasonic flow sensor and mass spectrometry: a comparative study.* Pediatric pulmonology, 2006. **41**(12): p. 1218-1225.

197. Haneveld, J., et al., *Modeling, design, fabrication and characterization of a micro Coriolis mass flow sensor.* Journal of micromechanics and microengineering, 2010. **20**(12): p. 125001.

198. Lee, E.S., et al. *AquaMote: ultra low power sensor tag for animal localization and fine motion tracking*. in *Proceedings of the 15th ACM Conference on Embedded Network Sensor Systems*. 2017.

199. Wilson, R.P., E. Shepard, and N. Liebsch, *Prying into the intimate details of animal lives: use of a daily diary on animals.* Endangered species research, 2008. **4**(1-2): p. 123-137.

200. Mustafa, M., et al., *Sleep problems and the risk for sleep disorders in an outpatient veteran population.* Sleep and Breathing, 2005. **9**(2): p. 57-63.

201. Zadra, A., et al., *Somnambulism: clinical aspects and pathophysiological hypotheses.* The Lancet Neurology, 2013. **12**(3): p. 285-294.

202. Song, W., et al., *Flexible, stretchable, and transparent planar microsupercapacitors based on 3D porous laser-induced graphene.* Small, 2018. **14**(1): p. 1702249.

203. Dallinger, A., et al., *Stretchable and skin-conformable conductors based on polyurethane/laser-induced graphene.* ACS applied materials & interfaces, 2020. **12**(17): p. 19855-19865.

204. Kaidarova, A., et al., *Enhanced Graphene Sensors via Multi-lasing Fabrication.* IEEE Sensors Journal, 2021.

205. Li, Y., et al., *IMU/magnetometer/barometer/mass-flow sensor integrated indoor quadrotor UAV localization with robust velocity updates.* Remote Sensing, 2019. **11**(7): p. 838.

206. Chow, J.C., J.D. Hol, and H. Luinge, *Tightly-coupled joint user self-calibration of accelerometers, gyroscopes, and magnetometers.* Drones, 2018. **2**(1): p. 6.

207. Wang, S., Z. Deng, and G. Yin, *An accurate GPS-IMU/DR data fusion method for driverless car based on a set of predictive models and grid constraints.* Sensors, 2016. **16**(3): p. 280.

208. Zhao, Y., *Applying time-differenced carrier phase in nondifferential GPS/IMU tightly coupled navigation systems to improve the positioning performance.* IEEE Transactions on Vehicular Technology, 2016. **66**(2): p. 992-1003.

209. El-Mowafy, A. and N. Kubo, *Integrity monitoring for Positioning of intelligent transport systems using integrated RTK-GNSS, IMU and vehicle odometer.* IET Intelligent Transport Systems, 2018. **12**(8): p. 901-908.

210. Wang, L., et al., *Attitude determination method by fusing single antenna GPS and low cost MEMS sensors using intelligent Kalman filter algorithm.* Mathematical Problems in Engineering, 2017. **2017**.

211. Youn, W. and S.A. Gadsden, *Combined quaternion-based error state Kalman filtering and smooth variable structure filtering for robust attitude estimation.* IEEE Access, 2019. **7**: p. 148989-149004.

212. Casey, R.T., *A comparison of attitude propagation and parameterization methods for low-cost UAVs*. 2012: University of California, Santa Cruz.

213. Godha, S., G. Lachapelle, and M.E. Cannon. *Integrated GPS/INS system for pedestrian navigation in a signal degraded environment*. in *Proceedings of the 19th International Technical Meeting of the Satellite Division of The Institute of Navigation (ION GNSS 2006)*. 2006.

214. Szabó, S., et al., *Automated registration of potential locations for solar energy production with Light Detection And Ranging (LiDAR) and small format photogrammetry.* Journal of Cleaner Production, 2016. **112**: p. 3820-3829.

215. Zahran, S., et al., *A new velocity meter based on Hall effect sensors for UAV indoor navigation.* IEEE Sensors Journal, 2018. **19**(8): p. 3067-3076.

216. Pang, C., C. Lee, and K.Y. Suh, *Recent advances in flexible sensors for wearable and implantable devices.* Journal of Applied Polymer Science, 2013. **130**(3): p. 1429-1441.

217. Patel, S., et al., *A review of wearable sensors and systems with application in rehabilitation.* Journal of neuroengineering and rehabilitation, 2012. **9**(1): p. 1-17.

218. Chou, H.-H., et al., *A chameleon-inspired stretchable electronic skin with interactive colour changing controlled by tactile sensing.* Nature communications, 2015. **6**(1): p. 1-10.

219. Yamada, T., et al., *A stretchable carbon nanotube strain sensor for human-motion detection.* Nature nanotechnology, 2011. **6**(5): p. 296-301.

220. Wang, X., Z. Liu, and T. Zhang, *Flexible sensing electronics for wearable/attachable health monitoring.* Small, 2017. **13**(25): p. 1602790.

221. Cao, R., et al., *Screen-printed washable electronic textiles as self-powered touch/gesture tribo-sensors for intelligent human–machine interaction.* ACS nano, 2018. **12**(6): p. 5190-5196.

222. Qian, J., D.-S. Kim, and D.-W. Lee, *On-vehicle triboelectric nanogenerator enabled self-powered sensor for tire pressure monitoring.* Nano Energy, 2018. **49**: p. 126-136.

223. Shaikh, S.F., et al., *Environmental Monitoring: Noninvasive Featherlight Wearable Compliant "Marine Skin": Standalone Multisensory System for Deep-Sea Environmental Monitoring (Small 10/2019).* Small, 2019. **15**(10): p. 1970051.

224. Wang, J., et al., *Silver nanowire electrodes: conductivity improvement without post-treatment and application in capacitive pressure sensors.* Nano-micro letters, 2015. **7**(1): p. 51-58.

225. Nela, L., et al., *Large-area high-performance flexible pressure sensor with carbon nanotube active matrix for electronic skin.* Nano letters, 2018. **18**(3): p. 2054-2059.

226. Peng, Y., et al., *Achieving high-resolution pressure mapping via flexible GaN/ZnO nanowire LEDs array by piezo-phototronic effect.* Nano Energy, 2019. **58**: p. 633-640.

227. Kaidarova, A., et al., *Laser-printed, flexible graphene pressure sensors.* Global Challenges, 2020. **4**(4): p. 2000001.

228. Mahmoud, W., et al., *A novel application of ADC/K-foaming agent-loaded NBR rubber composites as pressure sensor.* Journal of Physics D: Applied Physics, 2006. **39**(3): p. 541.

229. Shcherbina, A., et al., *Accuracy in wrist-worn, sensor-based measurements of heart rate and energy expenditure in a diverse cohort.* Journal of personalized medicine, 2017. **7**(2): p. 3.

230. O'Driscoll, R., et al., *How well do activity monitors estimate energy expenditure? A systematic review and meta-analysis of the validity of current technologies.* British Journal of Sports Medicine, 2020. **54**(6): p. 332-340.

231. Choong, C.L., et al., *Highly stretchable resistive pressure sensors using a conductive elastomeric composite on a micropyramid array.* Advanced materials, 2014. **26**(21): p. 3451-3458.

232. Kappassov, Z., J.-A. Corrales, and V. Perdereau, *Tactile sensing in dexterous robot hands.* Robotics and Autonomous Systems, 2015. **74**: p. 195-220.

233. Fishel, J.A., G.M. Berke, and K.A. Muller, *Tactile Sensing Reflexes for Advanced Prosthetic Hands*. 2017, SynTouch.

234. Gallagher, D., et al., *Application of a novel biomimetic tactile evaluation system to quantify/qualify desired product feel: 7143.* Journal of the American Academy of Dermatology, 2018. **79**(3).

235. Dargahi, J. and S. Najarian, *Human tactile perception as a standard for artificial tactile sensing—a review.* The international journal of medical robotics and computer assisted surgery, 2004. **1**(1): p. 23-35.

236. Nag, A., S.C. Mukhopadhyay, and J. Kosel, *Sensing system for salinity testing using laser-induced graphene sensors.* Sensors and Actuators A: Physical, 2017. **264**: p. 107-116.

237. Hughes, T.P., et al., *Climate change, human impacts, and the resilience of coral reefs.* science, 2003. **301**(5635): p. 929-933.

238. Sabine, C.L., et al., *The oceanic sink for anthropogenic CO2.* science, 2004. **305**(5682): p. 367-371.

239. Broadbent, H.A., S.Z. Ivanov, and D.P. Fries, *A miniature, low cost CTD system for coastal salinity measurements.* Measurement Science and Technology, 2007. **18**(11): p. 3295.

240. Hounslow, A.W., *Water quality data: analysis and interpretation*. 2018: CRC press.

241. Hyldgård, A., et al., *Autonomous multi-sensor micro-system for measurement of ocean water salinity.* Sensors and Actuators A: Physical, 2008. **147**(2): p. 474-484.

242. Delauney, L., C. Compere, and M. Lehaitre, *Biofouling protection for marine environmental sensors.* Ocean Science, 2010. **6**(2): p. 503-511.

243. Nurioglu, A.G. and A.C.C. Esteves, *Non-toxic, non-biocide-release antifouling coatings based on molecular structure design for marine applications.* Journal of Materials Chemistry B, 2015. **3**(32): p. 6547-6570.

244. Kaidaorva, A., et al., *Flexible, four-electrode conductivity cell for biologging applications.* Results in Materials, 2019. **1**: p. 100009.

245. Kaidarova, A., et al., *Flexible and biofouling independent salinity sensor.* Advanced Materials Interfaces, 2018. **5**(23): p. 1801110.

246. Hyldgard, A., et al. *FISH & CHIPS: four electrode conductivity/salinity sensor on a silicon multi-sensor chip for fisheries research*. in *SENSORS, 2005 IEEE*. 2005. IEEE.

247. Ishai, P.B., et al., *Electrode polarization in dielectric measurements: a review.* Measurement science and technology, 2013. **24**(10): p. 102001.

248. Hunt, R.C., *How to increase the accuracy of solution conductivity measurements.* Santa Ana, CA: Sensor Development, 1995.

249. Fofonoff, N.P. and R. Millard Jr, *Algorithms for the computation of fundamental properties of seawater.* 1983.

250. Spieler, R.E., D.S. Gilliam, and R.L. Sherman, *Artificial substrate and coral reef restoration: what do we need to know to know what we need.* Bulletin of Marine Science, 2001. **69**(2): p. 1013-1030.

251. Abràmoff, M.D., P.J. Magalhães, and S.J. Ram, *Image processing with ImageJ.* Biophotonics international, 2004. **11**(7): p. 36-42.

252. Lenz, J. and S. Edelstein, *Magnetic sensors and their applications.* IEEE Sensors journal, 2006. **6**(3): p. 631-649.

253. Ge, J., et al., *A bimodal soft electronic skin for tactile and touchless interaction in real time.* Nature communications, 2019. **10**(1): p. 1-10.

254. Granell, P.N., et al., *Highly compliant planar Hall effect sensor with sub 200 nT sensitivity.* npj Flexible Electronics, 2019. **3**(1): p. 1-6.

255. Alfadhel, A. and J. Kosel, *Magnetic nanocomposite cilia tactile sensor.* Advanced Materials, 2015. **27**(47): p. 7888-7892.

256. Melzer, M., et al., *Wearable magnetic field sensors for flexible electronics.* Advanced Materials, 2015. **27**(7): p. 1274-1280.

257. Schaefer, B.T., et al., *Gate-Tunable Graphene Hall Sensors with High Magnetic Field Sensitivity.* arXiv preprint arXiv:1912.12678, 2019.

258. Collomb, D., P. Li, and S.J. Bending, *Nanoscale graphene Hall sensors for high-resolution ambient magnetic imaging.* Scientific reports, 2019. **9**(1): p. 1-10.

259. Xu, H., et al., *Flicker noise and magnetic resolution of graphene hall sensors at low frequency.* Applied Physics Letters, 2013. **103**(11): p. 112405.

260. Kaidarova, A., et al., *Flexible Hall sensor made of laser-scribed graphene.* npj Flexible Electronics, 2021. **5**(1): p. 1-7.

261. Kushmerick, J.G.e.a., *Hall effect measurements.*

262. Wang, Z., et al., *Encapsulated graphene-based Hall sensors on foil with increased sensitivity.* physica status solidi (b), 2016. **253**(12): p. 2316-2320.

263. Mystkowski, A., et al., *Flux measurement and conditioning system for heteropolar active magnetic bearing using Kapton-foil Hall sensors.* Mechanical Systems and Signal Processing, 2019. **115**: p. 394-404.

264. Min, Y.-J., et al., *A CMOS magnetic Hall sensor using a switched biasing amplifier.* IEEE Sensors Journal, 2011. **12**(5): p. 1195-1196.

265. Heidari, H., et al., *A CMOS current-mode magnetic Hall sensor with integrated front-end.* IEEE Transactions on Circuits and Systems I: Regular Papers, 2015. **62**(5): p. 1270-1278.

266. Lee, J., et al., *Low power CMOS-based Hall sensor with simple structure using double-sampling delta-sigma ADC.* Sensors, 2020. **20**(18): p. 5285.

267. Porciatti, A., et al. *Flicker noise in graphene-based Hall sensors*. in *2017 International Conference on Noise and Fluctuations (ICNF)*. 2017. IEEE.

268. Chen, Z., et al., *Graphene nano-ribbon electronics.* Physica E: Low-dimensional Systems and Nanostructures, 2007. **40**(2): p. 228-232.

269. Shao, Q., et al., *Flicker noise in bilayer graphene transistors.* IEEE Electron Device Letters, 2009. **30**(3): p. 288-290.

270. Kyberd, P.J. and P.H. Chappell, *A force sensor for automatic manipulation based on the Hall effect.* Measurement Science and Technology, 1993. **4**(3): p. 281.

271. Wang, H., et al., *Design methodology for magnetic field-based soft tri-axis tactile sensors.* Sensors, 2016. **16**(9): p. 1356.

272. Jamone, L., et al., *Highly sensitive soft tactile sensors for an anthropomorphic robotic hand.* IEEE sensors Journal, 2015. **15**(8): p. 4226-4233.

273. Mirzanejad, H., et al. *A new soft force sensor using blended silicone-magnetic powder*. in *2017 5th RSI International Conference on Robotics and Mechatronics (ICRoM)*. 2017. IEEE.

274. Almansouri, A.S., et al., *An imperceptible magnetic skin.* Advanced Materials Technologies, 2019. **4**(10): p. 1900493.

275. Kaidarova, A., et al., *Tunable, Flexible composite magnets for marine monitoring applications.* Advanced Engineering Materials, 2018. **20**(9): p. 1800229.

276. Hong, S.Y., et al., *Stretchable active matrix temperature sensor array of polyaniline nanofibers for electronic skin.* Advanced Materials, 2016. **28**(5): p. 930-935.

277. Yoon, J., J. Lee, and J. Hur, *Stretchable supercapacitors based on carbon nanotubes-deposited rubber polymer nanofibers electrodes with high tolerance against strain.* Nanomaterials, 2018. **8**(7): p. 541.

278. Woerle, J. and H. Rost, *Roll-to-roll production of transparent conductive films using metallic grids.* MRS bulletin, 2011. **36**(10): p. 789.

LIST OF PUBLICATIONS

Peer Reviewed Journal Publications

J1. N. R. Geraldi, R.P. Wilson, J.Kosel, M. G. Meekan, V.M. Eguíluz, M.M.Hussain, A. Shamim, M. Srivastava, M. S. Strano, X. Zhang, B.S. Ooi, M. Holton, **A. Kaidarova**, L. W. Hopkins, X. Jin, Xun Gong, F.Quintana and C.M. Duarte. "Wearables for an Internet of Marine Life." ***Nature Biotechnology (2021)*** *[Accepted]*

J2. A. Kaidarova, M. T. Vijjapu, K. Telegenov, A. Przybysz, K. N. Salama, and J. Kosel. "Enhanced Graphene Sensors via Multi-lasing Fabrication." ***IEEE Sensors Journal*** (2021).

J3. A. Kaidarova, W. Liu, L. Swanepoel, A. Almansouri, N.R. Geraldi, C M. Duarte, and J. Kosel. "Flexible Hall sensor made of laser-scribed graphene." ***npj Flexible Electronics*** 5, no. 1 (2021): 1-7.

J4. A. Kaidarova, and J. Kosel. "Physical Sensors Based on Laser-Induced Graphene: A Review." ***IEEE Sensors Journal*** (2020).

J5. S. Rossbach, S. Overmans, **A. Kaidarova,** J. Kosel, S. Agusti, and C.M. Duarte. "Giant clams in shallow reefs: UV-resistance mechanisms of Tridacninae in the Red Sea." ***Coral Reefs,*** 39, no. 5 (2020): 1345-1360.

J6. A. Kaidarova, N. Alsharif, B. Nicoly M. Oliveira, M.Marengo, N.R. Geraldi, C. M. Duarte, and J. Kosel. "Laser-printed, flexible graphene pressure sensors." ***Global Challenges*** 4, no. 4 (2020): 2000001. **On the Cover**

J7. A. Kaidarova, M. Marengo, N.R. Geraldi, C.M. Duarte, and J. Kosel. "Flexible conductivity, temperature, and depth sensor for marine environment monitoring." ***IEEE Sensors*** (2019).

J8. A. S. Almansouri, N. A. Alsharif, M. A. Khan, L. Swanepoel, **A. Kaidarova**, K.N. Salama, and J. Kosel. "An imperceptible magnetic skin." ***Advanced Materials Technologies*** 4, no. 10 (2019): 1900493.

J9. A. Kaidarova, M.A.Khan, M.Marengo, L.Swanepoel, A.Przybysz, C.Muller, A.Fahlman, U. Buttner, N.R. Geraldi, R.P Wilson, C.M Duarte and J.Kosel."Wearable multifunctional printed graphene sensors." ***npj Flexible Electronics,*** 3, no. 1 (2019): 1-10.

J10. M.A. Karimi, Q.Zhang, Y.H.Kuo, S. F.Shaikh, **A. Kaidarova,** N.Geraldi, M.Mustafa Hussain, J. Kosel, C. M. Duarte, and A. Shamim. "Flexible tag design for semi-continuous wireless data acquisition from marine animals." ***Flexible and Printed Electronics,*** 4, no. 3 (2019): 035006.

J11. A. Kaidarova, M. Marengo, G.Marinaro, N. R. Geraldi, R. Wilson, C.M. Duarte, and J. Kosel. "Flexible, four-electrode conductivity cell for biologging applications." ***Results in Materials,*** 1 (2019): 100009.

J12. L.Swanepoel, **A. Kaidarova**, A. Almansouri, M. A. Khan, J. H. Müller, and J. Kosel. "Ultra Low Power Sensor for 3-Phase Water-Cut Applications." ***IEEE Sensors Letters,*** 3, no. 3 (2019): 1-4.

J13 A. Kaidarova, M. Marengo, G. Marinaro, N. Geraldi, C. M. Duarte, and J. Kosel. "Flexible and biofouling independent salinity sensor." ***Advanced Materials Interfaces,*** 5, no. 23 (2018): 1801110.

J14 A. Kaidarova, M.A Karimi, S.Amara, A.Shamim, N. R. Gerali, C.M. Duarte, and J. Kosel. "Sensor for real-time animal condition and movement monitoring." ***IEEE Sensors*** (2018)

J15 A. Kaidarova, M.A Khan, S.Amara, N. R. Geraldi, M.A Karimi, A.Shamim, R. P. Wilson, C. M. Duarte, and Jurgen Kosel. "Tunable, Flexible composite magnets for marine monitoring applications." *Advanced Engineering Materials*20, no. 9 (2018): 1800229.

International Conference Presentations:

C1. **A. Kaidarova**, S.Aldhurais, D.Cachon, and J.Kosel, "Hall Effect Sensors in Laser Scribed Graphene **", IEEE International Conference on Flexible and Printable Sensors and Systems (FLEPS)**, Manchester, 2020

C2. A. Kaidarova, M.Marengo, N.R.Geraldi, C.M. Duarte, J. Kosel "Flexible conductivity, temperature, and depth sensor for marine environment monitoring**", IEEE Sensors,** 2019, Montreal, Canada, 2019

C3. A. Kaidarova, A.Almoudi, R.Allagani, M.Marengo, M.A. Khan, B.Buttner, D.M. Duarte, J. Kosel. " Flexible and Multi-functional Graphene sensor platform" **IEEE International Conference on Flexible and Printable Sensors and Systems (FLEPS),** Glasgow, Scotland, 2019.

C4. A. Kaidarova, S. Aldhurais, D. Cacho A.Almansouri, M.A Khan, U.Buttner, J. Kosel , "Flexible Hall sensors based on laser induced graphene", **MMM/Intermag**, Washington, USA, 2019 .

C5. A. Kaidarova, M. A. Karimi, S.Amara, A. Shamim, N. Geraldi, C. M. Duarte, "A wireless magnetic system for marine animal conservation", **Joint European Magnetic Symposia** , Mainz, Germany, 2018.

C6. A. Kaidaorva, M. Marengo, G. Marinaro, N.R. Geraldi, L. Swaneapoel, R. Wilson, C.M Duarte and J.Kosel, “Laser induced graphene sensors for marine animal speed monitoring.”, **MSSM2018**, Paisley, Scotland, 2018

C7. A. Kaidaorva, M. Marengo, G. Marinaro, L. Swaneapoel, N.R. Geraldi, R. Wilson, C.M Duarte and J.Kosel, “Flexible,four-electrode conductivity cell for biologging applications”, **MSSM2018**, Paisley, Scotland, 2018

C8. A. Kaidarova, M. A. Karimi, S.Amara; A. Shamim, N. Geraldi, C. M. Duarte, J. Kosel, "Magnetic sensor system for real-time marine animals monitoring," **ICM**, San Francisco, ,2018

C9. A. Kaidarova, S.Amara, M. A. Karimi, A. Shamim, N. Geraldi, C. M. Duarte, J. Kosel, "Remote Underwater Animal Monitoring Magnetic Sensor System," **Intermag,** Singapore, 2018

C10. A.Kaidarova, S.Amara, N.Geraldi, C.Duarte, J.Kosel,”Underwater animal monitoring magnetic sensor system”, **MMM 2017**, Pittsburgh, USA, 2017

APPENDICES

Figure 1.1. Copyright © [2021] Wiley-VCH. Reprinted with permission from [6]

Figure 2.3 – Figure 2.9. Copyright © [2021] IEEE. Reprinted with permission from [45].

Figure 3.3. Copyright ©[2021] Nature. Reprinted with permission from [246]
Figure 3.4 – Figure 3.6. Copyright © [2021] IEEE. Reprinted with permission from [190].
Figure 3.7. Copyright © [2020] Wiley-VCH. Reprinted with permission from [213]
Figure 3.8a. Copyright ©[2021] Nature. Reprinted with permission from [246]
Figure 3.8b. Copyright © [2019] IEEE. Reprinted with permission from [230].

Figure 4.1 –Figure 4.13. Copyright ©[2019] Nature. Reprinted with permission from [138]

Figure 5.1- Figure 5.6. Copyright © [2021] IEEE. Reprinted with permission from [190].
Figure 6.1- Figure 6.9. Copyright © [2020] Wiley-VCH. Reprinted with permission [213]

Figure 7.3. Copyright © [2018] Wiley-VCH. Reprinted with permission [231]
Figure 7.2 –Figure 7.7. Copyright © [2019] Elsevier. Reprinted with permission from [230].
Figure 7.8 –Figure 7.13. Copyright © [2018] Wiley-VCH. Reprinted with permission [231]

Figure 8.1- Figure 8.15. Copyright ©[2021] Nature. Reprinted with permission from [246]